國立交通大學

機械工程學系

博 士 論 文

純旋轉自由度之運動模擬系統之

最佳化設計與控制

Optimal Design and Control for Motion Simulator System of

Rotational Degrees of Freedom

研 究 生：張 仰 宏

指導老師：成 維 華 教授

中 華 民 國 九 十 七 年 七 月

純旋轉自由度之運動模擬系統之最佳化設計與控制

Optimal Design and Control for Motion Simulator System of Rotational Degrees of Freedom

研　究　生：張 仰 宏　　Student: Yang-Hung Chang

指 導 教 授：成 維 華　　Advisor: Wei-Hua Chieng

國 立 交 通 大 學

機 械 工 程 學 系

博 士 論 文

A Dissertation

Submitted to Department of Mechanical Engineering

College of Engineering

National Chiao Tung University

In Partial Fulfillment if the Requirements

For the Degree of Doctor of Philosophy

in

Mechanical Engineering

July 2008

Hsinchu, Taiwan

中 華 民 國 九 十 七 年 七 月

純旋轉自由度之運動模擬系統之最佳化設計與控制

學生：張仰宏　指導老師：成維華

國立交通大學機械工程學系

摘要

本論文之研究目的在於運用一個純旋轉自由度之運動平台，對於運動模擬系統提出一個最佳化的設計與控制；對於 X 系列之運動控制平台結合最佳工作空間以及機械效益的設計之可行性，作深入性的探討與分析。此研究對於低成本之運動控制系統有其重要性。而最佳化目標函數之設計方法亦將呈現。本文所提出之方法結合了某些主要的課題如：工作空間的大小、工作空間的對稱性、以及驅動系統的輸出功率要求等。再者藉由採取一全域最佳化之程序-基因演算法，以及運用「逆向/正向」運動學所推導之成效指標所決定的展開角，可改善運動平台之靜態與動態的成效。此外，藉由一以即時最佳化演算法推導之運動線索控制策略，運用在前述之運動模擬系統-純旋轉自由度平台-可呈現翻滾、俯仰、偏轉、正衝以及側衝等五個自由度之動作。而權函數在每一個取樣時間皆可適應性地自我調整以獲得最佳歐拉角之解析解。此運動線索控制策略因其不需要遞迴地搜尋最佳解故能呈現出極佳的效率。實驗結果呈現其對於五自由度之運動模擬之正

確性及有效性。此運動策略配合軟硬體的實現已應用在 X2/X360 之運動模擬系統上。

Optimal Design and Control for Motion Simulator System of Rotational Degrees of Freedom

Student: Yang-Hung Chang Advisor: Wei-Hua Chieng

Institute of Mechanical Engineering National Chiao Tung University

Abstract

This dissertation presents an optimal method for designing and controlling a novel motion simulator system with only rotational degrees of freedom (DOF). The feasibility of adopting the design of X-series motion platforms to combine optimal workspace and mechanical advantage, which is considered important for low-cost simulators, is investigated. A design method to optimize an objective function is also presented. The proposed method consolidates some major issues associated with workspace volume, workspace symmetry, and actuator power requirements. Performance indices obtained from inverse/forward kinematics are adopted within a global optimization procedure, a genetic algorithm (GA), to determine the designed spread-angle that improves static and dynamic performance. Furthermore, an optimal motion-cueing strategy is applied to the designed simulator system with three rotational DOF to perform the roll, pitch, yaw, surge, and sway motions via an online optimization algorithm. Weighting functions are adaptively tuned in each step, and the optimal Euler angles are obtained analytically. This motion-cueing algorithm is efficient as it requires no recursive search on the optimal solution. Experimental results demonstrating the

validity of the five DOF motion simulation are presented. The proposed algorithm is applied to X2/X360 motion simulators with software and hardware realization.

Keywords: genetic algorithm, mechanism design, motion cueing; motion simulator, parallel mechanism, online optimization

誌　　謝

本論文的完成，首先感謝指導老師 成維華 教授。

感謝 廖俊旭 學長。

感謝 翁瑞鴻 學長， 童永成 同學，楊嘉豐 同學，黃旭生 同學，黃柏瑞 同學。

感謝 吳秉霖 學弟。

衷心感謝 偉傑、心豪、維宗。

特別感謝 領航數位國際/動感科技股份有限公司董事長、總經理、暨所有同仁的協助。

最後，感謝父母親與家人的支持與包容。謹以此論文與榮耀，獻給我的父親與母親。

Contents

摘要 i

Abstract iii

誌謝 v

Contents vi

List of Figures viii

List of Tables xi

Nomenclature xii

Chapter 1 Introduction 1

Chapter 2 Optimal Design for X-series Motion Platform Using Genetic Algorithm 8

2.1 Problem Statement 8

2.1.1 Introduction to the 2-DOF Motion Platform, X-2 8

2.1.2 Objective of Optimization on the X-2 Motion Platform 9

2.2 Workspace and Mechanical Advantage Analysis of the X-2 Platform 9

2.2.1 Maximum Pitch/Roll Angle with Different Spread-Angle ϕ 10

2.2.2 Workspace Symmetry 13

2.2.3 Mechanical Advantage Analysis 13

2.3 Optimal Design for the X-2 Motion Platform 15

2.3.1 Objective Matrix, Cost, and Fitness 16

2.3.2 Weights 16

2.3.3 Optimal Analysis Using Genetic Algorithm 18

Chapter 3 Optimal Motion Cueing for Rotational-DOF Motion Simulators 20

3.1 Human Perception and the Performance Index of Motion Cueing 20

3.1.1 The Performance Index of Yaw Motion 22

3.1.2 The Performance Index of a Combination of Pitch and Surge Motions 23

3.1.3 The Performance Index of a Combination of Roll and Sway Motions 26

3.2 Motion Cueing Strategy for the X-2/X360 Motion Simulator 27

3.2.1 Real-Time Motion Simulation Structure 28

3.2.2 Motion Cueing Strategy 28

3.3 Real-time Optimal Motion Cueing Algorithm (ROMA) 29

3.3.1 K-K-T Conditions 29

3.3.2 Optimization on Yaw Motion 30

3.3.3 Optimization on Pitch and Surge Motion 32

3.3.4 Optimization on Roll and Sway Motion 33

3.3.5 Physical Meaning of Each Case of the Optimization 35

3.4 Washout Filtering 36

3.4.1 Yawing Washout Filter 36

3.4.2 Adaptive Washout Filter 37

Chapter 4 Simulation and Experimental Results 39

Chapter 5 Conclusion 44

Appendix 47

A. Inverse Kinematics of the X-2 Motion Platform 47

B. Forward Kinematics of the X-2 Motion Platform 48

C. Jacobian of the X-2 Motion Platform 52

D. Additional Kinematics for X-360 (based on X-2) 54

References 56

本論文作者已發表之著作 103

List of Figures

Fig. 1. 2-DOF motion platform, X-2 62

Fig. 2. Pitch motion of X-2 platforms in the view of (a) 3D view and (b) side view. 63

Fig. 3. Roll motion of X-2 platforms in the view of (a) 3D view and (b) side view. 64

Fig. 4. Flowchart of GA optimization process. 65

Fig. 5. Coordinates on an aircraft 66

Fig. 6. Motion simulator mechanism with 3-DOF in the view of (a) 3-D view (b) front view (c) side view (d) top view 67

Fig. 7. 3-rotational-DOF motion simulation structure 68

Fig. 8. Simplified schematic of the proposed motion cueing strategy 69

Fig. 9. Block diagram of Optimization process of yaw motion 70

Fig. 10. Block diagram of Optimization process of pitch and surge (longitudinal) motion 71

Fig. 11. Block diagram of Optimization process of roll and sway (lateral) motion 72

Fig. 12. Procedure of applying KKT conditions in practice 73

Fig. 13. Experimental X-2 motion platform (Courtesy by IMON Corp.). 74

Fig. 14. Maximum pitch/roll angle along different spread-angle ϕ 75

Fig. 15. Comparison of workspaces with (a) ϕ = 21°, (b) ϕ = 45°, (c) ϕ = 60°, and (d) ϕ = 69° 76

Fig. 16. Workspace symmetry 77

Fig. 17. Comparison of kinetic energy with (a) ϕ = 21°, (b) ϕ = 45°, (c) ϕ = 60°, and (d) ϕ = 69°. 78

Fig. 18. Comparison of potential energy with (a) ϕ = 21°, (b) ϕ = 45°, (c) ϕ = 60°, and (d) ϕ = 69°. 79

Fig. 19. Comparison of gradient of potential energy with (a) ϕ = 21°, (b) ϕ = 45°, (c) ϕ =

60°, and (d) ϕ = 69°. 80

Fig. 20. Comparison of 2-norm of gradient of potential energy with (a) ϕ = 21°, (b) ϕ = 45°, (c) ϕ = 60°, and (d) ϕ = 69°. 81

Fig. 21. Infinity-norm of kinetic energy, $\left\| T|_{\phi} \right\|_{\infty}$ 82

Fig. 22. Infinity-norm of gradient of potential energy, $\left\| \nabla V|_{\phi} \right\|_{\infty}$ 83

Fig. 23. GA optimization, emphasized the workspace symmetry, with weights $w_b = 80$, $w_T = 10$, $w_V = 10$. This figure shows (a) best-so-far solution during GA recursive searching, (b) workspace, (c) potential energy, (d) gradient of potential energy, (e) norm of gradient of potential energy, and (f) kinetic energy as the optimal solution is ϕ = 41.94°. 84

Fig. 24. GA optimization, emphasized the infinity-norm of kinetic energy, with weights $w_b = 10$, $w_T = 80$, $w_V = 10$. This figure shows (a) best-so-far solution during GA recursive searching, (b) workspace, (c) potential energy, (d) gradient of potential energy, (e) norm of gradient of potential energy, and (f) kinetic energy as the optimal solution is ϕ = 21.22°. 85

Fig. 25. GA optimization, emphasized the infinity-norm of kinetic energy, with weights $w_b = 10$, $w_T = 10$, $w_V = 80$. This figure shows (a) best-so-far solution during GA recursive searching, (b) workspace, (c) potential energy, (d) gradient of potential energy, (e) norm of gradient of potential energy, and (f) kinetic energy as the optimal solution is ϕ = 33.49°. 86

Fig. 26. GA optimization, emphasized the infinity-norm of kinetic energy, with weights $w_b = 40$, $w_T = 30$, $w_V = 30$. This figure shows (a) best-so-far solution during GA recursive searching, (b) workspace, (c) potential energy, (d) gradient of potential energy, (e) norm of gradient of potential energy, and (f) kinetic energy as the optimal solution is ϕ = 36.53°. 87

Fig. 27. Implementation of the control and driving system 88
Fig. 28. Trajectory of flight simulation 89
Fig. 29. Comparison of linear high-frequency acceleration along *x*-axis..... 90
Fig. 30. Comparison of linear high-frequency acceleration along *y*-axis..... 91
Fig. 31. Segmental error of linear high-frequency (onset) acceleration along *x*-axis using classical method (CLWF) and the proposed algorithm (ROMA) 92
Fig. 32. Segmental error of linear high-frequency (onset) acceleration along *y*-axis using the classical method (CLWF) and the proposed algorithm (ROMA) 93
Fig. 33. Comparison of simulator output, longitudinal-motion: 94
Fig. 34. Comparison of simulator output, lateral-motion:..... 95
Fig. 35. Comparison of simulator output, yaw-motion: 96
Fig. 36. Yawing-speed and yaw-angle after washout filtering (YWF)..... 97
Fig. 37. Subjective feedback from users with five significant characteristics of flight simulators using proposed algorithm (ROMA)..... 98
Fig. 38. Complete framework of the entire electrical and mechanical system..... 99
Fig. 39. Complete implementation of the system..... 100

List of Tables

Table 1. Experimental Setup of Mechanical System 101

Table 2. Experimental Setup of Servo-Drive System 101

Table 3. Experimental Setup of Software System 102

Nomenclature

Symbol	Physical Meaning
α	Euler angle, yaw
β	Euler angle, pitch
γ	Euler angle, roll
$\mathbf{I}_{main}$	moment of inertia (vector)
p_1	position of slider #1
p_2	position of slider #2
$p_{\max}$	maximum position of sliders
$p_{\min}$	minimum position of sliders
$\mathbf{H}$	vector, from origin to center of mass
$c\bullet$	cos($\bullet$)
$s\bullet$	sin($\bullet$)
$t\bullet$	tan($\bullet$)
T	kinetic energy
V	potential energy
$\|\bullet\|_\infty$	Infinity norm of $\bullet$
$\|\bullet\|_2$	2-norm of $\bullet$
${}^{\Gamma}\vec{\bullet}_i$	vector $\bullet$ at the coordinate Γ with axis i
h_c	height of center of mass
$\nabla\bullet$	gradient of $\bullet$
ϕ	spread-angle
$\mathbf{x}^*$	local minimizer governed by KKT conditions
$\boldsymbol{\mu}^*$	multiplier vector of inequality constraints

$\mathbf{g}$	inequality constraints vector
T	sampling time
g	acceleration due to gravity
$f_{\bullet}$	cost function of $\bullet$
$E_{\bullet}$	error vector of $\bullet$
$Q_{\bullet}$	weighting matrix of $\bullet$
$\omega_{\bullet}$	angular velocity along $\bullet$-axis
$\hat{\omega}_{\bullet}$	reference angular velocity along $\bullet$-axis
$\omega_{\bullet,bound}$	maximum angular velocity along $\bullet$-axis
$\omega_{\bullet,indiff}$	indifference threshold for angular velocity along $\bullet$-axis
$\omega_{\bullet,k+1}$	desired angular velocity along $\bullet$-axis at step $k+1$
$\hat{\omega}_{\bullet,k+1,highpass}$	reference angular velocity along $\bullet$-axis after high-pass filtering at step $k+1$
$a_{\bullet}$	linear acceleration along $\bullet$-axis
$\hat{a}_{\bullet}$	reference linear acceleration along $\bullet$-axis
$a_{\bullet,k+1}$	desired linear acceleration along $\bullet$-axis at step $k+1$
$\hat{a}_{\bullet,k+1}$	reference linear acceleration along $\bullet$-axis at step $k+1$
$\hat{a}_{\bullet,k+1,lowpass}$	reference linear acceleration after low-pass filtering along $\bullet$-axis at step $k+1$
$a_{\bullet,k+1,highpass}$	desired high-frequency linear acceleration along $\bullet$-axis at step $k+1$
$\hat{a}_{\bullet,k+1,highpass}$	reference linear acceleration after high-pass filtering along $\bullet$-axis at step $k+1$
$\hat{\alpha}_{\bullet,k+1,highpass}$	reference angular acceleration along $\bullet$-axis at step $k+1$
$\ell_{\bullet,k}$	equivalent moment arm of $\bullet$

Chapter 1 Introduction

Interactive motion simulators are extensively utilized in not only flight simulation but also the entertainment field. A conventional flight simulator system with six degrees of freedom (DOF) successfully delivers excellent “sustained” and fair “onset” motion cues with long travel distance characteristics. However, the extremely expensive cost and large space requirement have limited their use for entertainment.

Chiang and Chieng (1995) developed a prototype, the SP-120, based on the concept of the Steward platform. The new structure allows the SP-120 to generate improved onset cues and provide sustained motion. Additionally, the space requirement is much less than the conventional one. However, this prototype with six DOF remains too expensive for commercial use. Thus, reducing cost, simplifying the mechanism structure and reducing the order of the actuator system are worthy goals.

This dissertation designs a low-cost motion simulator system. The new motion simulation system has two significant goals: (1) mechanism design for motion platform; and, (2) establish a motion-cueing control strategy. In this work, the optimal design of the new platform, called X-2, is based on a parallel kinematic mechanism structure, which is discussed in Chapter 2. Chapter 3 presents a motion-cueing control strategy for the proposed simulation system.

Parallel manipulators have many benefits over conventional serial manipulators in terms

of accuracy, velocity, stiffness and payload capacity, and are therefore widely adopted in industry. Parallel manipulators [1]–[4] with fewer than six DOF have recently been extensively adopted for various uses as they maintain the advantages inherent in parallel mechanisms, and have several other benefits such as reduced total manufacturing and operation costs.

Performance indices of a parallel kinematic machine (PKM) [5] may include workspace [6], [7], actuator capability, power transmission efficiency, architecture design [8]–[12] and possibly the best accuracy [13].

Various studies of manipulator performance focused on analyzing the manipulator's kinematic properties represented by the Jacobian transformation. These efforts yielded important measures for and characterizations of kinematic properties [14]–[17] and static force capability [18].

Although many parallel mechanisms have been developed] [8], [19], [20], less attention is given to optimal design of a manipulator that has optimal workspace features, or the best mechanical advantages in motion relative to the rotational parallel mechanism. Notably, workspace features and mechanical advantages are significant characteristics in controlling parallel manipulators, particularly for those applied as motion platforms.

Chapter 2 analyzes the global optimization of a two-prismatic-universal-universal (2-PUU) PKM to obtain the best synthetic properties of performance indices, and presents a

novel optimization procedure that, via the use of global optimal searching techniques, addresses some major issues associated with static (workspace) and dynamic (actuator capability) performance. The optimal parallel manipulator design solution is computed using a well-known global optimization algorithm, a genetic algorithm (GA) [21]–[23]. The performance index can be treated as a compromise between the optimal mechanical advantage design and optimal workspace design based on the weight of each term.

After the optimal design for the platform mechanism is obtained, an appropriate motion-cueing control strategy is applied on this platform. To form an optimal motion-cueing strategy for the simulation system, some basic concepts of motion-cueing theory should first be addressed.

A motion simulator attempts a realistic impression of vehicle motion, such as that of an aircraft or racing car. Unfortunately, this goal is not easily achieved because simulators are limited by workspace features and actuator capabilities such as maximum torque and velocity. Engineers have improved simulator motion by developing motion-cueing strategies, known as "washout filtering." Washout filtering is intended to transform trajectories generated by a dynamic virtual reality (VR) model incorporating very large displacements into driving system commands that generate realistic motion cues for a pilot within the simulator's limited workspace.

Washout separates motion cues into high- (onset) and low- (sustained) frequency

components, such that cues to be managed and displayed within the physical confines of a given platform system. Washout must provide a high-pass filtering system, which may be linear or nonlinear, to limit simulator cab excursions. Nonlinear designs include adaptive filters and other optimal control techniques that are applied based on various criteria.

Many schemes for motion-cueing control have been presented. Schmidt and Bjorn [24] analyzed motion drive signals for piloted flight simulators. Conrad and Schmidt [25] proposed techniques for calculating motion drive signals. Sinacori [26] proposed a practical approach for motion simulation. Bowles, Parrish and Dieudonne [27] applied coordinated adaptive washout to motion simulators. Sivan, Ish-shalom and Huang [28] applied an optimal control approach for the design of moving flight simulators. Ariel and Sivan [29] addressed false cue reduction in moving flight simulators. Reid and Nahon [30] developed an algorithm that drives a flight simulator. Nahon and Reid [31] developed simulator motion-drive algorithms. Reid, Nahon and Kirdeikis [32] developed adaptive simulator motion software that has supervisory control. Idan and Sahar [33] presented a robust controller for a simulator with six DOF. Pouliot, Gosselin and Nahon [34] analyzed motion simulation capabilities of flight simulators with three DOF. Moshe and Nahon [35] analyzed an offline comparison of classical and robust flight-simulator motion controls. Martin [36] considered the whole body motion of motion cueing. Liao and Chieng [37] proposed another novel washout filter algorithm for a motion simulator with six DOF. Chang, Liao and Chieng [38] developed a

master switching technique for electronic cam control with special reference to multi-axis coordinated trajectory following.

The theory and development of an optimal algorithm for a flight simulator with six DOF have recently been discussed by Wu and Cardullo [39] and Telban and Cardullo [40]. Their approach incorporates a mathematical model of the human vestibular system that constrains pilot sensation of error between the simulated aircraft and platform motion dynamics. The problem is to determine a transfer function matrix that relates the desired simulator motion input to aircraft input, such that a cost function constraining pilot sensation error (between a simulator and plane) is minimized.

However, the aforementioned studies focused on motion simulators with full spatial DOF, *i.e.*, six DOF; the problem of real-time optimal motion-cueing techniques for simulating specific virtual reality (VR) motion in a motion simulator with limited DOF has rarely been addressed.

To develop a motion-cueing control strategy for motion simulators with rotational DOF without loss of generality, a full rotational DOF platform, the X-360, which is a modified version of the X-2 platform, is adopted for experimental testing.

Chapter 3 presents a novel algorithm for evaluating a real-time optimal motion-cueing strategy for a motion simulator solely with three rotational DOF (yaw, pitch and roll). This algorithm optimizes the additional linear onset cues, providing the attitude and sustained cues

are remained. The proposed algorithm comprises a classical linear washout filter (CLWF), a yawing washout filter (YWF), an adaptive washout filter (AWF) and a real-time optimal motion-cueing algorithm (ROMA). The proposed algorithm individually transforms high- and low-frequency linear motions into output angles of a motion simulator with rotational DOF (3-DOF). These output angles are incorporated into the cockpit attitude control to achieve five DOF motion. The ROMA first defines a quadratic cost function to be minimized. This cost function, which corresponds to the performance index of five DOF motion, is then decoupled into three Euler angles associated with the three DOF simulator. The restrictions of workspace and actuator capabilities are represented as inequality constraints of the motion performance optimization problem. Since the cost function has a quadratic (convex) form, Karush-Kuhn-Tucker (KKT) conditions can be introduced to locate the global optimum. Prior to motion optimization via the ROMA, the YWF is applied to prevent simulator cab excursion from exceeding the workspace. After motion optimization via the ROMA, the AWFs are applied when necessary to reset simulator position gradually. All washout motions are performed in insensible acceleration or rate to the pilot. The remaining Euler angles of the three DOF simulator, *i.e.*, pitch and roll, should simultaneously account for cockpit angular motion and residual tilt during linear motion. The bounds of pitch and roll angles are formulated implicitly, and are calculated during each sample time. Motor commands are obtained by substituting the desired Euler angles into an inverse kinematics model of the three

DOF simulator.

The remainder of this dissertation is organized as follows. Chapter 2 describes the optimal design for the X-2 platform using a GA. Chapter 3 establishes the ROMA for the simulation system. Chapter 4 presents experimental setups and detailed results. Appendices A, B, C and D present the kinematics and Jacobian relations. Tables 1, 2 and 3 show all the electrical, mechanical and software parameters and setup. Synthesis of the characterization and measures into an optimization procedure is then discussed. Finally, the optimization procedure is applied to the design and control for a novel motion simulator system with rotational DOF.

Chapter 2 Optimal Design for X-series Motion Platform Using Genetic Algorithm

Chapter 2 is organized as follows. Section 2.1 briefly describes the architecture of the X-2 motion platform. Section 2.2 then illustrates the performance indices built for the optimization. Section 2.3 introduces the global optimization technique and the practical procedure for the optimal design.

2.1 Problem Statement

The problem statement comprises the following parts: (1) the introduction to the presented motion platform, called the X-2 motion platform, and (2) the performance indices, which are used to determine the cost of optimization.

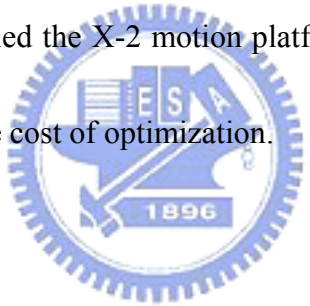

2.1.1 Introduction to the 2-DOF Motion Platform, X-2

The X-2 motion platform is designed for motion simulation with two rotational DOF (pitch and roll). The platform comprises two pairs of screws and sliders, which are actuated directly by servomotors, as shown in Fig. 1. Two linkages are connected between the upper plate and sliders with universal joints on both sides. The upper plate is supported by a universal joint, which constrains the yawing DOF. The spread-angle of the X-2 motion platform is defined as the intersection angle between the two sliders. The spread-angle determines most of the kinematic properties of the X-2 motion platform, which are described

in Section 2.2. Fig. 2 and Fig. 3 respectively depict the pitch and roll motion of the X-2 motion platform. The platform pitches up and down when the sliders both go backwards and forwards. The platform exhibits a roll motion when one slider goes forward and the other one goes backward.

2.1.2 Objective of Optimization on the X-2 Motion Platform

The X-2 motion platform designed to perform the motion cue of reality is limited to the workspace boundary, capability of actuator, power efficiency, and dexterity of motion simulator. A tradeoff among these limitations is necessary to ensure an optimal design of the motion platform. This study defines several performance indices for the X-2 motion platform in terms of the spread-angle. The global search algorithm, GA, is then applied to find the optimal solution of the mechanical design numerically.

2.2 Workspace and Mechanical Advantage Analysis of the X-2 Platform

The performance indices of workspace and mechanical advantage are crucial to the mechanical design of the motion platform. The optimal workspace analysis concerns both the size of the workspace and the workspace symmetry. The mechanical advantage analysis is derived from the infinity norm of the kinetic energy, and the gradient of potential energy within the workspace.

2.2.1 Maximum Pitch/Roll Angle with Different Spread-Angle ϕ

This study defines the maximum pitch or roll angle independently from the neutral (home) position. More specifically, one maximum angle is obtained within the workspace when the other angle is set to zero. According to the above definition, the maximum pitch angle is defined as

$$\beta_{\max} \equiv \arg\max_{p_1, p_2} \beta\big|_{\substack{\gamma=0 \\ \phi=\Phi}} = \left\| \beta\big|_{\substack{\gamma=0 \\ \phi=\Phi}} \right\|_{\infty} \tag{2.1}$$

Since the X-2 mechanism is symmetric about the X-Z plane in the fixed coordinate, the optimization can be reduced to a half-model, as derived in the following equations. According to the kinematics (Appendix A and B), $\beta\big|_{\substack{\gamma=0 \\ \phi=\Phi}}$ is formulated as

$$\beta\big|_{\substack{\gamma=0 \\ \phi=\Phi}} = \beta(p_1, p_1, \phi) = -p_1 \cdot c\beta c\phi^2 - p_1 \cdot s\phi^2 - h \cdot s\beta c\phi = \frac{c_1}{u} \tag{2.2}$$

Equation (2.2) is rearranged as

$$-p_1 \sqrt{1 - s\beta\big|_{\gamma=0}{}^2}\, c\phi^2 = \frac{c_1}{u} + p_1 \cdot s\phi^2 + h \cdot s\beta\big|_{\substack{\gamma=0 \\ \phi=\Phi}} c\phi \tag{2.3}$$

Squaring both sides yields

$$A_\beta \cdot s\beta\big|_{\substack{\gamma=0 \\ \phi=\Phi}}{}^2 + B_\beta \cdot s\beta\big|_{\substack{\gamma=0 \\ \phi=\Phi}} + C_\beta = 0 \tag{2.4}$$

or

$$s\beta\big|_{\substack{\gamma=0 \\ \phi=\Phi}} = \frac{-B_\beta \pm \sqrt{B_\beta{}^2 - 4A_\beta C_\beta}}{2A_\beta} \tag{2.5}$$

where

$$A_\beta = {p_1}^2 \cdot c\phi^4 + h^2 \cdot c\phi^2$$

$$B_\beta = h \cdot p_1 \cdot s\phi^2 c\phi + \frac{h \cdot c_1}{u} c\phi$$

$$C_\beta = \left(\frac{c_1}{u}\right)^2 + \left(p_1 \cdot s\phi^2\right)^2 - \left(p_1 \cdot c\phi^2\right)^2 + 2\frac{c_1}{u} p_1 \cdot s\phi^2$$

Since $\frac{-B_\beta - \sqrt{{B_\beta}^2 - 4A_\beta C_\beta}}{2A_\beta}$ and $\frac{-B_\beta + \sqrt{{B_\beta}^2 - 4A_\beta C_\beta}}{2A_\beta}$ are skew solutions about the kinematic singularity, only the feasible solution is chosen, namely

$$\beta\big|_{\substack{\gamma=0 \\ \phi=\Phi}} = \sin^{-1}\left(\frac{-B_\beta - \sqrt{{B_\beta}^2 - 4A_\beta C_\beta}}{2A_\beta}\right) \tag{2.6}$$

The maximum pitch angle has two possibilities:

$$\left\| \beta\big|_{\substack{\gamma=0 \\ \phi=\Phi}} \right\|_\infty = \begin{cases} \beta(p_{\max}, p_{\max}, \Phi) \\ \beta(p_{\min}, p_{\min}, \Phi) \end{cases} \tag{2.7}$$

Substituting the physical parameters in Nomenclature into the kinematic model in Appendices A and B verifies that

$$\left\| \beta\big|_{\substack{\gamma=0 \\ \phi=\Phi}} \right\|_\infty = \beta(p_{\min}, p_{\min}, \Phi) \tag{2.8}$$

Therefore, the first index is given by

$$\beta_{\max}\big|_{\phi=\Phi} = \left\| \beta\big|_{\substack{\gamma=0 \\ \phi=\Phi}} \right\|_\infty = \beta(p_{\min}, p_{\min}, \Phi) \tag{2.9}$$

Following the similar line of reasoning, the maximum roll angle is derived as

$$\gamma_{\max} \equiv \arg\max_{p_1, p_2} \gamma\big|_{\substack{\beta=0 \\ \phi=\Phi}} = \left\| \gamma\big|_{\substack{\beta=0 \\ \phi=\Phi}} \right\|_\infty \tag{2.10}$$

Then $\gamma\big|_{\beta=0}$ is formulated as a set of simultaneous equations:

$$\begin{cases} -p_1 \cdot c\phi^2 - p_1 \cdot c\gamma s\phi^2 + h \cdot s\gamma s\phi = \frac{c_1}{u} \\ -p_2 \cdot c\phi^2 - p_2 \cdot c\gamma s\phi^2 - h \cdot s\gamma s\phi = \frac{c_2}{u} \end{cases} \tag{2.11}$$

The maximum roll angle occurs when one slider reaches its limit, and the other slider is on the opposite side. The parameters of physical setting determine which slider reaches the maximum or minimum limitation. In this case, the maximum roll angle occurs only if one of the sliders reaches the "maximum" limitation, and the other slider position can be derived from (2.11). Since $\gamma_{\max}\big|_{\phi=\Phi} = \left|\gamma_{\min}\big|_{\phi=\Phi}\right|$ can be derived from the symmetry property, either one of the equations in (2.11) can be adopted to solve the roll angle. For instance, the first equation of (2.11) is applied to yield

$$-p_{\max}\cdot c\phi^2 - p_{\max}\cdot c\gamma\big|_{\substack{\beta=0\\ \phi=\Phi}} s\phi^2 + h\cdot s\gamma\big|_{\substack{\beta=0\\ \phi=\Phi}} s\phi = \frac{c_1}{u} \tag{2.12}$$

Equation (2.12) is rearranged as

$$-p_{\max}\cdot s\phi^2\sqrt{1-s\gamma\big|_{\substack{\beta=0\\ \phi=\Phi}}^{\ 2}} = \frac{c_1}{u} + p_{\max}\cdot c\phi^2 - h\cdot s\gamma\big|_{\substack{\beta=0\\ \phi=\Phi}} s\phi \tag{2.13}$$

Squaring both sides yields

$$A_\gamma\, s\gamma\big|_{\substack{\beta=0\\ \phi=\Phi}}^{\ 2} + B_\gamma\, s\gamma\big|_{\substack{\beta=0\\ \phi=\Phi}} + C_\gamma = 0 \tag{2.14}$$

or

$$s\gamma\big|_{\substack{\beta=0\\ \phi=\Phi}} = \frac{-B_\gamma \pm \sqrt{B_\gamma^{\ 2} - 4A_\gamma C_\gamma}}{2A_\gamma} \tag{2.15}$$

where

$$A_\gamma = h^2\cdot s\phi^2 + p_{\max}^{\ 2}\cdot s\phi^4$$

$$B_\gamma = -2\cdot h\cdot p_1\cdot s\phi c\phi^2 - 2\cdot\frac{c_1}{u}\cdot h\cdot s\phi$$

$$C_\gamma = 2\cdot\frac{c_1}{u}\cdot p_{\max}\cdot c\phi^2 - p_{\max}^{\ 2}\cdot s\phi^4 + \left(\frac{c_1}{u}\right)^2 + p_{\max}^{\ 2}\cdot c\phi^4$$

Since $\dfrac{-B_\gamma - \sqrt{B_\gamma^{\ 2} - 4A_\gamma C_\gamma}}{2A_\gamma}$ and $\dfrac{-B_\gamma + \sqrt{B_\gamma^{\ 2} - 4A_\gamma C_\gamma}}{2A_\gamma}$ are skew solutions about the kinematic

singularity, only the feasible solution is chosen, namely

$$\gamma\Big|_{\substack{\beta=0\\ \phi=\Phi}} = \sin^{-1}\left(\frac{-B_\gamma + \sqrt{B_\gamma{}^2 - 4A_\gamma C_\gamma}}{2A_\gamma}\right) \tag{2.16}$$

According to (2.16), the second index is derived as

$$\gamma_{\max}\Big|_{\phi=\Phi} = \left\|\gamma\Big|_{\substack{\beta=0\\ \phi=\Phi}}\right\|_\infty \tag{2.17}$$

2.2.2 Workspace Symmetry

Workspace symmetry occurs when $\left\|\beta\Big|_{\substack{\gamma=0\\ \phi=\Phi}}\right\|_\infty = \left\|\gamma\Big|_{\substack{\beta=0\\ \phi=\Phi}}\right\|_\infty$ (or simply, $\beta_{\max}\Big|_{\phi=\Phi} = \gamma_{\max}\Big|_{\phi=\Phi}$) at a given angle ϕ. A tradeoff exists between the workspace symmetry and the maximum roll/pitch angle. Thus, the third index for the workspace symmetry is determined by minimizing the following cost function as follows:

$$\Delta\Big|_{\phi=\Phi} \equiv \left\|\beta_{\max}\Big|_{\phi=\Phi} - \gamma_{\max}\Big|_{\phi=\Phi}\right\|_2 \tag{2.18}$$

Individual indices in (2.9), (2.17), and (2.18) can be incorporated to yield a new multi-objective cost function. This multi-objective cost function associated $\beta_{\max}\Big|_{\phi=\Phi}$ and $\gamma_{\max}\Big|_{\phi=\Phi}$ via weights w_p and w_r. Thus, the third index is revised as

$$\Delta\Big|_{\phi=\Phi} \equiv \left\|w_r \cdot \beta_{\max}\Big|_{\phi=\Phi} - w_p \cdot \gamma_{\max}\Big|_{\phi=\Phi}\right\|_2 \tag{2.19}$$

By adjusting w_p and w_r, (2.19) can produce different workspace shapes for a variety of motion applications.

2.2.3 Mechanical Advantage Analysis

The velocity-dependent kinetic energy function of a rotational DOF motion platform is expressed as

$$T = \frac{1}{2}\boldsymbol{\omega}^{\mathrm{T}}\mathbf{I}\boldsymbol{\omega} \tag{2.20}$$

where

$$\boldsymbol{\omega} = \begin{bmatrix} \dfrac{d\gamma}{dt} \\ \dfrac{d\beta}{dt} \\ \dfrac{d\alpha}{dt} \end{bmatrix}$$

and

$$\mathbf{I}_{main} = \begin{bmatrix} I_x & 0 & 0 \\ 0 & I_y & 0 \\ 0 & 0 & I_z \end{bmatrix}$$

The yawing velocity equals zero in the case of the 2- rotational-DOF platform, (2.20) gives

$$T = \frac{1}{2}\left[I_x \left(\frac{d\gamma}{dt} \right)^2 + I_y \left(\frac{d\beta}{dt} \right)^2 \right] \tag{2.21}$$

The derivative chain-rule produces

$$T = \frac{1}{2}\left[I_x \left(\frac{\partial\gamma}{\partial p_1}\frac{dp_1}{dt} + \frac{\partial\gamma}{\partial p_2}\frac{dp_2}{dt} \right)^2 + I_y \left(\frac{\partial\beta}{\partial p_1}\frac{dp_1}{dt} + \frac{\partial\beta}{\partial p_2}\frac{dp_2}{dt} \right)^2 \right] \tag{2.22}$$

$$= \frac{1}{2}\left[I_x \left(\frac{\partial\gamma}{\partial p_1}\dot{p}_1 + \frac{\partial\gamma}{\partial p_2}\dot{p}_2 \right)^2 + I_y \left(\frac{\partial\beta}{\partial p_1}\dot{p}_1 + \frac{\partial\beta}{\partial p_2}\dot{p}_2 \right)^2 \right]$$

The kinetic energy can be considered as an index of power requirement, meaning that the maximum kinetic energy should be minimized. The fourth index corresponding to the input velocity is then formulated as

$$T_{\max}\Big|_{\phi=\Phi} \equiv \arg\max_{p_1,p_2}\{T\} \tag{2.23}$$

The position-dependent potential energy function is expressed as

$$V\Big|_{\phi=\Phi} = mgh_c \tag{2.24}$$

where

$$h_c\Big|_{\phi=\Phi} = \begin{bmatrix}0 & 0 & 1\end{bmatrix}\mathbf{RH} = \begin{bmatrix}0 & 0 & 1\end{bmatrix}\mathbf{R}\begin{bmatrix}H_x\\0\\H_z\end{bmatrix} = -s\beta H_x + c\beta c\gamma H_z \tag{2.25}$$

The gradient of potential energy associated with the input torque is undesirable and needs to be minimized. Therefore, a performance index associated with gravity is defined as the norm of the potential energy gradient. The fifth performance index corresponding to structural dimensions is given by

$$\nabla V_{\max}\Big|_{\phi=\Phi} = \arg\max_{p_1,p_2}\left\{\nabla V\Big|_{\phi=\Phi}\right\} = \left\|\nabla V\Big|_{\phi=\Phi}\right\|_\infty = m\cdot g\cdot\left\|\nabla h_c\Big|_{\phi=\Phi}\right\|_\infty \tag{2.26}$$

where

$$\begin{aligned}\nabla h_c &= \begin{bmatrix}\dfrac{\partial}{\partial p_1}\left(-s\beta H_x + c\beta c\gamma H_z\right)\\[2ex]\dfrac{\partial}{\partial p_2}\left(-s\beta H_x + c\beta c\gamma H_z\right)\end{bmatrix}\\ &= \begin{bmatrix}\left(-H_x c\beta - H_z s\beta c\gamma\right)\dfrac{\partial\beta}{\partial p_1} + \left(-H_z c\beta s\gamma\right)\dfrac{\partial\gamma}{\partial p_1}\\[2ex]\left(-H_x c\beta - H_z s\beta c\gamma\right)\dfrac{\partial\beta}{\partial p_2} + \left(-H_z c\beta s\gamma\right)\dfrac{\partial\gamma}{\partial p_2}\end{bmatrix}\end{aligned} \tag{2.27}$$

2.3 Optimal Design for the X-2 Motion Platform

The objective matrix is defined as a collection of three performance indices presented in

Section 2.2:

$$\begin{bmatrix} \Delta_{\min} \\ T_{\min} \\ \nabla V_{\min} \end{bmatrix} = \begin{bmatrix} \arg\min_{\Phi} \{\Delta\} \\ \arg\min_{\Phi} \{T_{\max}\} \\ \arg\min_{\Phi} \{\nabla V_{\max}\} \end{bmatrix} = \begin{bmatrix} \arg\min_{\Phi} \left\{ \left\| w_r \cdot \beta_{\max}\big|_{\phi=\Phi} - w_p \cdot \gamma_{\max}\big|_{\phi=\Phi} \right\|_2 \right\} \\ \arg\min_{\Phi} \left\{ \arg\max_{p_1, p_2} T\big|_{\phi=\Phi} \right\} \\ \arg\min_{\Phi} \left\{ \arg\max_{p_1, p_2} \nabla V\big|_{\phi=\Phi} \right\} \end{bmatrix} \tag{2.28}$$

Equation (2.28) is not a practical form of optimization, but has to be reformed in the aspect of "cost" or "fitness" for either minimization or maximization.

2.3.1 Objective Matrix, Cost, and Fitness

To "reduce cost", a proper spread-angle of the X-2 mechanism must be found to minimize the cost. The objective function is formulated as a cost function, as follows:

$$f_{cost} = \begin{bmatrix} w_b & w_T & w_V \end{bmatrix} \begin{bmatrix} \Delta_{\min} \\ T_{\min} \\ \nabla V_{\min} \end{bmatrix} \tag{2.29}$$

Conversely, when considering "fitness", the objective function is written as follows:

$$f_{fitness} = \exp\left(\begin{bmatrix} w_b & w_T & w_V \end{bmatrix} \begin{bmatrix} -\Delta_{\min} \\ -T_{\min} \\ -\nabla V_{\min} \end{bmatrix} \right) \tag{2.30}$$

The exponential function ensures that (2.30) is positive definite for the need in the following optimization procedure based on the genetic algorithm.

2.3.2 Weights

The weights associated with different performance indices are assigned before the optimization process is performed. Individual terms of the cost function or fitness function should be non-dimensionalized before the weights are assigned. The first two indices in (2.29) denote "generating the maximum workspace" in the DOF of pitch and roll. Taking pitch as an example, one particular weight can be chosen as a ratio between the desired percentage of importance k_p and the infinity norm of the referenced pitch-angle (the infinity norm of pitch at the referenced spread-angle, ϕ = 45°, which is the middle value of the spread-angle ϕ), that is

$$w_p = \frac{k_p\%}{\left\| \beta \big|_{\gamma=0,\phi=45^\circ} \right\|_\infty} \tag{2.31}$$

Similarly, the weight of the DOF of roll is given by

$$w_r = \frac{k_r\%}{\left\| \gamma \big|_{\beta=0,\phi=45^\circ} \right\|_\infty} \tag{2.32}$$

where k_r denotes the desired percentage of importance of roll-angle.

In the same idea, the weight of workspace symmetry is formulated as

$$w_b = \frac{k_b\%}{\left\| \left\| \beta \big|_{\gamma=0,\phi=45^\circ} \right\|_\infty - \left\| \gamma \big|_{\beta=0,\phi=45^\circ} \right\|_\infty \right\|_2} \tag{2.33}$$

where k_b denotes the desired percentage of importance of workspace symmetry.

The indices associated with mechanical advantage employ the following terms of kinetic energy function and the norm of gradient of potential energy function. The weight of kinetic energy is given by

$$w_T = \frac{k_T\%}{\left\| T|_{\phi=45^\circ} \right\|_\infty} \tag{2.34}$$

where k_T denotes the desired percentage of importance of kinetic energy. The weight of the norm of potential energy gradient is given by

$$w_V = \frac{k_V\%}{\left\| \nabla V|_{\phi=45^\circ} \right\|_\infty} \tag{2.35}$$

where k_V denotes the desired percentage of importance of norm of potential energy gradient.

2.3.3 Optimal Analysis Using Genetic Algorithm

A genetic algorithm (GA) is a probabilistic search technique based on the principles of genetics. Genetic algorithms are applied to the problem of this study as follows. Starting with an initial set of points in Ω, denoted as $P(0)$, the *initial population*. The objective function is then evaluated at points in $P(0)$. A new set of points $P(0)$ may be obtained based on this evaluation. The creation of $P(1)$ involves certain operations on points in $P(0)$, called *crossover* and *mutation*. This procedure is repeated iteratively until a suitable stopping criterion is reached. In summary, the genetic algorithm iteratively performs the operations of crossover and mutation on each population to generate a new population, until a chosen termination criterion is satisfied.

Genetic algorithms are described using terminology adopted from genetics. The algorithm has the following steps:

1. Chromosomes and Representation Schemes

2. Selection and Evolution

Step 0: Find $P(0)$ and set $k = 0$.

Step 1: Evaluate $P(k)$, and update the best-so-far chromosome.

Step 2: If stopping criterion is satisfied, then stop and output the solution.

Step 3: Select $M(k)$ from $P(k)$.

Step 4: Evaluate $M(k)$ to $P(k + 1)$.

Step 5: Set $k = k + 1$, and return to Step 1.

Fig. 4 shows the schematic procedure.

Chapter 3 Optimal Motion Cueing for Rotational-DOF Motion Simulators

Chapter 3 is organized as follows. Section 3.1 describes the human perception and the performance index of motion cueing. Section 3.2 then briefly illustrates the motion cueing strategy for the X-2/X-360 motion simulator. Section 3.3 introduces the real-time optimal motion cueing algorithm (ROMA). Section 3.4 then finally presents the yawing and adaptive washout filtering.

3.1 Human Perception and the Performance Index of Motion Cueing

The motion cues within the motion simulation can be categorized into six components, namely the translations and rotations along *x*, *y*, and *z* axes, respectively. These rotation angles are known as the Euler angles (yaw, pitch, and roll). In flight, any aircraft rotates about its center of gravity, a point that is the average location of the mass of the aircraft. It can be defined as a three dimensional coordinate system through the center of gravity, with each axis perpendicular to the other two axes. The orientation of the aircraft can then be defined as the degree of rotation of the parts of the aircraft along these principal axes (*x*, *y*, and *z* axes), as shown in Fig. 5.

Motion simulation attempts to provide task-critical motion and force information (i.e., "cues") and any required components of the stressor-induced workload increment that would be present in flight or other vehicles [36]. In practice, a motion simulator focuses most strongly on "linear acceleration" and "angular velocity" [30]. Defining an error of motion can

help to construct a particular performance index for real-time processing of motion control. The error of a six DOF motion is defined as a vector of two norms of differences between the actual and required angular velocity/linear acceleration, as follows.

$$E_{overall} = \begin{bmatrix} \left\| \omega_x - \hat{\omega}_x \right\|_2 \\ \left\| \omega_y - \hat{\omega}_y \right\|_2 \\ \left\| \omega_z - \hat{\omega}_z \right\|_2 \\ \left\| a_x - \hat{a}_x \right\|_2 \\ \left\| a_y - \hat{a}_y \right\|_2 \\ \left\| a_z - \hat{a}_z \right\|_2 \end{bmatrix} \tag{3.1}$$

Motion cueing attempts to minimize the above error vector. In this study, a motion simulator with three rotational DOF is concerned. This motion simulator is not naturally capable of performing any linear motion. To present the cues of linear acceleration to a pilot, the cockpit needs to be offset from the pivot of the simulator mechanism, and the rotational motion cue must be sacrificed. Moreover, only the linear accelerations greater than the indifference threshold [30] have to be transformed into angles.

Figure 6 shows a 3-rotational-DOF motion simulator, X-360. The X-360 platform inherits most of the significant characteristics from the X-2 platform. The X-360 employs three rotational DOF. Since this motion simulator is pivoted by a ball joint, and the cockpit is supported on top of the pivot, the heave motion, i.e. linear motion along the *z*-axis, must be left behind during the error minimization. This study is concerned with the following five motion cues

$$E_{total} = \begin{bmatrix} \left\| \omega_x - \hat{\omega}_x \right\|_2 \\ \left\| \omega_y - \hat{\omega}_y \right\|_2 \\ \left\| \omega_z - \hat{\omega}_z \right\|_2 \\ \left\| a_x - \hat{a}_x \right\|_2 \\ \left\| a_y - \hat{a}_y \right\|_2 \end{bmatrix} \tag{3.2}$$

Since the surge and sway motion can only be induced by the pitch and roll motion of the motion simulator, the overall minimization problems can be divided into the following three sub-problems: yaw, longitudinal, and lateral as follows

$$E_{yaw} == \left[\left\| \omega_z - \hat{\omega}_z \right\|_2 \right] \Rightarrow f_{yaw} = E_{yaw}{}^T Q_{yaw} E_{yaw} \tag{3.3}$$

$$E_{longitudinal} = \begin{bmatrix} \left\| \omega_y - \hat{\omega}_y \right\|_2 \\ \left\| a_x - \hat{a}_x \right\|_2 \end{bmatrix} \Rightarrow f_{longitudinal} = E_{longitudinal}{}^T Q_{longitudinal} E_{longitudinal} \tag{3.4}$$

$$E_{lateral} = \begin{bmatrix} \left\| \omega_x - \hat{\omega}_x \right\|_2 \\ \left\| a_y - \hat{a}_y \right\|_2 \end{bmatrix} \Rightarrow f_{lateral} = E_{lateral}{}^T Q_{lateral} E_{lateral} \tag{3.5}$$

The reference point is determined by offset from the pivot to the pilot's head since the proposed algorithm is based on human's Vestibular System. The Vestibular System comprises semicircular canals, which that respond to angular acceleration and velocity, and Otoliths, which are associated with gravity.

3.1.1 The Performance Index of Yaw Motion

The yaw axis (z-axis) is perpendicular to the wings, and lies in the plane of the aircraft centerline. A yaw motion is a side-to-side movement of the nose of the aircraft. The error of yaw motion is defined as

$$E_{yaw} = \left\| \omega_{z,k+1} - \hat{\omega}_{z,k+1,highpass} \right\|_2 \tag{3.6}$$

In the discrete control domain, the above error may be formulated as

$$E_{yaw} = \left\| \theta_{z,k+1} - \hat{\theta}_{z,k+1,highpass} \right\|_2 \tag{3.7}$$

where $\hat{\theta}_{z,k+1,highpass} = \theta_{z,k} + \hat{\omega}_{z,k+1,highpass} \cdot T$.

According to (3.3), such two-norm error representing the performance index of yaw motion may be expressed as a quadratic equation:

$$f_{yaw} = E_{yaw}{}^{T} Q_{yaw} E_{yaw} = \left[\theta_{z,k+1} - \hat{\theta}_{z,k+1,highpass} \right]^2 \tag{3.8}$$

Assume that $Q_{yaw} = 1$.

3.1.2 The Performance Index of a Combination of Pitch and Surge Motions

The pitch axis (*y*-axis) is perpendicular to the aircraft centerline, and lies in the plane of the wings. A pitch motion is an up or down movement of the nose of the aircraft. The 3-rotational-DOF motion simulator with yaw, pitch, and roll controls can also yield a high-frequency (onset) linear acceleration in either the *x* or the *y* direction, because the cockpit is offset from the pivot of the simulator mechanism by a height distance. The linear motion in the *x*-axis may be induced due to the presence of pitch motion (rotation about the *y*-axis).

This optimization problem attempts to improve the cues on the cockpit attitude and the linear onset cues along the *x*-axis simultaneously in real time. The tradeoff between these two

factors is determined by the weighting matrix $Q_{longitudinal}$. According to (3.4), the error vector can be expressed as

$$E_{longitudinal} = \begin{bmatrix} \left\| \theta_{y,k+1} - \hat{\theta}_{y,k+1} \right\|_2 \\ \left\| a_{x,k+1} - \hat{a}_{x,k+1} \right\|_2 \end{bmatrix} \tag{3.9}$$

Additionally, the otolith organs in the human vestibular system sense both the acceleration and tilting of the pilot's head with respect to the gravity vector [40]. Since the otoliths cannot discriminate between acceleration and tilt, this phenomenon, known as tilt coordination, can be adopted to improve motion simulation. This additional cue results from passing the vehicle acceleration through a low-pass filter to produce the desired long-duration tilt cue. Tilt coordination is implemented in a motion cueing algorithm by adding additional cross-feed channels with low-pass filters in the longitudinal (pitch/surge) and lateral (roll/sway) modes that produce the additional rotational cues. The low-frequency linear motion cues can thus be incorporated into the pitch angle to yield the following form of the error vector.

$$E_{longitudinal} = \begin{bmatrix} \left\| \theta_{y,k+1} - \left(\hat{\theta}_{y,k+1} - k_s \frac{\hat{a}_{x,k+1,lowpass}}{g} \right) \right\|_2 \\ \left\| a_{x,k+1,highpass} - \hat{a}_{x,k+1,highpass} \right\|_2 \end{bmatrix} \tag{3.10}$$

The angle obtained from low-frequency linear motions of axis *x* is scaled by the constant k_s based on the weight effect of the pilot. In the domain of discrete control, the above error vector can be expressed as

$$E_{longitudinal} = \begin{bmatrix} \left\| \theta_{y,k+1} - \left(\hat{\theta}_{y,k+1} - k_s \frac{\hat{a}_{x,k+1,lowpass}}{g} \right) \right\|_2 \\ \left\| \theta_{y,k+1} - \hat{\theta}_{y,k+1,highpass} \right\|_2 \end{bmatrix} \tag{3.11}$$

The angular acceleration of the pitch can be expressed in the discrete form as

$$\hat{\alpha}_{y,k+1,highpass} = \frac{\hat{\theta}_{y,k+1,highpass} - 2\theta_{y,k} + \theta_{y,k-1}}{T^2} \tag{3.12}$$

The relation between $\hat{a}_{x,k+1,highpass}$ and $\hat{\alpha}_{y,k+1,highpass}$ is

$$\hat{\alpha}_{y,k+1,highpass} = \frac{\hat{a}_{x,k+1,highpass}}{\ell_{pitch,k}} \tag{3.13}$$

where $\ell_{pitch,k}$ denotes the moment arm to the axis *y* (with respect to pitch angle) at step *k*.

Equations (3.12) and (3.13) can be combined to obtain

$$\hat{\theta}_{y,k+1,highpass} = \left(\frac{T^2}{\ell_{pitch,k}} \right) \cdot \hat{a}_{x,k+1,highpass} + 2\theta_{y,k} - \theta_{y,k-1} \tag{3.14}$$

The performance index of the pitch motion can be stated as

$$f_{longitudinal} = E_{longitudinal}{}^T \begin{bmatrix} 1 & 0 \\ 0 & W_{longitudinal,k} \end{bmatrix} E_{longitudinal} \tag{3.15}$$

where

$$E_{longitudinal} = \begin{bmatrix} \left\| \theta_{y,k+1} - \left(\hat{\theta}_{y,k+1} - k_s \frac{\hat{a}_{x,k+1,lowpass}}{g} \right) \right\|_2 \\ \left\| \theta_{y,k+1} - \hat{\theta}_{y,k+1,highpass} \right\|_2 \end{bmatrix}$$

The above equation can be expanded into

$$f_{longitudinal} = \left[\theta_{y,k+1} - b \right]^2 + W_{pitch,k} \left[\theta_{y,k+1} - c \right]^2 \tag{3.16}$$

where

$b = \hat{\theta}_{y,k+1} - \frac{k_s}{g} \cdot \hat{a}_{x,k+1,lowpass}$, and

$$c = \hat{\theta}_{y,k+1,highpass}$$

A particular weighting function is chosen as $W_{longitudinal,k} = K_p \cdot \left|\hat{a}_{x,k+1,highpass}\right| \cdot e^{-K_e\left|\theta_{y,k}\right|}$ where K_p and K_e are constants. The linear onset motion is associated with a small weighting when the simulator cab excurses to the boundary of the workspace, and a progressive increase in weighting as the simulator cab approaches its home position.

3.1.3 The Performance Index of a Combination of Roll and Sway Motions

The roll axis (*x*-axis) lies along the aircraft centerline. A roll motion is an up and down movement of the wings of the aircraft. According to (3.5), the performance index of the roll motion can be stated as

$$f_{lateral} = E_{lateral}{}^{T} \begin{bmatrix} 1 & 0 \\ 0 & W_{lateral} \end{bmatrix} E_{lateral} \tag{3.17}$$

where

$$E_{lateral} = \begin{bmatrix} \left\| \theta_{x,k+1} - \left(\hat{\theta}_{x,k+1} + k_s \dfrac{\hat{a}_{y,k+1,lowpass}}{g} \right) \right\|_2 \\ \left\| \theta_{x,k+1} - \hat{\theta}_{x,k+1,highpass} \right\|_2 \end{bmatrix}$$

The angular acceleration of the roll can be expressed in the discrete form as

$$\hat{\alpha}_{x,k+1,highpass} = \frac{\hat{\theta}_{x,k+1,highpass} - 2\theta_{x,k} + \theta_{x,k-1}}{T^2} \tag{3.18}$$

The relation between $\hat{a}_{y,k+1,highpass}$ and $\hat{\alpha}_{x,k+1,highpass}$ is

$$\hat{\alpha}_{x,k+1,highpass} = -\frac{\hat{a}_{y,k+1,highpass}}{\ell_{roll,k}} \tag{3.19}$$

where $\ell_{roll,k}$ denotes the moment arm to the axis *x* (which is respect to roll angle) at step *k*. Equations (3.18) and (3.19) can be combined to obtain

$$\hat{\theta}_{x,k+1,highpass} = \left(-\frac{T^2}{\ell_{roll,k}} \right) \cdot \hat{a}_{y,k+1,highpass} + 2\theta_{x,k} - \theta_{x,k-1} \tag{3.20}$$

The above equation can be expanded into

$$f_{lateral} = \left[\theta_{x,k+1} - b \right]^2 + W_{lateral,k} \left[\theta_{x,k+1} - c \right]^2 \tag{3.21}$$

where

$$b = \hat{\theta}_{x,k+1} + \frac{k_s}{g} \cdot \hat{a}_{y,k+1,lowpass}$$

$$c = \hat{\theta}_{x,k+1,highpass}$$

The weighting function may be chosen as $W_{lateral,k} = K_p \cdot \left| \hat{a}_{y,k+1,highpass} \right| \cdot e^{-K_e \left| \theta_{x,k} \right|}$ where K_p and K_e are constants.

3.2 Motion Cueing Strategy for the X-2/X360 Motion Simulator

Figure 6 shows the X-360 motion platform. This 3 rotational-DOF platform is a modified version of the original X-2 prototype. Figure 6 indicates that the yaw motion is performed by rotating the turntable through the additional third motor. The rotation of turntable is independent of the rest of the connecting mechanism. The inverse kinematic equations shown in Appendices A and D are adopted to convert the Cartesian space motion into the joint space control commands.

The workspace of the motion simulator is restricted by the mechanical structure. The

velocity of the motion simulator is limited by the driving system. A motion cueing strategy must be able to confine the simulator cab within the workspace, providing that the driving system is not over-speeding at all instances. Since different mechanisms and driving systems may yield different bounds and limitations, this study formulates the constraints in terms of the cockpit coordinates, i.e. Z-Y-X Euler angles, for general cases.

3.2.1 Real-Time Motion Simulation Structure

Figure 7 shows the real-time motion simulation structure of the 3-rotational-DOF motion simulator. The operator control inputs drive a mathematical model of the virtual reality (VR) system, generates the vehicle states. Passing vehicle states through the real-time motion cueing strategy produces the desired motion cues and platform states. The desired platform states are then transformed from DOF space to actuator space, generating the realized commands to the three actuators by kinematics transformation. The actuator motion commands serve as input to the platform dynamics, resulting in the actual simulator motion.

3.2.2 Motion Cueing Strategy

The proposed motion cueing strategy comprises three branches of motion cues, as shown in Fig. 8. All branches are fed into a real-time optimal motion cueing algorithm (ROMA) for a motion optimization process. The first branch of the motion cue is the high-frequency (onset)

linear motion; the second branch is the low frequency (sustained) linear motion, and the third branch is the angular motion cue. The classical washout filter (CLWF) converts the sustained motion into the residual tilt (rotation angle of the cockpit). The angular motion cue is then fed into the yawing washout filter, which is discussed in Section 3.4, and subsequently fed into the real-time optimal motion cueing algorithm (ROMA).

3.3 Real-time Optimal Motion Cueing Algorithm (ROMA)

Optimization theory and methods select the best alternative in the sense of the given objective function [41]. The real-time optimal motion cueing algorithm (ROMA) in this study involves minimizing the motion error where the inequality constraints of concerns are not violated.

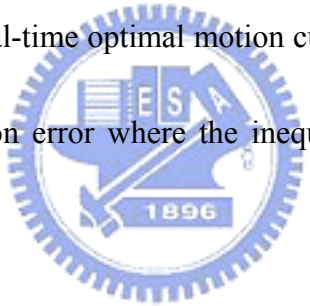

3.3.1 K-K-T Conditions

The KKT condition [41] is the necessary condition for the constrained optimization problem. Specifically, the points satisfying the KKT condition are considered as candidate minimizers. The cost (objective) function defined herein is in quadratic form, thus forming a convex optimization problem. The KKT condition also yields the sufficient condition of the global minimum. In sum, the KKT condition corresponding to the inequality constraints comprises four parts (two equalities and two inequalities):

(K1) $\boldsymbol{\mu}^* \geq \mathbf{0}$

(K2) $Df\left(\mathbf{x}^*\right) + \boldsymbol{\mu}^{*T} D\mathbf{g}\left(\mathbf{x}^*\right) = \mathbf{0}^T$

(K3) $\boldsymbol{\mu}^{*T}\mathbf{g}\left(\mathbf{x}^*\right) = \bar{0}$

(K4) $\mathbf{g}\left(\mathbf{x}^*\right) \leq \mathbf{0}$

3.3.2 Optimization on Yaw Motion

The constraint vector of mechanical boundaries and velocity limitations can be expressed as follows:

$$\mathbf{g} = \begin{bmatrix} {\theta_{z,k+1}}^2 - {\theta_{z,bound}}^2 \\ \left(\theta_{z,k+1} - \theta_{z,k}\right)^2 - {\omega_{z,bound}}^2 \cdot T^2 \end{bmatrix} \tag{3.22}$$

The optimization problem can be stated as

$$\begin{aligned} &\min \quad f_{yaw} \\ &s.t. \quad \mathbf{g} \leq 0 \end{aligned} \tag{3.23}$$

The condition K1 yields

$$\boldsymbol{\mu}^* = \begin{bmatrix} \mu_1^* \\ \mu_2^* \end{bmatrix} \geq \mathbf{0} \tag{3.24}$$

The condition K2 yields

$$\theta_{z,k+1}^* = \frac{\hat{\theta}_{z,k+1,highpass} + \mu_2^* \theta_{z,k}}{1 + \mu_1^* + \mu_2^*} \tag{3.25}$$

The condition K3 yields

$$\mu_1^* \left({\theta_{z,k+1}^*}^2 - {\theta_{z,bound}}^2\right) + \mu_2^* \left[\left(\theta_{z,k+1}^* - \theta_{x,k}\right)^2 - \left(\omega_{z,bound} T\right)^2\right] = 0 \tag{3.26}$$

The condition K4 yields

$$\begin{cases} {\theta^*_{z,k+1}}^2 - {\theta_{z,bound}}^2 \le 0 \\ \left(\theta^*_{z,k+1} - \theta_{x,k}\right)^2 - \left(\omega_{z,bound} T\right)^2 \le 0 \end{cases} \tag{3.27}$$

Substituting the conditions of (3.27) into (3.26) indicates that conditions $\mu_1^* > 0$ and $\mu_2^* > 0$ cannot both exist simultaneously. Thus, the optimum solution can be obtained from one of the three cases as follows:

Case 1: $\mu_1^* = 0$, $\mu_2^* = 0$. According to (3.25), we obtain that

$$\theta^*_{z,k+1} = \hat{\theta}_{z,k+1,highpass} \tag{3.28}$$

Case 2: $\mu_1^* > 0$, $\mu_2^* = 0$. According to (3.25) and (3.26), we obtain that

$$\theta^*_{z,k+1} = \pm\theta_{z,bound} \tag{3.29}$$

providing that

$$\mu_1^* = \frac{\hat{\theta}_{z,k+1,highpass} - \theta^*_{z,k+1}}{\theta_{z,bound}} > 0 \tag{3.30}$$

Case 3: $\mu_1^* = 0$, $\mu_2^* > 0$. According to (3.25) and (3.26), we obtain that

$$\theta^*_{z,k+1} = \theta_{z,k} \pm \omega_{z,bound} T \tag{3.31}$$

providing that

$$\mu_2^* = \frac{\hat{\theta}_{z,k+1,highpass} - \theta^*_{z,k+1}}{\omega_{z,bound} T} > 0 \tag{3.32}$$

Figure 9 shows the yaw motion optimization process with the yawing washout filter discussed in Section 3.4.

3.3.3 Optimization on Pitch and Surge Motion

The constraint vector of mechanical boundaries and velocity limitations can be expressed as follows:

$$\mathbf{g} = \begin{bmatrix} {\theta_{y,k+1}}^2 - {\theta_{y,bound}}^2 \\ \left(\theta_{y,k+1} - \theta_{y,k}\right)^2 - {\omega_{y,bound}}^2 \cdot T^2 \end{bmatrix} \tag{3.33}$$

The optimization problem can be stated as

$$\begin{aligned} &\min \quad f_{longitudinal} \\ &s.t. \quad \mathbf{g} \le 0 \end{aligned} \tag{3.34}$$

The condition K1 yields

$$\boldsymbol{\mu}^* = \begin{bmatrix} \mu_1^* \\ \mu_2^* \end{bmatrix} \ge \mathbf{0} \tag{3.35}$$

The condition K2 yields

$$\theta_{y,k+1}^* = \frac{b + W_{longitudinal,k} \cdot c + \mu_2^* \theta_{y,k}}{1 + W_{longitudinal,k} + \mu_1^* + \mu_2^*} \tag{3.36}$$

The condition K3 yields

$$\mu_1^* \left({\theta_{y,k+1}^*}^2 - {\theta_{y,bound}}^2\right) + \mu_2^* \left[\left(\theta_{y,k+1}^* - \theta_{y,k}\right)^2 - \left(\omega_{y,bound} T\right)^2\right] = 0 \tag{3.37}$$

The condition K4 yields

$$\begin{cases} {\theta_{y,k+1}^*}^2 - {\theta_{y,bound}}^2 \le 0 \\ \left(\theta_{y,k+1}^* - \theta_{y,k}\right)^2 - \left(\omega_{y,bound} T\right)^2 \le 0 \end{cases} \tag{3.38}$$

Substituting the conditions of (3.38) into (3.37) indicates that conditions $\mu_1^* > 0$ and $\mu_2^* > 0$ cannot both exist simultaneously. Thus, the optimum solution can be obtained from one of the three cases as follows:

Case 1: $\mu_1^* = 0$, $\mu_2^* = 0$. According to (3.36), we obtain that

$$\theta_{y,k+1}^* = \frac{b + W_{longitudinal,k} \cdot c}{1 + W_{longitudinal,k}} \tag{3.39}$$

Case 2: $\mu_1^* > 0$, $\mu_2^* = 0$. According to (3.36) and (3.37), we obtain that

$$\theta_{y,k+1}^* = \pm\theta_{y,bound}$$

providing that

$$\mu_1^* = \frac{b + W_{longitudinal,k} \cdot c - \left(1 + W_{longitudinal,k}\right)\theta_{y,k+1}^*}{\theta_{y,bound}} > 0 \tag{3.40}$$

Case 3: $\mu_1^* = 0$, $\mu_2^* > 0$. According to (3.36) and (3.37), we obtain that

$$\theta_{y,k+1}^* = \theta_{y,k} \pm \omega_{y,bound} T \tag{3.41}$$

providing that

$$\mu_2^* = \frac{b + W_{longitudinal,k} \cdot c - \left(1 + W_{longitudinal,k}\right)\theta_{y,k+1}^*}{\omega_{y,bound} T} > 0 \tag{3.42}$$

Figure 10 shows the pitch motion optimization process.

3.3.4 Optimization on Roll and Sway Motion

The constraint vector of mechanical boundaries and velocity limitations can be expressed as follows:

$$\mathbf{g} = \begin{bmatrix} \theta_{x,k+1}^{\ 2} - \theta_{x,bound}^{\ 2} \\ \left(\theta_{x,k+1} - \theta_{x,k}\right)^2 - \omega_{x,bound}^{\ 2} \cdot T^2 \end{bmatrix} \tag{3.43}$$

The optimization problem can be stated as

$$\begin{aligned} &\min \quad f_{lateral} \\ &s.t. \quad \mathbf{g} \le 0 \end{aligned} \tag{3.44}$$

The condition K1 yields

$$\boldsymbol{\mu}^* = \begin{bmatrix} \mu_1^* \\ \mu_2^* \end{bmatrix} \ge \mathbf{0} \tag{3.45}$$

The condition K2 yields

$$\theta_{x,k+1}^* = \frac{b + W_{lateral,k} \cdot c + \mu_2^* \theta_{x,k}}{1 + W_{lateral,k} + \mu_1^* + \mu_2^*} \tag{3.46}$$

The condition K3 yields

$$\mu_1^* \left({\theta_{x,k+1}^*}^2 - {\theta_{x,bound}}^2 \right) + \mu_2^* \left[\left(\theta_{x,k+1}^* - \theta_{x,k} \right)^2 - \left(\omega_{x,bound} T \right)^2 \right] = 0 \tag{3.47}$$

The condition K4 yields

$$\begin{cases} {\theta_{x,k+1}^*}^2 - {\theta_{x,bound}}^2 \le 0 \\ \left(\theta_{x,k+1}^* - \theta_{x,k} \right)^2 - \left(\omega_{x,bound} T \right)^2 \le 0 \end{cases} \tag{3.48}$$

Similarly, substituting the conditions of (3.48) into (3.47) indicates that conditions $\mu_1^* > 0$ and $\mu_2^* > 0$ cannot both exist simultaneously. Thus, the optimum solution can be obtained from one of the three cases as follows:

Case 1: $\mu_1^* = 0$, $\mu_2^* = 0$. According to (3.46), we obtain that

$$\theta_{x,k+1}^* = \frac{b + W_{lateral,k} \cdot c}{1 + W_{lateral,k}} \tag{3.49}$$

Case 2: $\mu_1^* > 0$, $\mu_2^* = 0$. According to (3.46) and (3.47), we obtain that

$$\theta_{x,k+1}^* = \pm \theta_{x,bound} \tag{3.50}$$

providing that

$$\mu_1^* = \frac{b + W_{lateral,k} \cdot c - \left(1 + W_{lateral,k}\right)\theta_{x,k+1}^*}{\theta_{x,bound}} > 0 \tag{3.51}$$

Case 3: $\mu_1^* = 0$, $\mu_2^* > 0$. According to (3.46) and (3.47), we obtain that

$$\theta_{x,k+1}^* = \theta_{x,k} \pm \omega_{x,bound} T \tag{3.52}$$

providing that

$$\mu_2^* = \frac{b + W_{lateral,k} \cdot c - \left(1 + W_{lateral,k}\right)\theta_{x,k+1}^*}{\omega_{x,bound} T} \tag{3.53}$$

Figure 11 shows the roll motion optimization process. Figure 12 shows the procedure of applying the KKT condition in practice.

3.3.5 Physical Meaning of Each Case of the Optimization

Each optimization task has three cases when applying the KKT conditions. Taking pitch motion as an example, if the pitch motion reaches its workspace bound then $\mu_1^* > 0$, otherwise $\mu_1^* = 0$. If the velocity of the pitch motion reaches its maximum allowable value, then $\mu_2^* > 0$, otherwise $\mu_2^* = 0$.

Subject to individual optimization tasks, in case #1, $\mu_1^* > 0$ and $\mu_2^* > 0$, is applied at the instance of real-time computation that neither the workspace boundary nor the velocity constraint is violated, while in case #2, $\mu_1^* > 0$ and $\mu_2^* = 0$, is applied at the instance that the velocity constraint is not violated when the workspace bound is reached. For example, the

pitch angle is sustained at its maximum pitch angle when the maximum allowable pitch angle is reached, otherwise the corresponding position constraint is violated. The case #3, $\mu_1^* = 0$ and $\mu_2^* > 0$, is applied when the velocity constraint is violated, thus limiting the corresponding motion to the maximum velocity.

3.4 Washout Filtering

Washout must provide a high pass filtering scheme to limit the simulator cab excursions. The washout filters in the proposed algorithm include the yaw and adaptive filters as stated in the following sections.

3.4.1 Yawing Washout Filter

The yawing washout filter is applied to prevent the yawing angle at step (*k+1*) from passing beyond the limits of the motion simulator workspace before the optimization process ROMA takes place, as shown in Fig. 8. If the norm of the new yawing angular velocity is less than the indifference threshold, then the proposed yawing washout motion is in action.

$$\text{If } \left|\hat{\omega}_{z,k+1,highpass}\right| \le \omega_{z,indiff} \text{ then } \begin{cases} \omega_{z,k+1} = -sign\left(\theta_{z,k}\right)\cdot\omega_{z,indiff} \\ and \\ \theta_{z,k+1} = \theta_{z,k} - \left[sign\left(\theta_{z,k}\right)\cdot\omega_{z,indiff}\cdot T\right] \end{cases} \tag{3.54}$$

The yawing washout filter continuously returns the cockpit to its home position, where the dexterity of motion is highest.

3.4.2 Adaptive Washout Filter

The optimization algorithm guarantees that the simulator cockpit not to exceed the workspace. However, this guarantee may fail in practice for the following reasons:

(1) The sampling frequency may not be stable, due to the high CPU loading subjected to the VR rendering.

(2) The workspace boundaries may be too complex to calculate the exact mechanical bounds. (see the kinematics in the Appendices A, B, C, and D).

An adaptive washout filter, as shown in Fig. 8, is proposed to compensate for the insufficiency of the prior proposed optimization process, and this accommodates more severe restrictions, such as the small workspace and the limited driving current. For yaw motion, the washout filter is implemented as follows.

$$\theta_{z,k+1} = \theta_{z,k} - \left[sign\left(\theta_{z,k}\right) \cdot \omega_{z,indiff} \cdot T \right] \quad \text{if} \quad \left|\theta_{z,k}\right| > \theta_{z,softwarebound} \tag{3.55}$$

The following filter is applied to prevent the hunting motion from being possibly associated with the washout motion.

$$\theta_{z,k+1} = 0 \quad \text{if} \quad \begin{cases} \theta_{z,k} \cdot \theta_{z,k+1} < 0 \\ or \\ \left|\theta_{z,k+1}\right| \le \varepsilon \end{cases} \tag{3.56}$$

where ε denotes a sufficiently small number. For the pitch and roll motion, further motion is prohibited as soon as the software limit of the workspace (in contrast to the hardware limit

(actual boundary) of the workspace) is reached. These filters may be formulated as follows.

$$\theta_{x,k+1} = \theta_{x,k} \quad \text{if} \quad \left|\theta_{x,k}\right| > \theta_{x,softwarebound} \tag{3.57}$$

$$\theta_{y,k+1} = \theta_{y,k} \quad \text{if} \quad \left|\theta_{y,k}\right| > \theta_{y,softwarebound} \tag{3.58}$$

Chapter 4 Simulation and Experimental Results

Figure 13 shows an experimental X-2 motion platform. The spread-angle range can be adjusted from 21° to 69°. Fig. 14 shows the maximum pitch and roll angles with different spread-angles, revealing that the maximum pitch angle rises and the maximum roll angle falls as the spread-angle rises. Fig. 15 shows the workspaces for different spread-angle settings. For instance, the maximum roll angle can reach about 21° but the maximum pitch angle falls to about 8° when the spread-angle ϕ = 21°. The maximum pitch angle remains to 21° while the maximum roll angle falls to 7.5°, when the spread-angle reaches ϕ = 69°. The different spread-angles result in a tradeoff between maximum roll and pitch angles.

Figure 16 shows the spread-angle that satisfies the workspace symmetry condition. The intersection point indicates that the spread-angle of a symmetrical workspace is 41.9°.

Figure 17 shows the variation of kinetic energy between different spread-angles, revealing that the kinetic energy rises as the spread-angle rises, and the slope becomes steeper for large spread-angles.

Figures 18 and 19 show the potential energy and the variation of gradient of potential energy between different spread-angles. Fig. 18 shows the potential energy field for different spread-angles, in which the arrows point toward the direction of rising potential energy. Fig. 20 shows the variation of the 2-norm of gradient of potential energy between different spread-angles. These figures indicate that the potential energy rises rapidly in two cases: when

both sliders go forward to their traversal limits, or when one slider goes forward and the other goes backward to the traversal limits. The first case presents a large pitch angle, and the second case exhibits a large roll angle. Thus, the slopes with maximum potential energy only occur at the maximum pitch or roll angle. Fig. 21 indicates that the maximum kinetic energy occurs at the largest spread-angle, and the minimum kinetic energy occurs at the smallest spread-angle. Fig. 22 indicates that the minimum variation of potential energy occurs at about ϕ = 33°.

The individual performance indices are described qualitatively in the previous sequels. The optimization was applied to cost function and fitness by the genetic algorithm for different purposes, and with different weights. Four sets of weights were adopted for different applications: (i) workspace symmetry, (ii) minimizing the infinity norm of the kinetic energy, (iii) minimizing the infinity norm of the gradient of potential energy, and (iv) multi-objective optimization.

Application (i) emphasized the workspace symmetry, with weights w_b = 80, w_T = 10, w_V = 10. The GA optimization yielded ϕ = 41.94° after 100 generations of searching.

Application (ii) emphasized minimizing the infinity norm of the kinetic energy, and adopted weights w_b = 10, w_T = 80, w_V = 10. The GA optimization yielded ϕ = 21.22° after 100 generations of searching.

Application (iii) emphasized minimizing the infinity norm of the gradient of potential

energy, and weights w_b = 10, w_T = 10, w_V = 80. The GA optimization yielded ϕ = 33.49° after 100 generations of searching.

Application (iv) was subjected to a specific multi-objective optimization, and adopted weights of w_b = 40, w_T = 30, w_V = 30. The GA optimization yielded ϕ = 36.53° after 100 generations of searching.

Figures 23, 24, 25 and 26 show analytical results for individual applications. Subplot (a) shows how the genetic algorithm generates the new best so far solution at each generation. Subplot (b) shows the workspace. Subplot (c) shows the potential energy. Subplot (d) shows the gradient of potential energy. Subplot (e) shows the norm of the potential energy gradient. The Subplot (f) shows the kinetic energy.

A simulation of Pseudo-Flight-Object (PFO) produced by IMON Corp. was applied in this study. The geocentric position and the body acceleration data of the aircraft produced from the equation of motion (EOM), were taken as inputs to the proposed motion cueing strategy in the PFO software. The outputs of the experiment were the motor position commands to the 3-rotational-DOF motion simulator, as shown in Fig. 27. The results were compared to the classical washout filter (CLWF). Figure 28 consists of four plots used to demonstrate the flight trajectory in 3-D view, front view, side view, and top view, respectively. The flight data including longitudinal (pitch + x-acceleration), lateral (roll + y-acceleration), and yaw motions. Data of individual Euler angles (yaw, pitch and roll) were provided

simultaneously to the proposed ROMA algorithm to yield the motion cue of the pilot. Hence, one complex simulation was performed to test all motion cues simultaneously.

Various aspects of the experimental results are shown. The real-time optimal motion-cueing algorithm (ROMA) introduced in this paper is derived from the classical washout filter (CLWF), which is depicted in Fig. 8. ROMA should perform similar sustained motions, or low-frequency linear motions, to CLWF. The sustained motion activates only the attitude and the residual tilt control, for which the calculation is mainly derived from the CLWF method. There is merely difference when comparing the performances of sustained motion along the *x* and *y* axes between these two methods.

However, the CLWF is designed for the general 6-DOF motion simulator. The ROMA is designed for a 3-DOF flight simulator, specifically the rotational motion simulator with insufficient spatial DOF. The CLWF shows poor performance on the high-frequency linear motion when implemented on the rotational motion simulator.

Figures 29 and 30 show the comparison of the high-frequency (onset) linear motion cues along the *x* and *y* axes. In this case, the CLWF generates no output to the rotation motion. The proposed algorithm ROMA eventually converts the onset linear motion to a rotation command based on (3.14) and (3.20), and presents the onset linear motion on the motion simulator. Figures 31 and 32 show the error between VR commands and actual linear acceleration by different motion cueing algorithms. The data indicate that the error rises rapidly as the

frequency of the linear motion increases when adopting the classical method.

Figures 33 and 34 show the results of a mixture of sustained and onset motion. The ROMA could optimize the motion cueing without violating the inequality equation, and remained within to the mechanical bounds of a motion simulator. The CLWF failed to do so; therefore, the mechanical structure of the motion simulator can be damaged by CLWF. Nevertheless, these figures indicate that the onset motion cue can be generated by ROMA rather than CLWF.

Figure 35 illustrates the effect of the yawing washout and ROMA. The washout motion continuously returns the cockpit to its home position when the indifference threshold is detected as in (3.54). The washout motion moving the cockpit back to its home position is performed with a velocity at the indifference threshold, as revealed in Fig. 36.

Chapter 5 Conclusion

This study first establishes a performance index for workspace and mechanical advantage. These performance indices are useful in designing motion platforms. Global optimal search techniques, based on GA, enable the desired motion platform to yield a large and symmetrical workspace, and reduce the power requirement. In addition to the optimization process, weighting functions were designed to correlate explicitly with the needs of different simulation applications. The X-series motion platforms are flexible, allowing manufacturers to adjust the spread-angle for different simulation scenarios. For instance, a video game application requires a symmetrical workspace to present sustained motion cues for low-frequency motion plus residual tilt. Accordingly, the spread-angle is recommended to be set at ϕ = 41.94°. A professional motion simulation system needs to achieve high-G motion (the onset motion cue for high-frequency motion), and requires a spread angle of ϕ = 21.22° to increase the mechanical advantage. After designing and analyzing the structure of the mechanism, this study then establishes a performance index for the motion of the motion simulator. This motion performance index is useful for planning motion control. By introducing the constrained optimization algorithm ROMA, motion control yields a precise cue to the pilot, and avoids damaging the mechanical structure of the motion simulator. In addition to the motion optimization process, washout filters are employed to ensure motion dexterity, and prevent unexpected damage due to loss of control motions resulting from high

CPU loading. Repeated tests, which were performed online, indicate that the proposed motion-cueing strategy yields more realistic motion than the classical strategy via the motion simulator with three rotational DOF (3-DOF). The proposed motion-cueing strategy is applicable to all motion simulators with rotational DOF.

The proposed method is designed for not only the X-series simulator, but also any other kinds of simulators with rotational DOF. Specifically, the rotational motion simulator has insufficient spatial DOF. The conventional motion cueing methods, such as the CLWF, failed to perform the high-frequency linear motion toward the rotational motion simulator. Thus, the aforementioned optimal algorithms based on CLWF are also not appropriate for 3-rotational-DOF motion simulators.

Since the optimal motion cueing for rotational DOF motion simulators has not yet been uncovered; the result is only compared with CLWF to avoid bias judgments of different approaches. Nevertheless, the detail experimental setup data and hardware specifications are provided to assist future work on rotational DOF motion simulators by enabling researchers to compare their results with those of ROMA in our study.

The computation time of the motion control is indeed less than 1% of CPU time steadily. Table 3 indicates that the CPU time for VR rendering process is in the range 50%–60%, depending on the graphical complexity. The graphical output of the simulation is based on the DirectX environment. Different number of polygons and their texture patches need to be onto

the screen for different scenes, such as the runway and buildings. Thus, the VR rendering time can vary. Notably, the motion control remains stable at the graphical loading shown in Table 3.

Figure 37 includes subjective feedback with five significant characteristics of flight simulators from different users. The result shows that the proposed algorithm performs more realistic cues in longitudinal and lateral acceleration/deceleration and also the special effect of the onset cues.

To perform a realistic human-machine interactive motion for entertainment demands, this dissertation finally describes the realization of the system integration. Figure 38 shows the complete framework of the electrical and mechanical system of the aforementioned X-series motion simulator. This framework is applicable to the lost-cost flight simulation purpose. Figure 39 shows a complete implementation of the simulator system. This simulator system is a single/double-seat version suitable for either entertainment use or training entry-level pilots.

Appendix

A. *Inverse Kinematics of the X-2 Motion Platform*

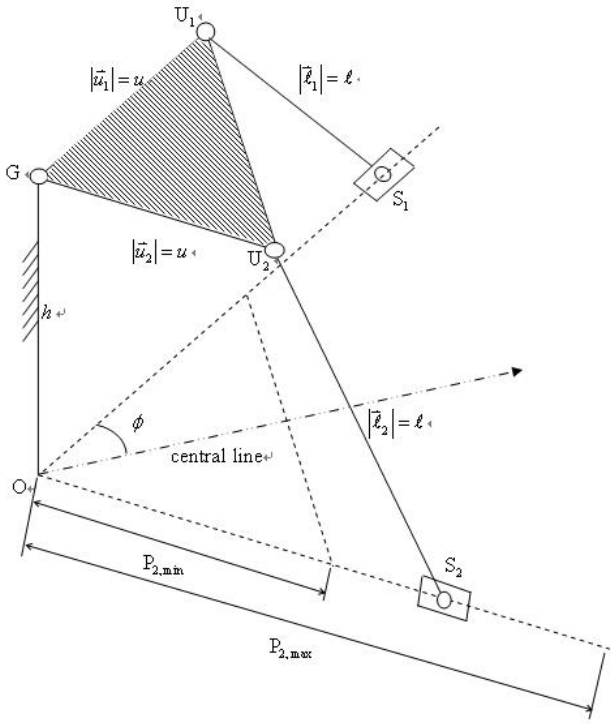

The rotation matrix is expressed as

$$\mathbf{R}(0,\beta,\gamma) = \begin{bmatrix} c\beta & s\beta s\gamma & s\beta c\gamma \\ 0 & c\gamma & -s\gamma \\ -s\beta & c\beta s\gamma & c\beta c\gamma \end{bmatrix} \tag{A1}$$

Derived from the geometrical relation, it is obtained that

$${}^{G}\vec{u}_i = \begin{bmatrix} {}^{G}u_{i,x} & {}^{G}u_{i,y} & {}^{G}u_{i,z} \end{bmatrix}^T = \mathbf{R} \cdot {}^{G}\vec{u}_{i,initial}\,, \tag{A2}$$

$${}^{O}u_i = \begin{bmatrix} {}^{O}u_{i,x} & {}^{O}u_{i,y} & {}^{O}u_{i,z} \end{bmatrix} = \overrightarrow{\mathbf{OG}} + \mathbf{R} \cdot {}^{G}u_{i,initial}\,, \tag{A3}$$

$$\vec{p}_i = p_i \begin{bmatrix} \cos\phi & (-1)^{i+1}\sin\phi & 0 \end{bmatrix}, \tag{A4}$$

$$\vec{\ell}_i = {}^{O}\vec{u}_i - \vec{p}_i\,, \tag{A5}$$

where $p_i = |\vec{p}_i|$. According to the cosine law we have

$$h^2 + p_i^2 = r_u^2 + \ell^2 - 2\,{}^{\mathbf{G}}\vec{u}_i \cdot \vec{\ell}_i^{\,T}. \tag{A6}$$

Equation (A6) is rearranged as

$$\begin{aligned} & p_i^2 \underbrace{- 2({}^{G}u_{i,x}\cos\phi + (-1)^{i+1} \cdot {}^{G}u_{i,y}\sin\phi)}_{B} p_i \\ & + \underbrace{h^2 - u^2 - l^2 + 2(u_{i,x}^{\mathbf{G}} \cdot u_{i,x}^{\mathbf{O}} + u_{i,y}^{\mathbf{G}} \cdot u_{i,y}^{\mathbf{O}} + u_{i,z}^{\mathbf{G}} \cdot u_{i,z}^{\mathbf{O}})}_{C} = 0 \end{aligned}, \tag{A7}$$

to yield

$$p_i = \left(-B \pm \sqrt{B^2 - 4C}\right)/2. \tag{A8}$$

Since (A8) are skew solutions about the kinematic singularity, only the feasible solution is chosen, namely

$$p_i = \left(-B + \sqrt{B^2 - 4C}\right)/2. \tag{A9}$$

B. Forward Kinematics of the X-2 Motion Platform

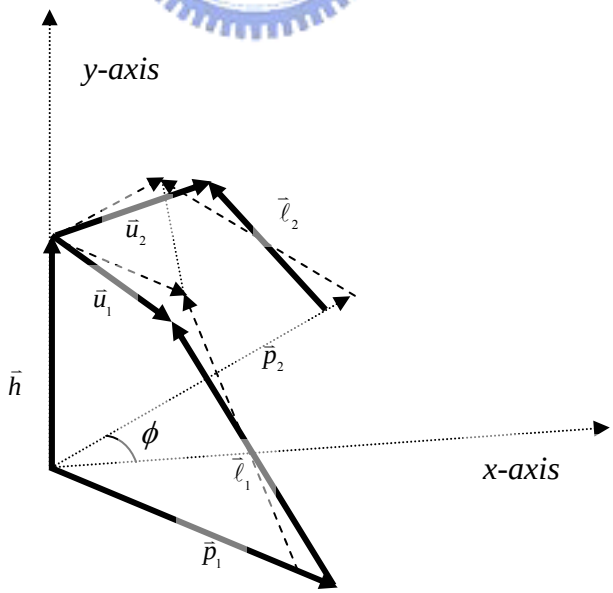

According to the cosine law yields

$$h^2 + p_i^2 = u^2 + \ell^2 - 2\vec{u}_i \cdot \vec{\ell}_i \tag{B1}$$

where

$$i = 1, 2$$

$$\vec{u}_i = \mathbf{R}\vec{u}_{i,0}$$

$$\vec{\ell}_i = \mathbf{R}\vec{u}_{i,0} + \vec{h} - \vec{p}_i$$

Equation (B1) can be expanded into

$$2\left(\mathbf{R}\vec{u}_{i,0}\right)\cdot\left(\mathbf{R}\vec{u}_{i,0} + \vec{h} - \vec{p}_i\right) = u^2 + \ell^2 - h^2 - p_i^2, \tag{B2}$$

we have

$$(\mathbf{R}\vec{u}_{i,0})\cdot\underbrace{(\vec{h} - \vec{p}_i)}_{\vec{b}_i} = \underbrace{(\ell^2 - h^2 - p_i^2 - u^2)/2}_{c_i}. \tag{B3}$$

Equation (B3) yields

$$\vec{b}_i^T\mathbf{R}\vec{u}_{i,0} = c_i, \tag{B4}$$

where

$$\vec{u}_{i,0} = u\begin{bmatrix} c\phi & (-1)^{i+1}s\phi & 0\end{bmatrix}^T$$

$$\vec{p}_i = p_i\begin{bmatrix} c\phi & (-1)^{i+1}s\phi & 0\end{bmatrix}^T$$

$$\vec{h} = \begin{bmatrix}0 & 0 & h\end{bmatrix}^T$$

$$\vec{b}_i = \vec{h} - \vec{p}_i = \begin{bmatrix} -p_i c\phi & -(-1)^{i+1}p_i s\phi & h\end{bmatrix}^T.$$

Equations (A1) and (B4) give

$$\begin{bmatrix} -p_i c\phi \\ (-1)^i p_i s\phi \\ h\end{bmatrix}^T\begin{bmatrix} c\beta & s\beta s\gamma & s\beta c\gamma \\ 0 & c\gamma & -s\gamma \\ -s\beta & c\beta s\gamma & c\beta c\gamma\end{bmatrix}\begin{bmatrix} c\phi \\ (-1)^{i+1}s\phi \\ 0\end{bmatrix} = \frac{c_i}{u}. \tag{B5}$$

Equation (B5) is then expanded into

$$\begin{aligned}&(-p_i c\beta c\phi^2 - p_i c\gamma s\phi^2 - hs\beta c\phi \\ &\quad + (-1)^i p_i s\beta s\gamma s\phi c\phi + (-1)^{i+1} hc\beta s\gamma s\phi) = c_i / u\end{aligned}, \tag{B6}$$

which is summarized into

$$\begin{cases} -c\beta - t\phi s\beta s\gamma - t\phi^2 c\gamma - \underbrace{\frac{h}{p_1 c\phi}}_{v} s\beta + t\phi \underbrace{\frac{h}{p_1 c\phi}}_{v} c\beta s\gamma = \underbrace{\frac{c_1}{up_1 c\phi^2}}_{V} \\ -c\beta + t\phi s\beta s\gamma - t\phi^2 c\gamma - \underbrace{\frac{h}{p_2 c\phi}}_{w} s\beta - t\phi \underbrace{\frac{h}{p_2 c\phi}}_{w} c\beta s\gamma = \underbrace{\frac{c_2}{up_2 c\phi^2}}_{W} \end{cases} \tag{B7}$$

Equation (B7) is rearranged as follows:

$$\begin{cases} -t\phi^2 c\gamma + \left(t\phi v c\beta - t\phi s\beta\right) s\gamma = c\beta + vs\beta + V \\ -t\phi^2 c\gamma + \left(-t\phi w c\beta + t\phi s\beta\right) s\gamma = c\beta + ws\beta + W \end{cases}. \tag{B8}$$

Equation (B8) gives

$$t\phi \begin{bmatrix} -t\phi & vc\beta - s\beta \\ -t\phi & -wc\beta + s\beta \end{bmatrix} \begin{bmatrix} c\gamma \\ s\gamma \end{bmatrix} = \begin{bmatrix} c\beta + vs\beta + V \\ c\beta + ws\beta + W \end{bmatrix}. \tag{B9}$$

Equation (B9) yields

$$\begin{bmatrix} c\gamma \\ s\gamma \end{bmatrix} = \frac{1}{t\phi} \begin{bmatrix} -t\phi & vc\beta - s\beta \\ -t\phi & -wc\beta + s\beta \end{bmatrix}^{-1} \begin{bmatrix} c\beta + vs\beta + V \\ c\beta + ws\beta + W \end{bmatrix}, \tag{B10}$$

then (B11) is given by

$$\begin{bmatrix} c\gamma \\ s\gamma \end{bmatrix} = \frac{\begin{bmatrix} 2 \cdot I \cdot s\beta^2 + 2 \cdot J \cdot c\beta s\beta - K \cdot c\beta + L \cdot s\beta - I \\ -t\phi\left(M \cdot s\beta - N\right) \end{bmatrix}}{t\phi^2 \left(I \cdot c\beta - 2s\beta\right)}, \tag{B11}$$

where

$$I = v + w$$

$$J = 1 - wv$$

$$K = wV + vW$$

$$L = V + W$$

$$M = w - v$$

$$N = W - V\ .$$

According to (B11) and the following relation

$$\sin^2\gamma + \cos^2\gamma = s\gamma^2 + c\gamma^2 = 1 \tag{B12}$$

yields

$$\begin{aligned} & s_4 \cdot s\beta^4 + s_3 \cdot s\beta^3 + s_2 \cdot s\beta^2 + s_1 \cdot s\beta + s_0 \\ & \quad + t_3 \cdot c\beta s\beta^3 + t_2 \cdot c\beta s\beta^2 + t_1 \cdot c\beta s\beta + t_0 \cdot c\beta = 0 \end{aligned} \tag{B13}$$

where

$$s_4 = 4I^2 - 4J^2$$

$$s_3 = 4JK + 4IL$$

$$s_2 = (t\phi^4 - 4)I^2 + 4J^2 - K^2 + L^2 + t\phi^2 M^2 - 4t\phi^4$$

$$s_1 = -4JK - 2IL + 2t\phi^2 MN$$

$$s_0 = (1 - t\phi^4)I^2 + K^2 + t\phi^2 N^2$$

$$t_3 = 8IJ$$

$$t_2 = -4IK + 4JL$$

$$t_1 = 4t\phi^4 I - 4IJ - 2KL$$

$$t_0 = 2IK\ .$$

Equation (B13) is then rewritten as

$$\underbrace{(s_4 s\beta^4 + s_3 s\beta^3 + s_2 s\beta^2 + s_1 s\beta + s_0)}_{X} + \underbrace{(t_3 s\beta^3 + t_2 s\beta^2 + t_1 s\beta + t_0)}_{Y} c\beta = 0 \quad , \tag{B14}$$

which gives

$$X^2 - Y^2 + Y^2 s\beta^2 = 0 \tag{B15}$$

$\sin\beta$ is determined by (B15), and β can be obtained using function arc-sin. γ is then obtained by Substituting the obtained β into (B5)

C. Jacobian of the X-2 Motion Platform

Equations (A1)-(A6) give

$$(\mathbf{R}\vec{u}_{i,0}) \cdot \underbrace{(\vec{h} - \vec{p}_i)}_{\vec{b}_i} + p_i^2 / 2 = \underbrace{(\ell^2 - h^2 - u^2)/2}_{c}. \tag{C1}$$

Equation (C2) is then given by

$$\begin{bmatrix} -p_i c\phi \\ (-1)^i p_i s\phi \\ h \end{bmatrix}^T \begin{bmatrix} c\beta & s\beta s\gamma & s\beta c\gamma \\ 0 & c\gamma & -s\gamma \\ -s\beta & c\beta s\gamma & c\beta c\gamma \end{bmatrix} \begin{bmatrix} c\phi \\ (-1)^{i+1} s\phi \\ 0 \end{bmatrix} + \frac{p_i}{2u} = \frac{c}{u}, \tag{C2}$$

which is summarized into

$$\begin{cases} -p_1 c\beta - t\phi p_1 s\beta s\gamma - t\phi^2 p_1 c\gamma - vs\beta + t\phi vc\beta s\gamma + wp_1 = \dfrac{c}{uc\phi^2} \\ -p_2 c\beta + t\phi p_2 s\beta s\gamma - t\phi^2 p_2 c\gamma - vs\beta - t\phi vc\beta s\gamma + wp_2 = \dfrac{c}{uc\phi^2} \end{cases} \tag{C3}$$

where

$$v = h / c\phi$$

$$w = 1/2uc\phi^2 .$$

Differentiating (C3) with respect to p_1 and p_2 yields (C4) and (C5) as

$$\begin{bmatrix} A_{11} & A_{12} \\ A_{21} & A_{22} \end{bmatrix} \begin{bmatrix} \frac{\partial \beta}{\partial p_1} \\ \frac{\partial \gamma}{\partial p_1} \end{bmatrix} = \begin{bmatrix} A_{13} \\ 0 \end{bmatrix} \tag{C4}$$

$$\begin{bmatrix} B_{11} & B_{12} \\ B_{21} & B_{22} \end{bmatrix} \begin{bmatrix} \frac{\partial \beta}{\partial p_2} \\ \frac{\partial \gamma}{\partial p_2} \end{bmatrix} = \begin{bmatrix} B_{13} \\ 0 \end{bmatrix}. \tag{C5}$$

Equations (C6) and (C7) are then obtained as follows:

$$\begin{bmatrix} \frac{\partial \beta}{\partial p_1} \\ \frac{\partial \gamma}{\partial p_1} \end{bmatrix} = \begin{bmatrix} A_{11} & A_{12} \\ A_{21} & A_{22} \end{bmatrix}^{-1} \begin{bmatrix} A_{13} \\ 0 \end{bmatrix} \tag{C6}$$

$$\begin{bmatrix} \frac{\partial \beta}{\partial p_2} \\ \frac{\partial \gamma}{\partial p_2} \end{bmatrix} = \begin{bmatrix} B_{11} & B_{12} \\ B_{21} & B_{22} \end{bmatrix}^{-1} \begin{bmatrix} B_{13} \\ 0 \end{bmatrix}, \tag{C7}$$

where

$$A_{11} = p_1 \cdot s\beta - t\phi \cdot p_1 \cdot c\beta s\gamma - v \cdot c\beta - t\phi \cdot v \cdot s\beta s\gamma$$
$$A_{12} = t\phi^2 \cdot p_1 \cdot s\gamma - t\phi \cdot p_1 \cdot s\beta c\gamma + t\phi \cdot v \cdot c\beta c\gamma$$
$$A_{13} = c\beta + t\phi^2 \cdot c\gamma + t\phi \cdot s\beta s\gamma - w$$
$$A_{21} = p_2 \cdot s\beta + t\phi \cdot p_2 \cdot c\beta s\gamma - v \cdot c\beta + t\phi \cdot v \cdot s\beta s\gamma$$
$$A_{22} = t\phi^2 \cdot p_2 \cdot s\gamma + t\phi \cdot p_2 \cdot s\beta c\gamma - t\phi \cdot v \cdot c\beta c\gamma$$

$$B_{11} = p_2 \cdot s\beta + t\phi \cdot p_2 \cdot c\beta s\gamma - v \cdot c\beta + t\phi \cdot v \cdot s\beta s\gamma$$
$$B_{12} = t\phi^2 \cdot p_2 \cdot s\gamma + t\phi \cdot p_2 \cdot s\beta c\gamma - t\phi \cdot v \cdot c\beta c\gamma$$
$$B_{13} = c\beta + t\phi^2 \cdot c\gamma - t\phi \cdot s\beta s\gamma - w$$
$$B_{21} = p_1 \cdot s\beta - t\phi \cdot p_1 \cdot c\beta s\gamma - v \cdot c\beta - t\phi \cdot v \cdot s\beta s\gamma$$

$$B_{22} = t\phi^2 \cdot p_1 \cdot s\gamma - t\phi \cdot p_1 \cdot s\beta c\gamma + t\phi \cdot v \cdot c\beta c\gamma .$$

D. Additional Kinematics for X-360 (based on X-2)

α, β, and γ denote the Euler angles of X-360 (3-DOF platform); α', β', and γ' denote the based-angle (Euler angles of the original X-2 platform) of X-360.

(→): the **Euler angles are known**. The base-angles of X-360 (pitch & roll angles of the original X-2) are found as follows.

$$\begin{bmatrix} c\alpha c\beta & c\alpha s\beta s\gamma - s\alpha c\gamma & c\alpha s\beta c\gamma + s\alpha s\gamma \\ s\alpha c\beta & s\alpha s\beta' s\gamma + c\alpha c\gamma & s\alpha s\beta c\gamma - c\alpha s\gamma \\ -s\beta & c\beta s\gamma & c\beta c\gamma \end{bmatrix} \begin{bmatrix} 0 \\ 0 \\ 1 \end{bmatrix} = \begin{bmatrix} c\alpha' c\beta' & c\alpha' s\beta' s\gamma' - s\alpha' c\gamma' & c\alpha' s\beta' c\gamma' + s\alpha' s\gamma' \\ s\alpha' c\beta' & s\alpha' s\beta' s\gamma' + c\alpha' c\gamma' & s\alpha' s\beta' c\gamma' - c\alpha' s\gamma' \\ -s\beta' & c\beta' s\gamma' & c\beta' c\gamma' \end{bmatrix} \begin{bmatrix} 0 \\ 0 \\ 1 \end{bmatrix} \tag{D1}$$

Since $\alpha' = 0$, we obtain

$$\begin{bmatrix} c\alpha s\beta c\gamma + s\alpha s\gamma \\ s\alpha s\beta c\gamma - c\alpha s\gamma \\ c\beta c\gamma \end{bmatrix} = \begin{bmatrix} c\alpha' s\beta' c\gamma' + s\alpha' s\gamma' \\ s\alpha' s\beta' c\gamma' - c\alpha' s\gamma' \\ c\beta' c\gamma' \end{bmatrix} \tag{D2}$$

then

$$\begin{bmatrix} s\beta' c\gamma' \\ -s\gamma' \\ c\beta' c\gamma' \end{bmatrix} = \begin{bmatrix} c\alpha s\beta c\gamma + s\alpha s\gamma \\ s\alpha s\beta c\gamma - c\alpha s\gamma \\ c\beta c\gamma \end{bmatrix} = \begin{bmatrix} r_1 \\ r_2 \\ r_3 \end{bmatrix} \tag{D3}$$

yields

$$\beta' = \tan^{-1}\left(\frac{r_1}{r_3}\right), \quad \gamma = \sin^{-1}(-r_2) \tag{D4}$$

(←): the **base-angles are known**. The Euler angles are found as follows (notice that the **yaw** angle is known).

$$\mathbf{R(\alpha,\beta,\gamma) = R_z(\alpha)R_z(\beta)R_z(\gamma)}$$

$$= \begin{bmatrix} c\alpha c\beta & c\alpha s\beta s\gamma - s\alpha c\gamma & c\alpha s\beta c\gamma + s\alpha s\gamma \\ s\alpha c\beta & s\alpha s\beta s\gamma + c\alpha c\gamma & s\alpha s\beta c\gamma - c\alpha s\gamma \\ -s\beta & c\beta s\gamma & c\beta c\gamma \end{bmatrix}$$

$$= \begin{bmatrix} c\alpha & -s\alpha & 0 \\ s\alpha & c\alpha & 0 \\ 0 & 0 & 1 \end{bmatrix} \begin{bmatrix} c\beta & s\beta s\gamma & s\beta c\gamma \\ 0 & c\gamma & -s\gamma \\ -s\beta & c\beta s\gamma & c\beta c\gamma \end{bmatrix} \tag{D5}$$

we have

$$\begin{bmatrix} c\alpha & -s\alpha & 0 \\ s\alpha & c\alpha & 0 \\ 0 & 0 & 1 \end{bmatrix} \begin{bmatrix} c\beta & s\beta s\gamma & s\beta c\gamma \\ 0 & c\gamma & -s\gamma \\ -s\beta & c\beta s\gamma & c\beta c\gamma \end{bmatrix} \begin{bmatrix} 0 \\ 0 \\ 1 \end{bmatrix} = \begin{bmatrix} s\beta' c\gamma' \\ -s\gamma' \\ c\beta' c\gamma' \end{bmatrix} \tag{D6}$$

$$\begin{bmatrix} c\alpha & -s\alpha & 0 \\ s\alpha & c\alpha & 0 \\ 0 & 0 & 1 \end{bmatrix} \begin{bmatrix} s\beta c\gamma \\ -s\gamma \\ c\beta c\gamma \end{bmatrix} = \begin{bmatrix} s\beta' c\gamma' \\ -s\gamma' \\ c\beta' c\gamma' \end{bmatrix} \tag{D7}$$

then

$$\begin{bmatrix} s\beta c\gamma \\ -s\gamma \\ c\beta c\gamma \end{bmatrix} = \begin{bmatrix} c\alpha & -s\alpha & 0 \\ s\alpha & c\alpha & 0 \\ 0 & 0 & 1 \end{bmatrix}^{\mathrm{T}} \begin{bmatrix} s\beta' c\gamma' \\ -s\gamma' \\ c\beta' c\gamma' \end{bmatrix} = \begin{bmatrix} s_1 \\ s_2 \\ s_3 \end{bmatrix} \tag{D8}$$

yields

$$\gamma = \sin^{-1}(-s_2), \quad \beta = \tan^{-1}\left(\frac{s_1}{s_3}\right) \tag{D9}$$

References

[1] T. Yoshikawa, Translational and rotational manipulability of robotic manipulators. In: Presented at Proceedings of the 1991 International Conference Industrial Electronics, Control, and Instrumentation, 1991.

[2] E. F. Fichter, A Stewart Platform-Based Manipulator: General Theory and Practical Construction, International Journal of Robotics Reserve 5(2) (1986) 157-182.

[3] J-O. Kim, P. K. Khosla, Dexterity Measures for Design and Control of Manipulators, in: Presented at Proceedings of the IROS '91, IEEE/RSJ International Workshop on Intelligent Robots and Systems, Osaka, Japan, 1991.

[4] J-P. Merlet, A DEsign MethOdology for the Conception of Robot with parallel ArchiTecture, Internal Report, INRIA Sophia-Antipolis, 1996.

[5] F. Hao, J-P. Merlet, Multi-criteria optimal design of parallel manipulators based on interval analysis, Mechanism and Machine Theory 40(2) (2005) 151-171.

[6] J-P. Merlet, Designing a parallel manipulator for a specific workspace, International Journal of Robotics Research 16(4) (1997) 545-556.

[7] K. C. Gupta, B. Roth, Design considerations for manipulator workspace, Journal of Mechanical Design - Transactions of the ASME 104(4) (1982) 704-711.

[8] C. Gosselin, J. Angeles, The optimum kinematic design of a spherical three-degree-of-freedom parallel manipulator, ASME Journal of Mech. Transm. Autom. Des. 111(2) (1989) 202–207.

[9] Q. Xu, Y. Li, GA-based architecture optimization of a 3-PUU parallel manipulator for stiffness performance, in: Presented at Proceedings of the 6th World Congress on Intelligent Control and Automation, 2006.

[10]O. Ma, J. Angeles, Optimum architecture design of platform manipulators, in: Presented at Proceedings of the IEEE International Conference on Robotics and Automation, 1991.

[11]C. Gosselin, J. Angeles, A Global Performance Index for the Kinematic Optimization of Robot Manipulators, Journal of Mechanical Design - Transactions of the ASME 113 (1991) 220-226.

[12]O. Khatib, J. Burdick, Optimization of dynamics in manipulator design: The operational space formulation, The International Journal of Robotics and Automation 2(2) (1987) 90-98.

[13]J. Ryu, J. Cha, Volumetric error analysis and architecture optimization for accuracy of HexaSlide type parallel manipulators, Mechanism and Machine Theory 38 (2003) 227–240.

[14]J. Angeles, The design of isotropic manipulator architectures in the presence of redundancies, The International Journal of Robotics Research 11(3) (1992) 196-201.

[15]C. A. Klein, B. E. Blaho, Dexterity measures for the design and control of kinematically redundant manipulators, The International Journal of Robotics Research 6(2) (1987) 72-83.

[16]R. V. Mayorga, B. Ressa, A. K. C. Wong, A kinematic design optimization of robot manipulators, in: Presented at Proceedings of the IEEE International Conference on Robotics and Automation, 1992.

[17]T. Yoshikawa, Manipulability of robotic mechanisms, The International Journal of Robotics Research 4(2) 1985.

[18]J. K. Salisbury, J. J. Craig, Articulated hands: Force control and kinematic issues, The International Journal of Robotics Research 1(1) (1982) 4-17.

[19]L. W. Tsai, S. Joshi, Kinematics analysis of 3-DOF position mechanisms for use in hybrid kinematic machines, Journal of Mechanical Design – Transactions of the ASME 124(2) (2002) 245–253.

[20]Y. Li, Q. Xu, Kinematic analysis and dynamic control of a 3-PUU parallel manipulator for cardiopulmonary resuscitation, in: Presented at Proceedings of the 12th International Conference on Advanced Robotics, 2005.

[21]D. Zhang, Z. Xu, C. M. Mechefske, F. Xi, Optimum design of parallel kinematic toolheads with genetic algorithms, Robotica 22(1) (2004) 77–84.

[22]R. C. Eberhart, Y. Shi, Comparison between genetic algorithms and particle swarm optimization, in: Presented at Proceedings of the 7th International Conference on Evolutionary Programming VII, 1998.

[23]R. Boudreau, C. M, Gosselin, The synthesis of planar parallel manipulators with a genetic algorithm, ASME Journal of Mechanical Design 121(4) (1999) 533-537.

[24] Schmidt, S. F., & Bjorn, C. (1970). Motion Drive Signals for Piloted Flight Simulators. *Analytical Mechanics Associated, Technical Report Contract NAS2-4869*.

[25] Conrad, B., & Schmidt, S. F. (1971). A Study of Techniques for Calculating Motion Drive Signals for Flight Simulators. *NASA CR-114345*.

[26] Sinacori, J. B. (1973). A practical approach to motion simulation. *Visual and Motion Simulation Conference, AIAA Paper*, Palo Alto, CA (pp. 73-931).

[27] Bowles, R. L., Parrish, R.V., & Dieudonne, J.E. (1975). Coordinated Adaptive Washout for Motion Simulators. *Journal of Aircraft*, *12*(1), 44-50.

[28] Sivan, R., Ish-shalom, J., & Huang, J. K. (1982). An Optimal Control Approach to the Design of Moving Flight Simulators. *IEEE Transactions on Systems, Man and Cybernetics, SMC-12*(6), 818-827.

[29] Ariel, D., Sivan, R. (1984). False Cue Reduction in Moving Flight Simulators. *IEEE Transactions on Systems, Man and Cybernetics, SMC-14*(12), 665-671.

[30] Reid, L. D., & Nahon, M. A. (1986). Flight Simulator Motion-based Drive Algorithm:

Part 3 – Pilot Evaluations. *Technical Report UTIAS Report 319*, Univ. of Toronto, Canada.

[31] Nahon, M. A., & Reid, L. D. (1990). Simulator Motion-Drive Algorithms: A Designer's Perspective. *Journal of Guidance, Control, and Dynamics*, *13*, 356-362.

[32] Reid, L. D., Nahon, M. A., & Kirdeikis, J. (1992). Adaptive Simulator Motion Software with Supervisory Control. *Journal of Guidance, Control, and Dynamics*, *15*(2), 376-383.

[33] Idan, M., & Sahar, David (1996). Robust Controller for a Dynamic Six Degree of Freedom Flight Simulator. *In AIAA Proceeding Of Conference On Flight Simulator Technologies* (pp. 53-60).

[34] Pouliot N. A., Gosselin C. M. & Nahon, M. A. (1998). Motion Simulation Capabilities of Three-Degree-of-Freedom Flight Simulators. *Journal of Aircraft*, *35*(1), 9-17.

[35] Moshe, I., & Nahon, M. A. (1999). Offline Comparison of Classical and Robust Flight Simulator Motion Control. *Journal of Guidance, Control, and Dynamics*, *22*(5), 702-709.

[36] Martin, E. A. (2000). Motion and Force Cueing, Part I: Whole Body Motion. *Flight & Ground Simulation Update*, State University of New York, Binghamton NY (pp. 5-18).

[37] Liao, C-. S., Huang, C-. F. & Chieng, W-.H. (2004). A Novel Washout Filter Design for a Six Degree-of-Freedom Motion Simulator. *JSME International Journal Series C*, *47*(2), 626-636.

[38] Wu, W. & Cardullo, F. M. (1997). Is There an Optimum Cueing Algorithm?. *AIAA Modeling and Simulation Technologies Conference*, New Orleans, LA (pp. 23-29).

[39] Chang, Y-. H., Chieng, W-. H., Liao, C-. S., Jeng, S-. L. (2006). A Novel Master Switching Method for Electronic Cam Control with Special Reference to Multi-axis Coordinated. *Control Engineering Practice, Volume 14*(2), 107-120

[40] Telban, R. J., & Cardullo, F. M. (2005). Motion Cueing Algorithm Development: Human-Centered Linear and Nonlinear Algorithms. *NASA CR-2005-213747*, NASA Langley Research Center, Hampton, VA.

[41] Chong, E. K-. P., & Żak, S. H. (2001). *An Introduction to Optimization (pp. 397~410)*. A Wiley-Interscience Publication, John Wiley & Sons, Inc.

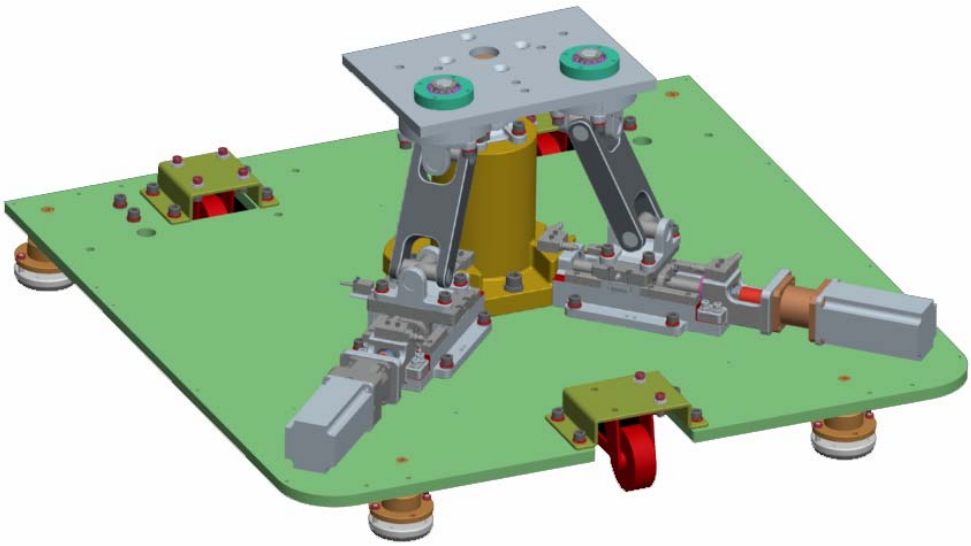

Fig. 1. 2-DOF motion platform, X-2

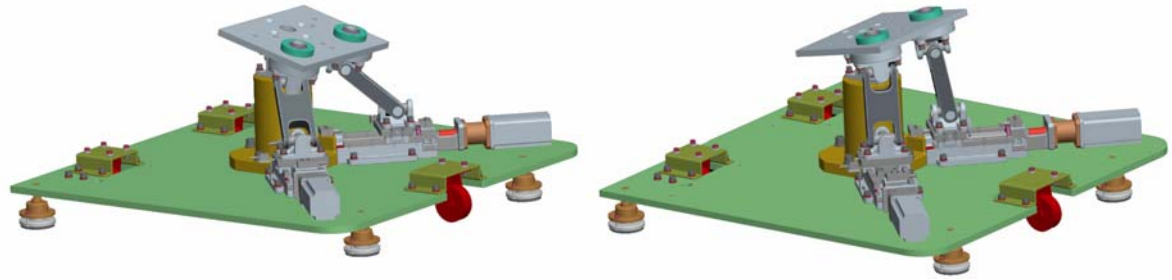

(a)

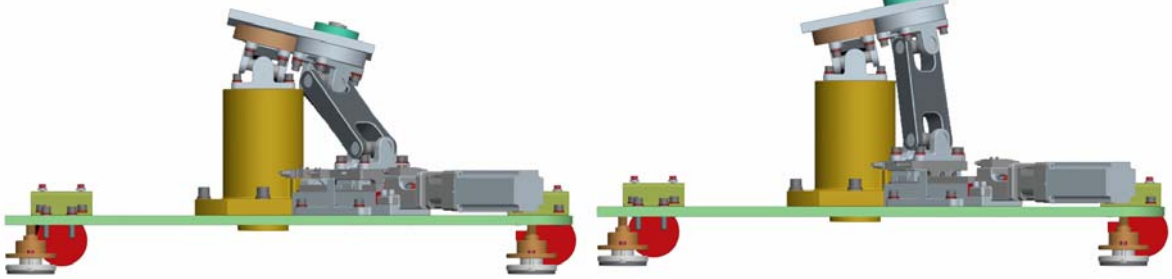

(b)

Fig. 2. Pitch motion of X-2 platforms in the view of (a) 3D view and (b) side view.

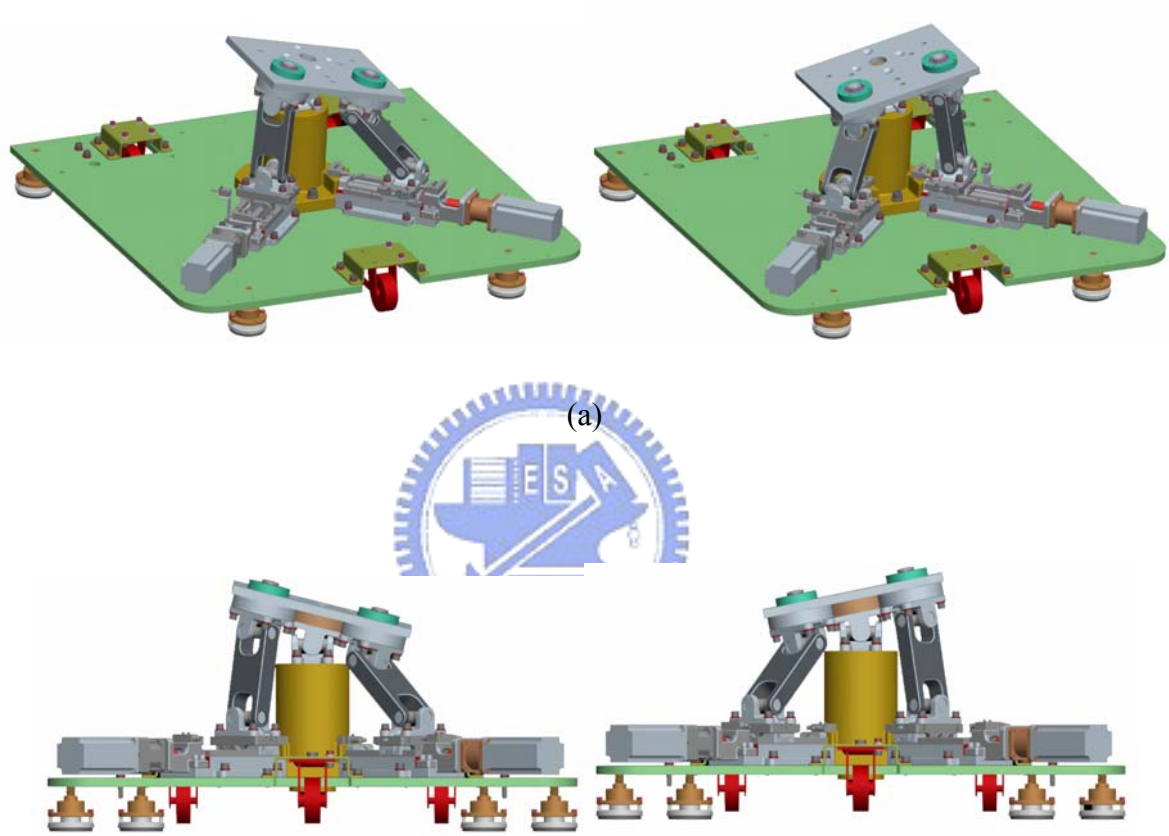

Fig. 3. Roll motion of X-2 platforms in the view of (a) 3D view and (b) side view.

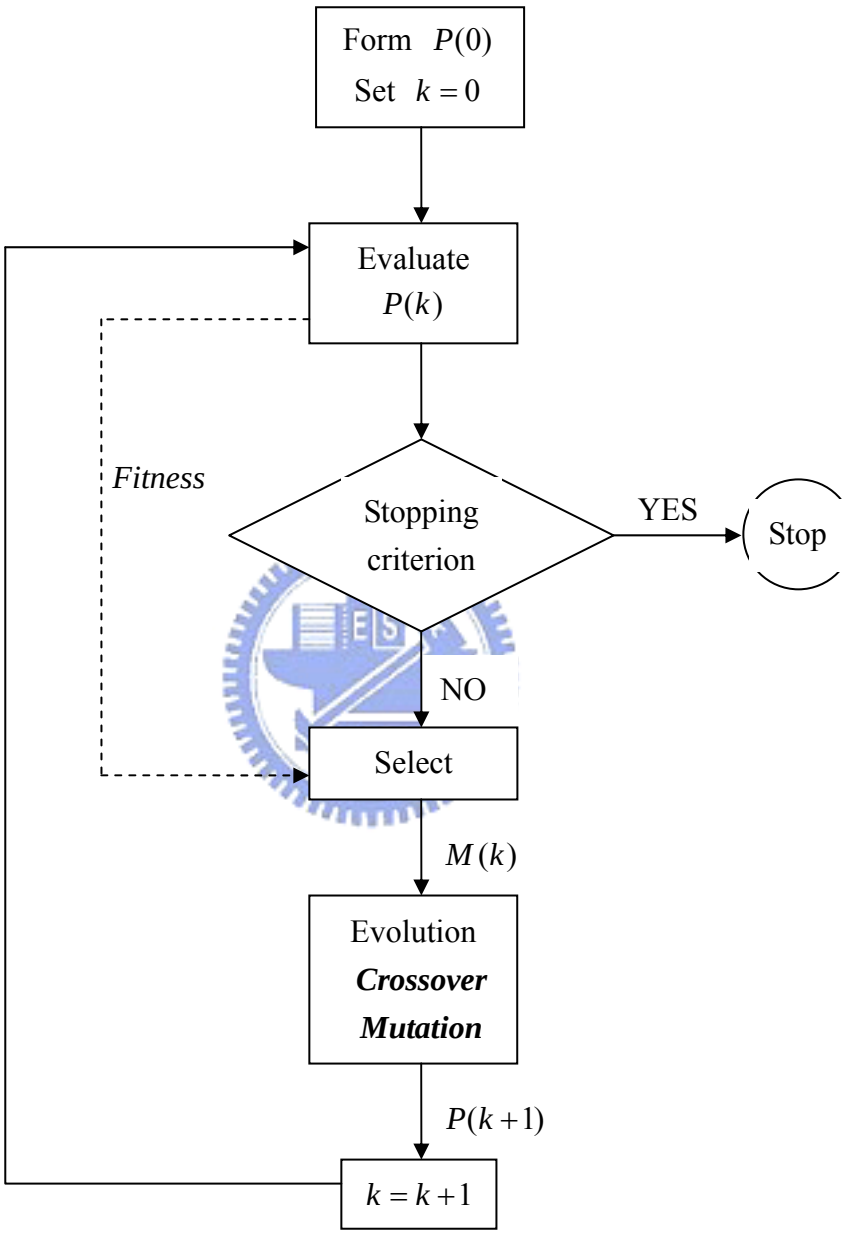

Fig. 4. Flowchart of GA optimization process.

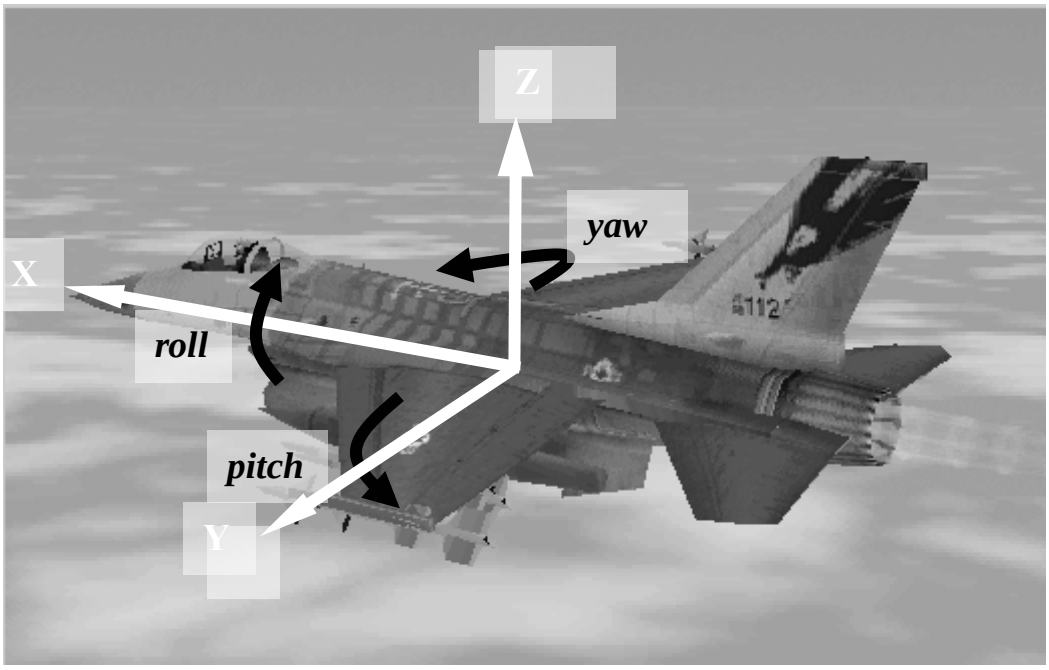

Fig. 5. Coordinates on an aircraft

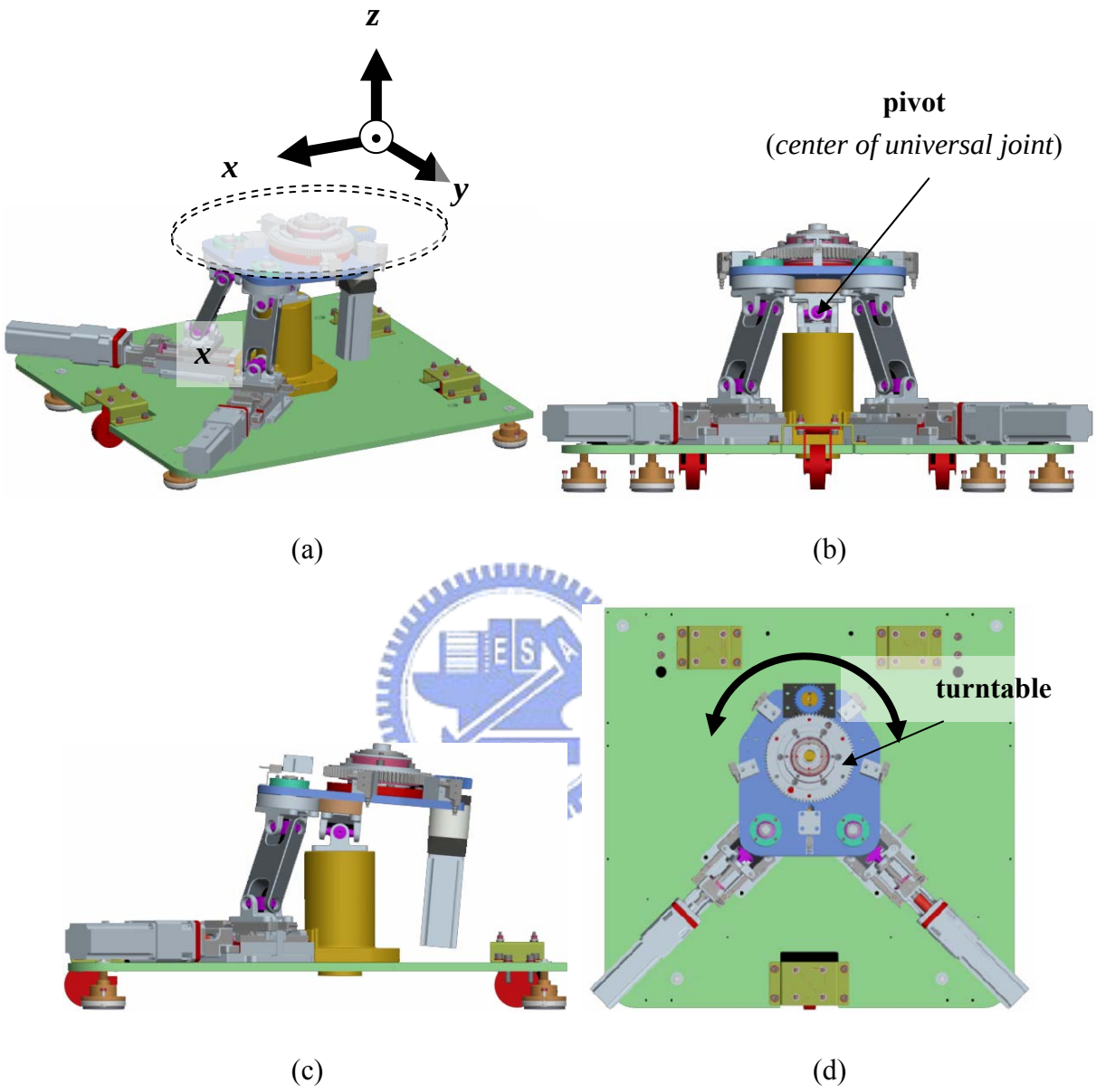

Fig. 6. Motion simulator mechanism with 3-DOF in the view of

(a) 3-D view (b) front view (c) side view (d) top view

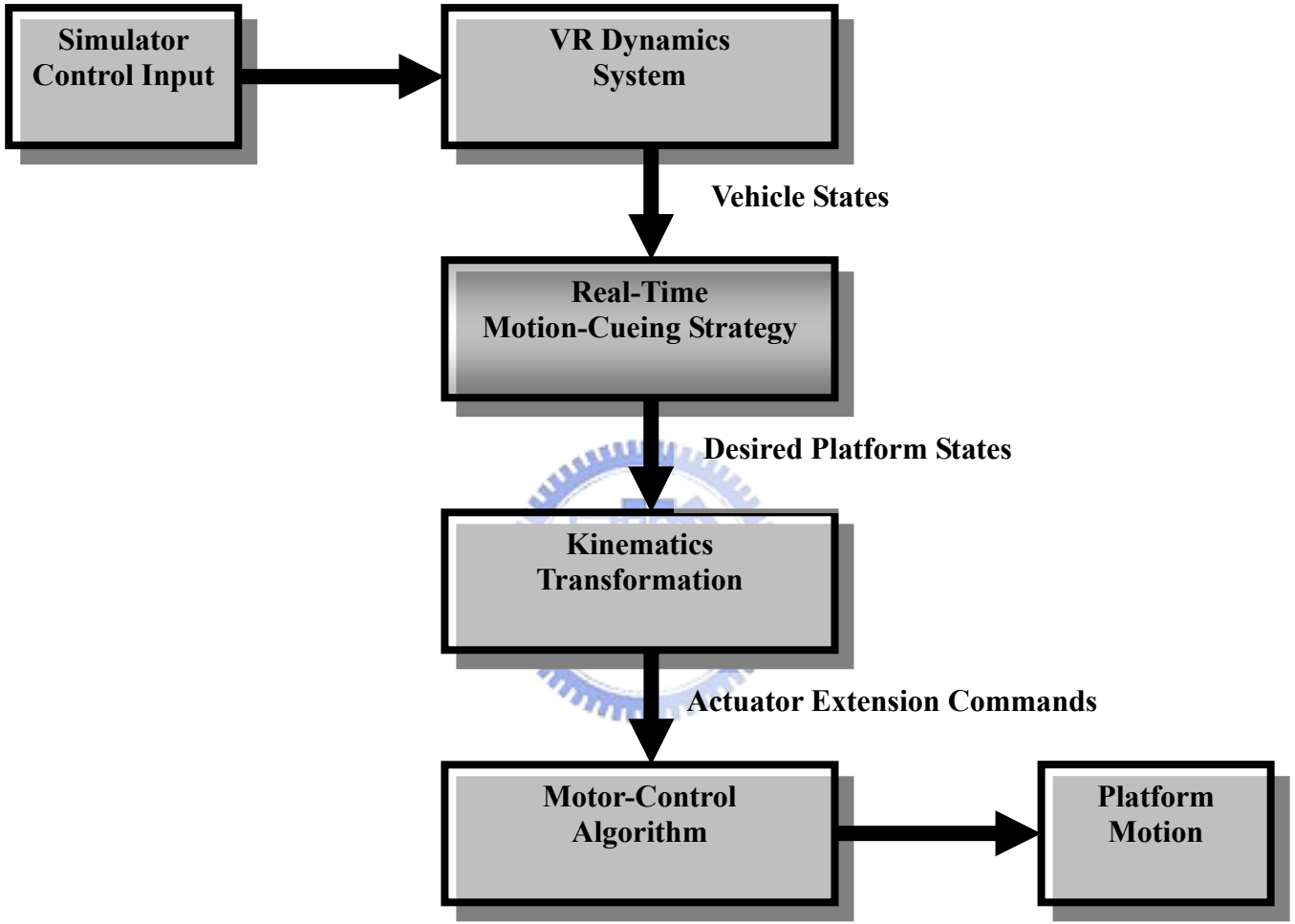

Fig. 7. 3-rotational-DOF motion simulation structure

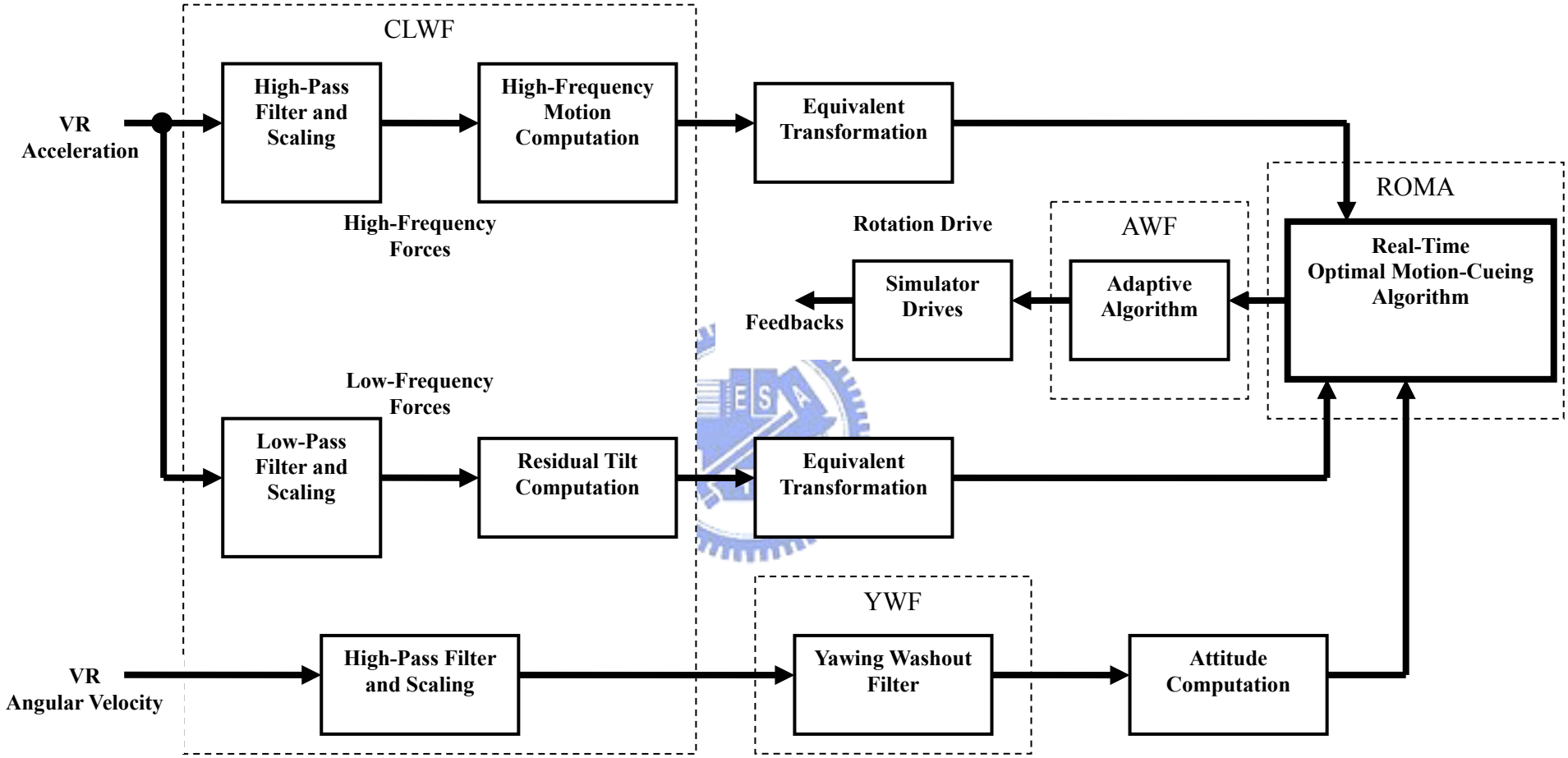

Fig. 8. Simplified schematic of the proposed motion cueing strategy

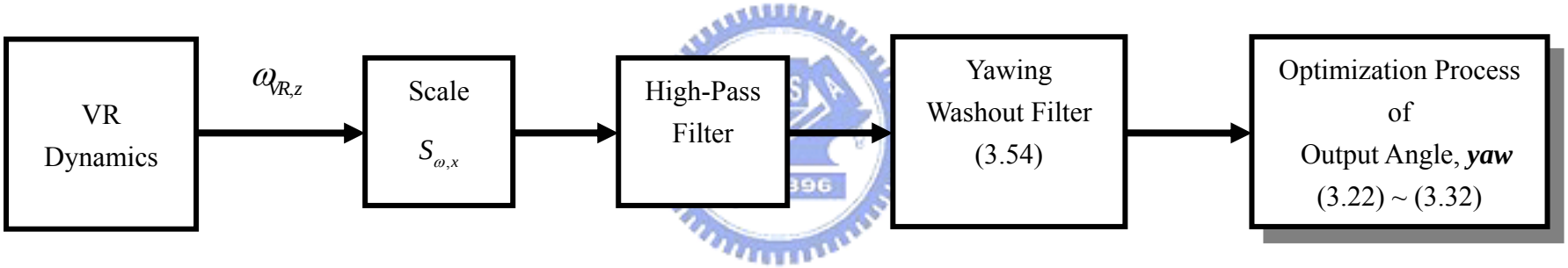

Fig. 9. Block diagram of Optimization process of yaw motion

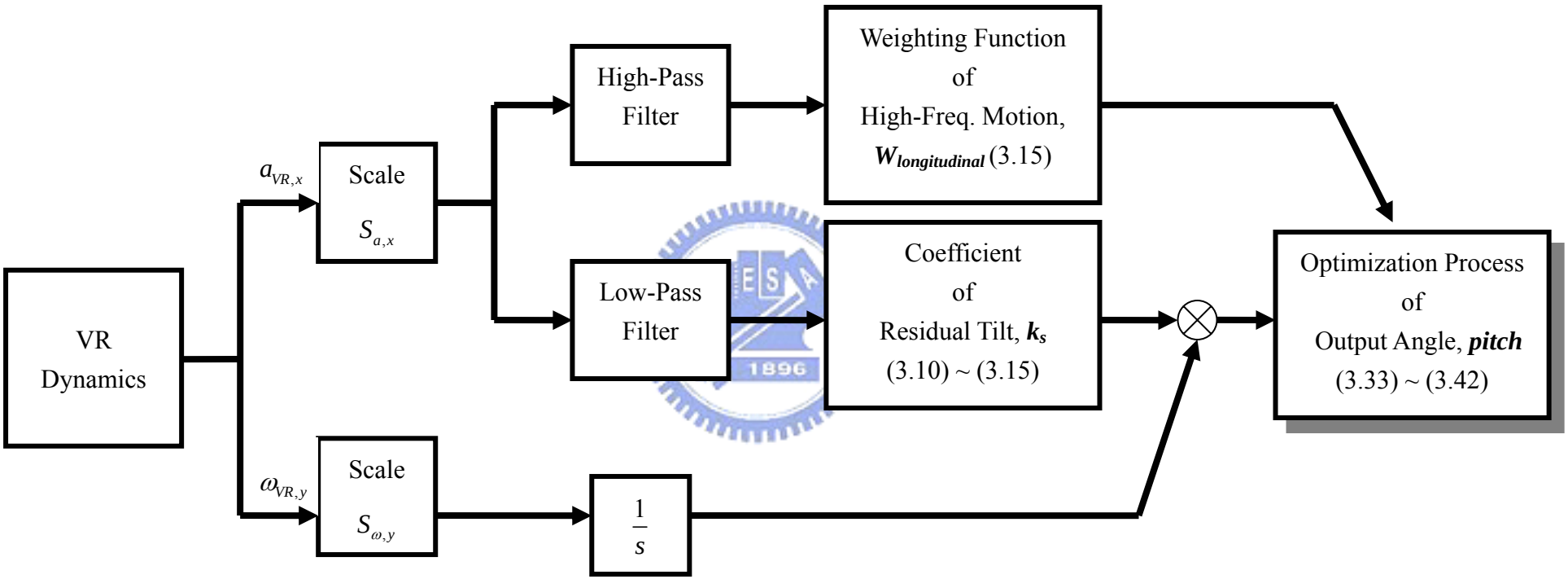

Fig. 10. Block diagram of Optimization process of pitch and surge (longitudinal) motion

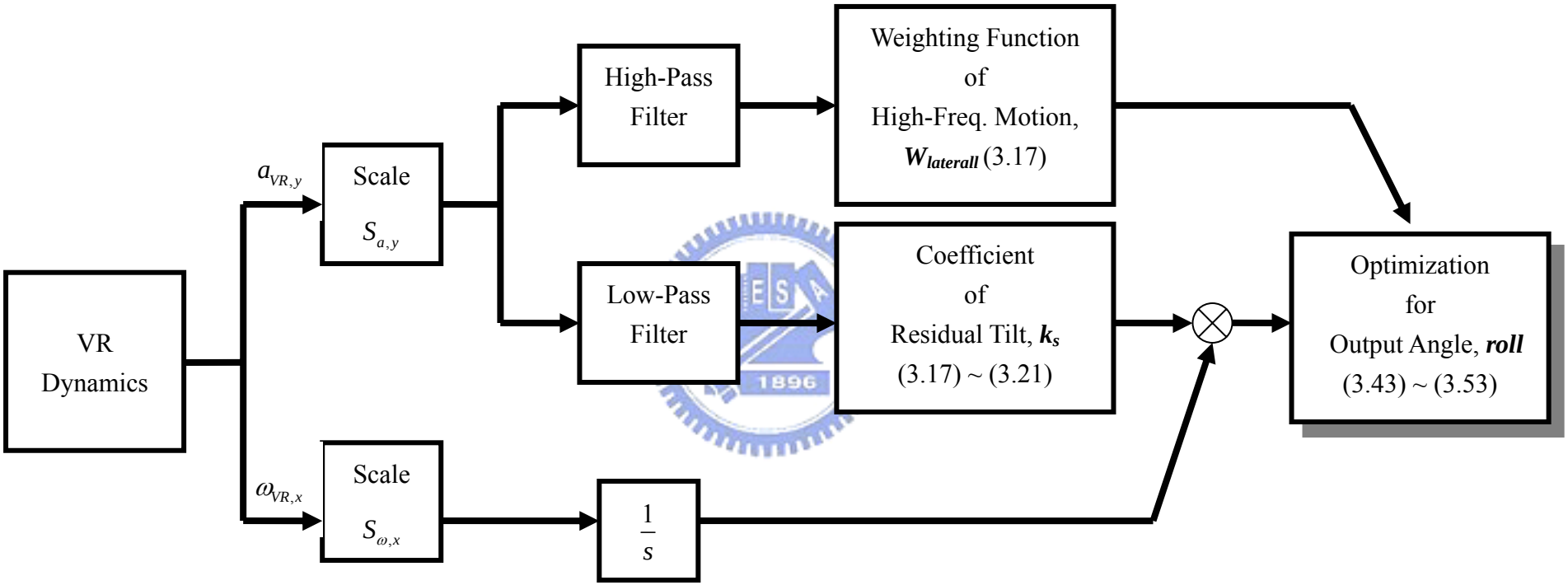

Fig. 11. Block diagram of Optimization process of roll and sway (lateral) motion

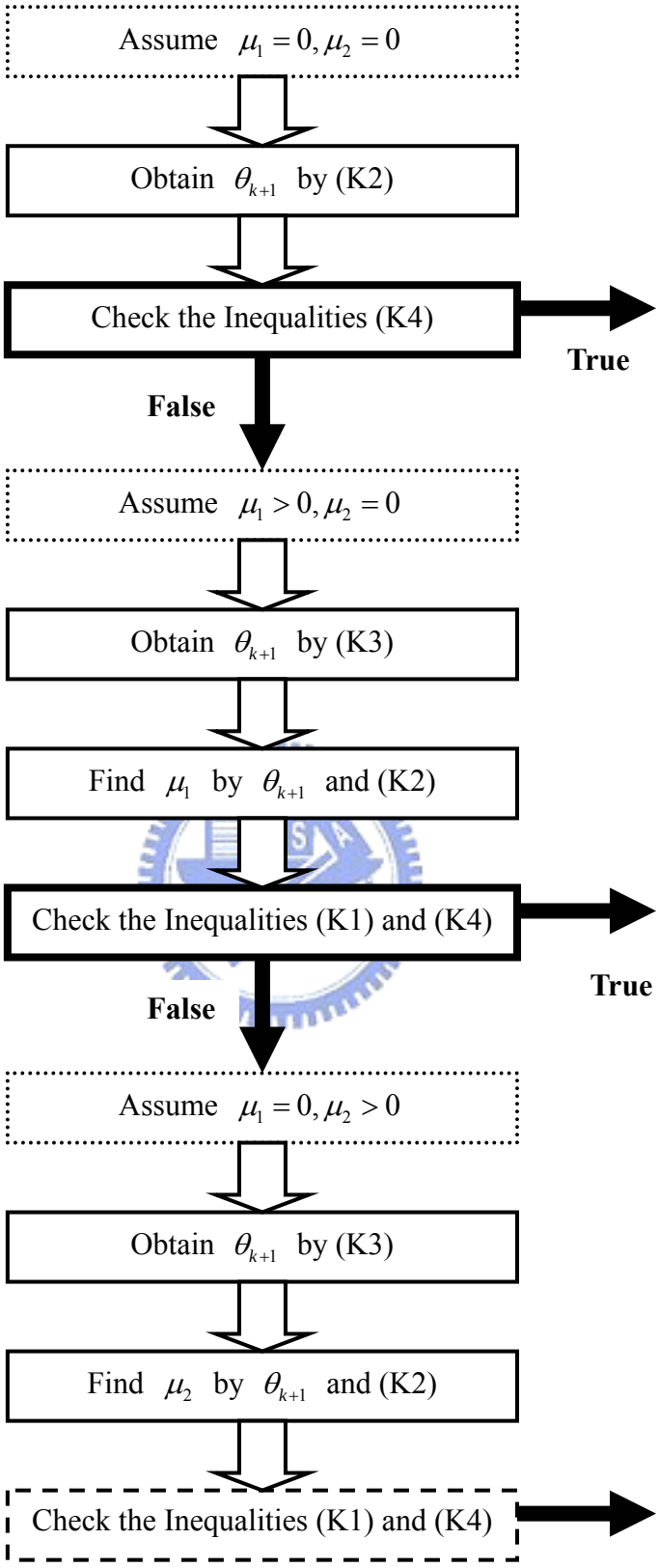

Fig. 12. Procedure of applying KKT conditions in practice

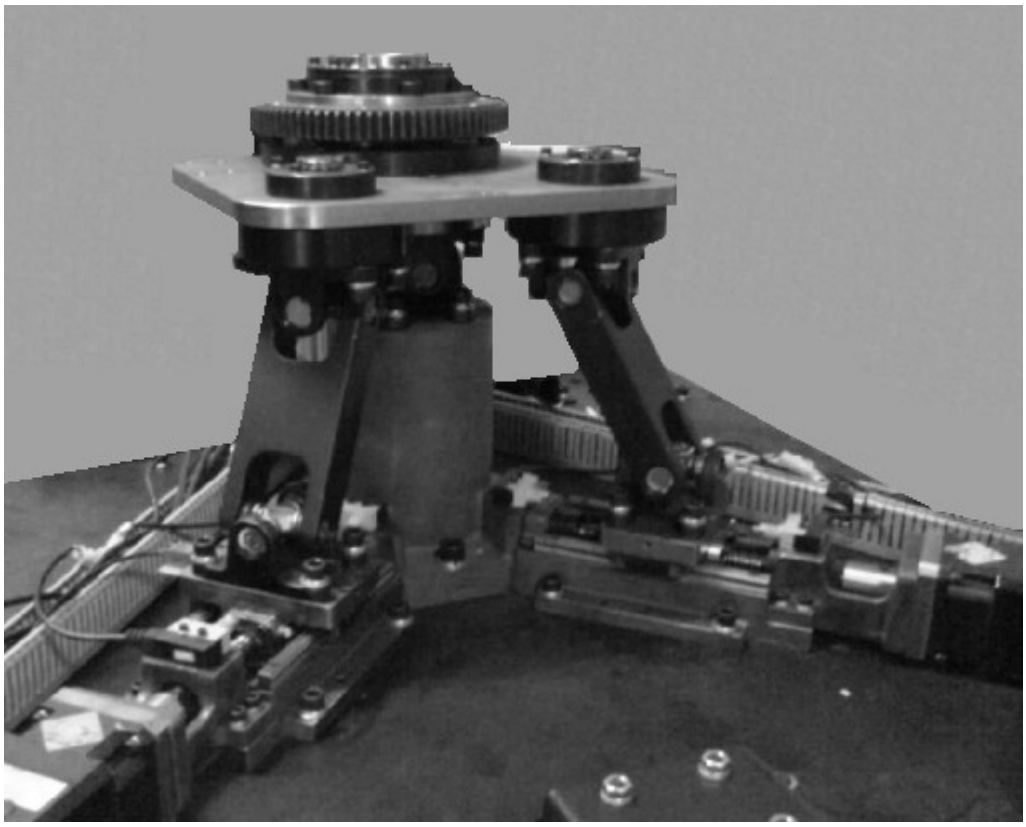

Fig. 13. Experimental X-2 motion platform (Courtesy by IMON Corp.).

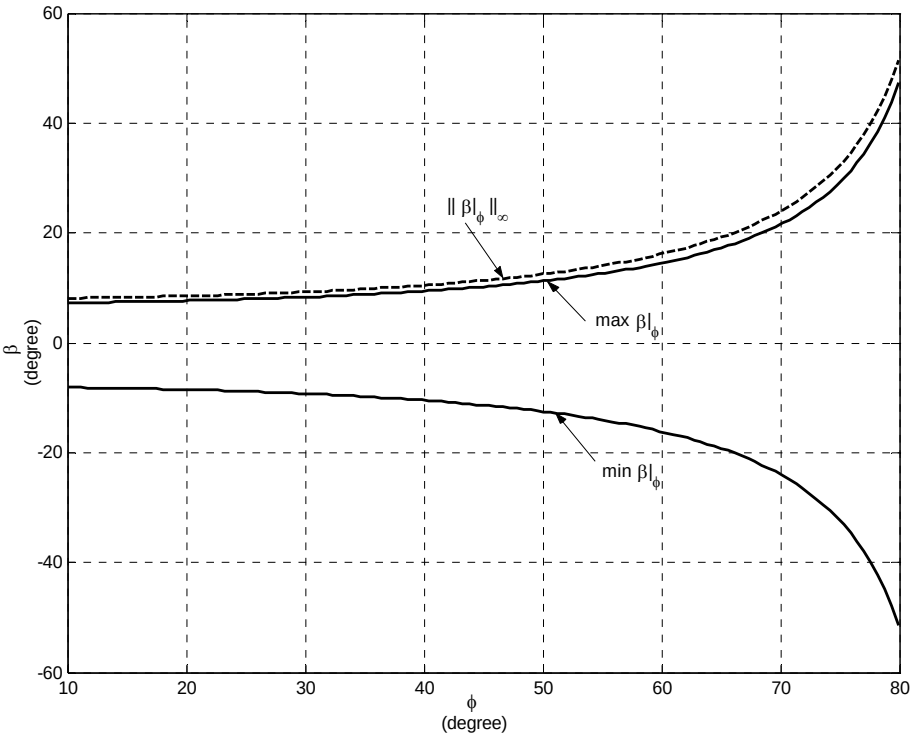

(a)

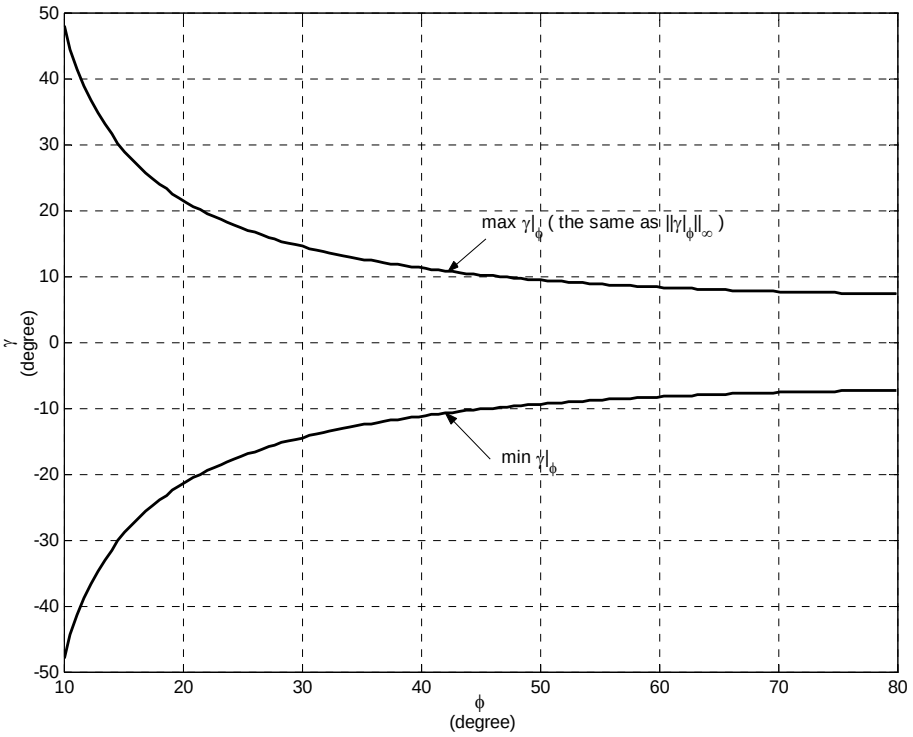

(b)

Fig. 14. Maximum pitch/roll angle along different spread-angle ϕ.

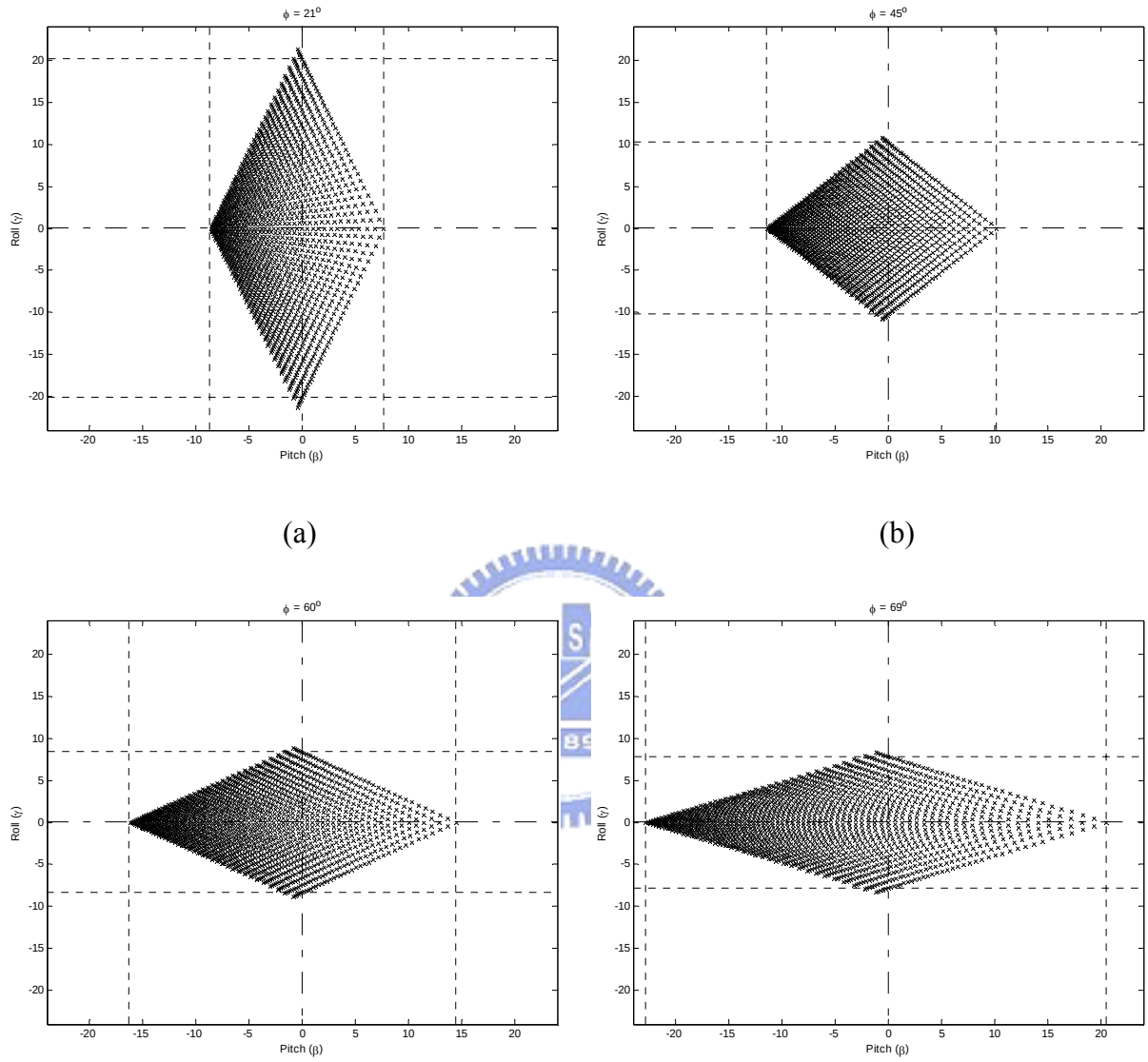

Fig. 15. Comparison of workspaces with (a) ϕ = 21°, (b) ϕ = 45°, (c) ϕ = 60°, and (d) ϕ = 69°.

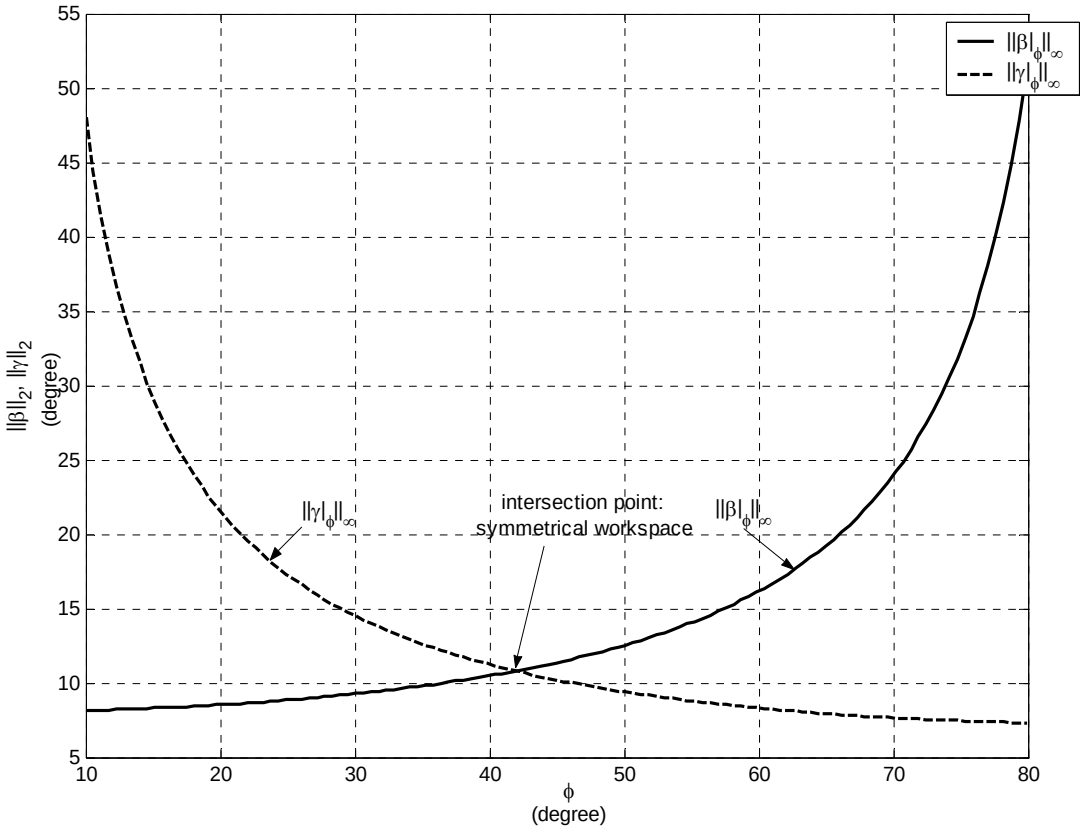

Fig. 16. Workspace symmetry

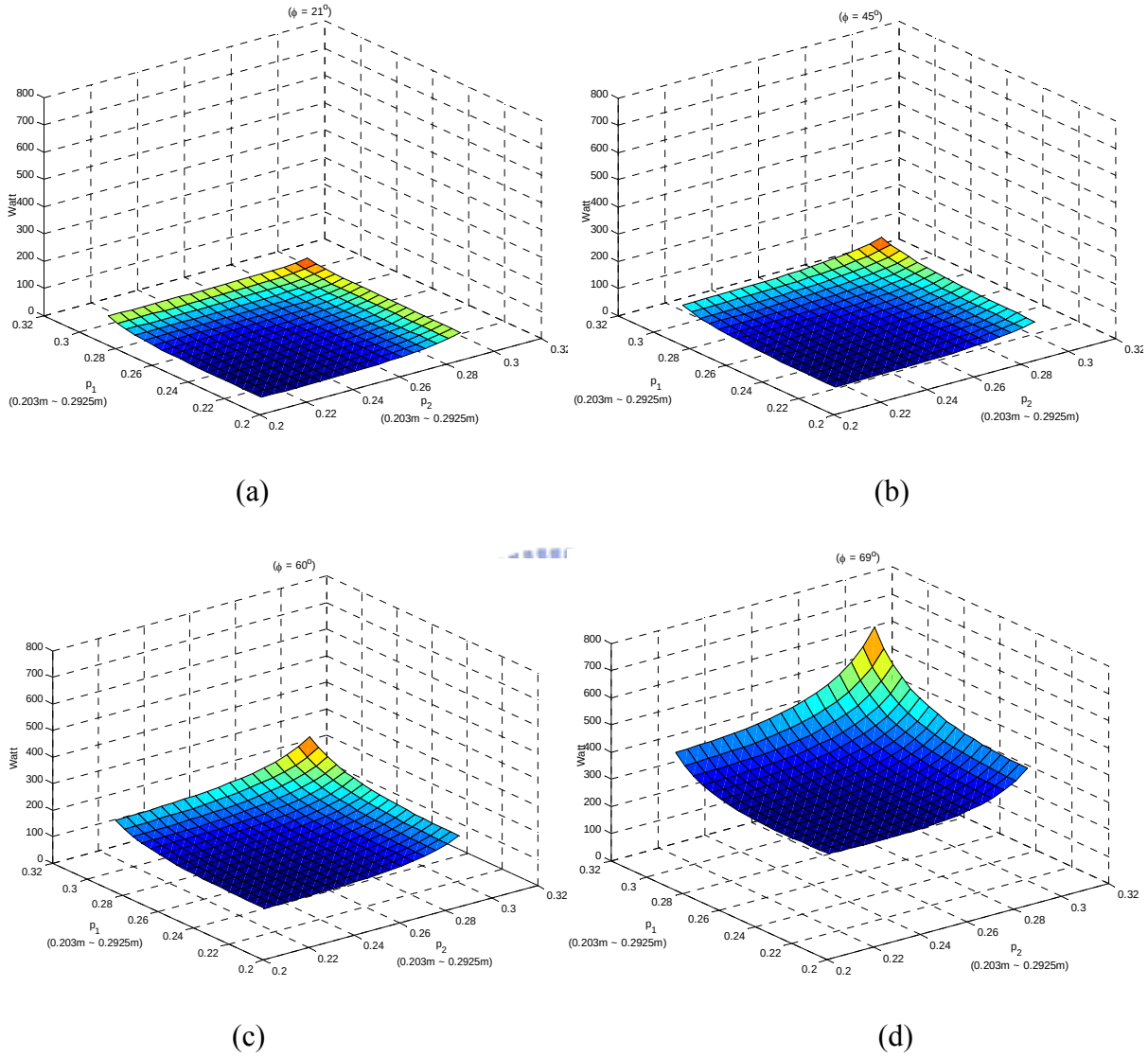

Fig. 17. Comparison of kinetic energy with (a) $\phi = 21°$, (b) $\phi = 45°$, (c) $\phi = 60°$, and (d) $\phi = 69°$.

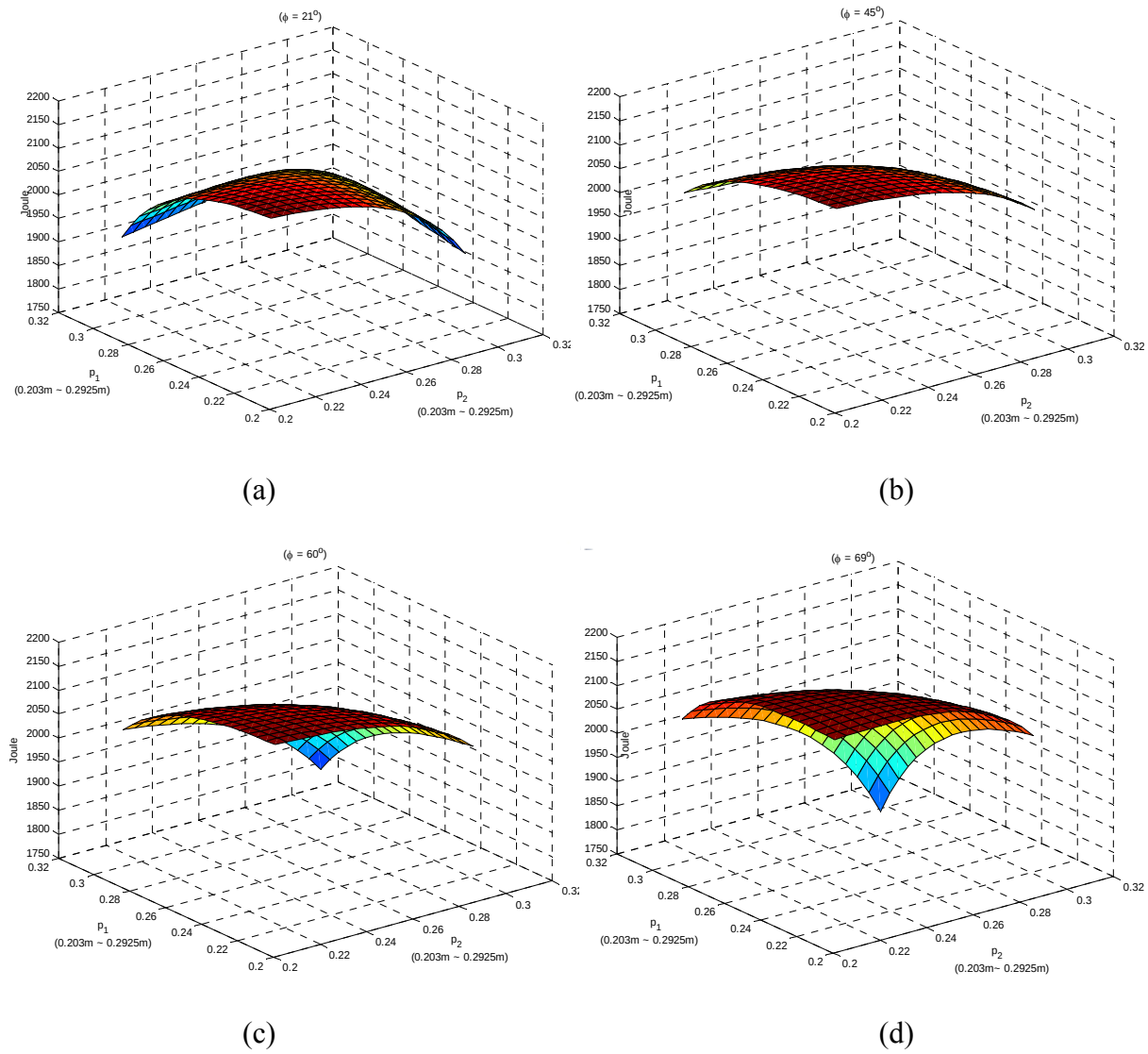

Fig. 18. Comparison of potential energy with (a) ϕ = 21°, (b) ϕ = 45°, (c) ϕ = 60°, and (d) ϕ = 69°.

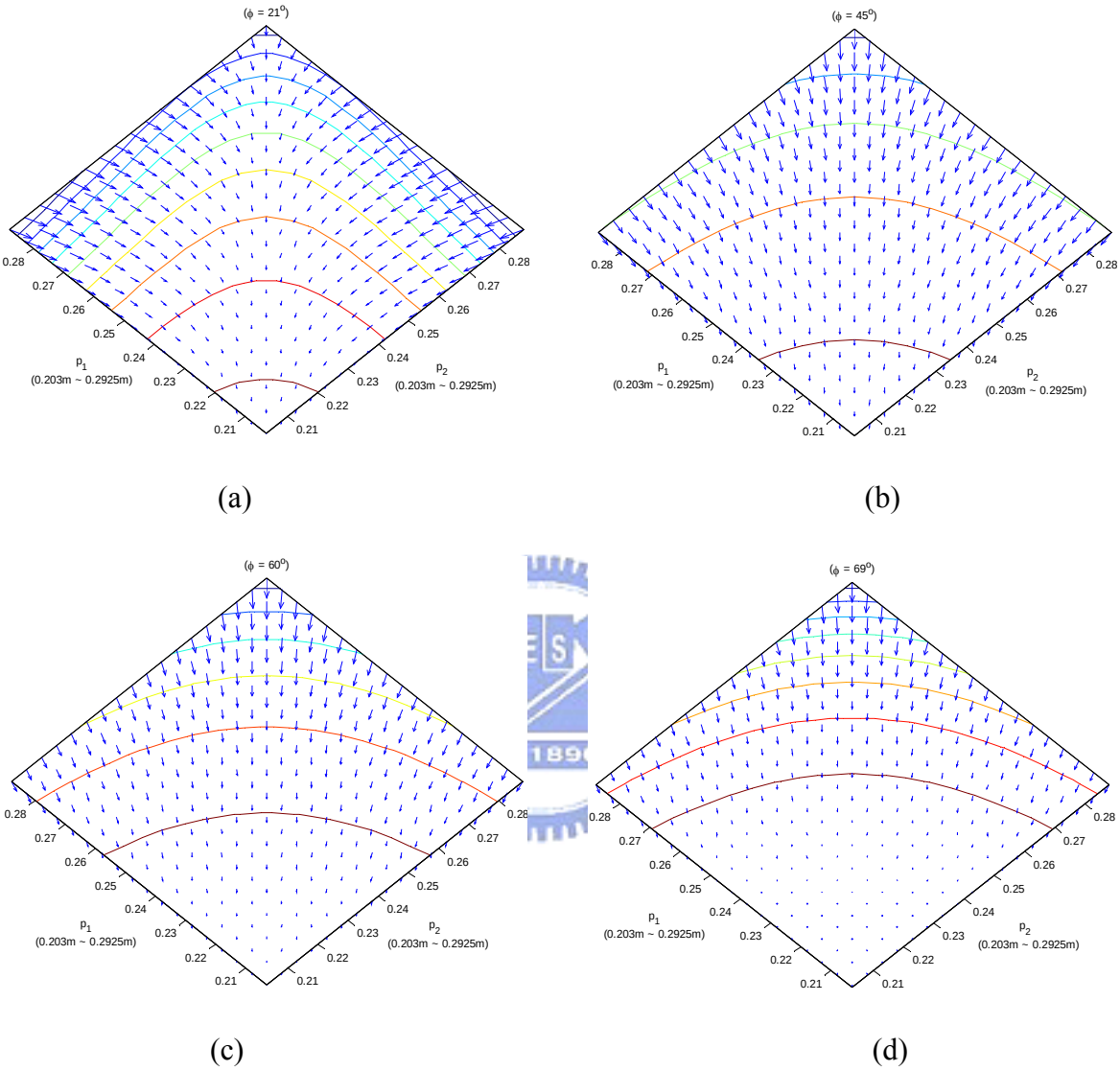

(a) (b)

(c) (d)

Fig. 19. Comparison of gradient of potential energy with (a) $\phi = 21°$, (b) $\phi = 45°$, (c) $\phi = 60°$, and (d) $\phi = 69°$.

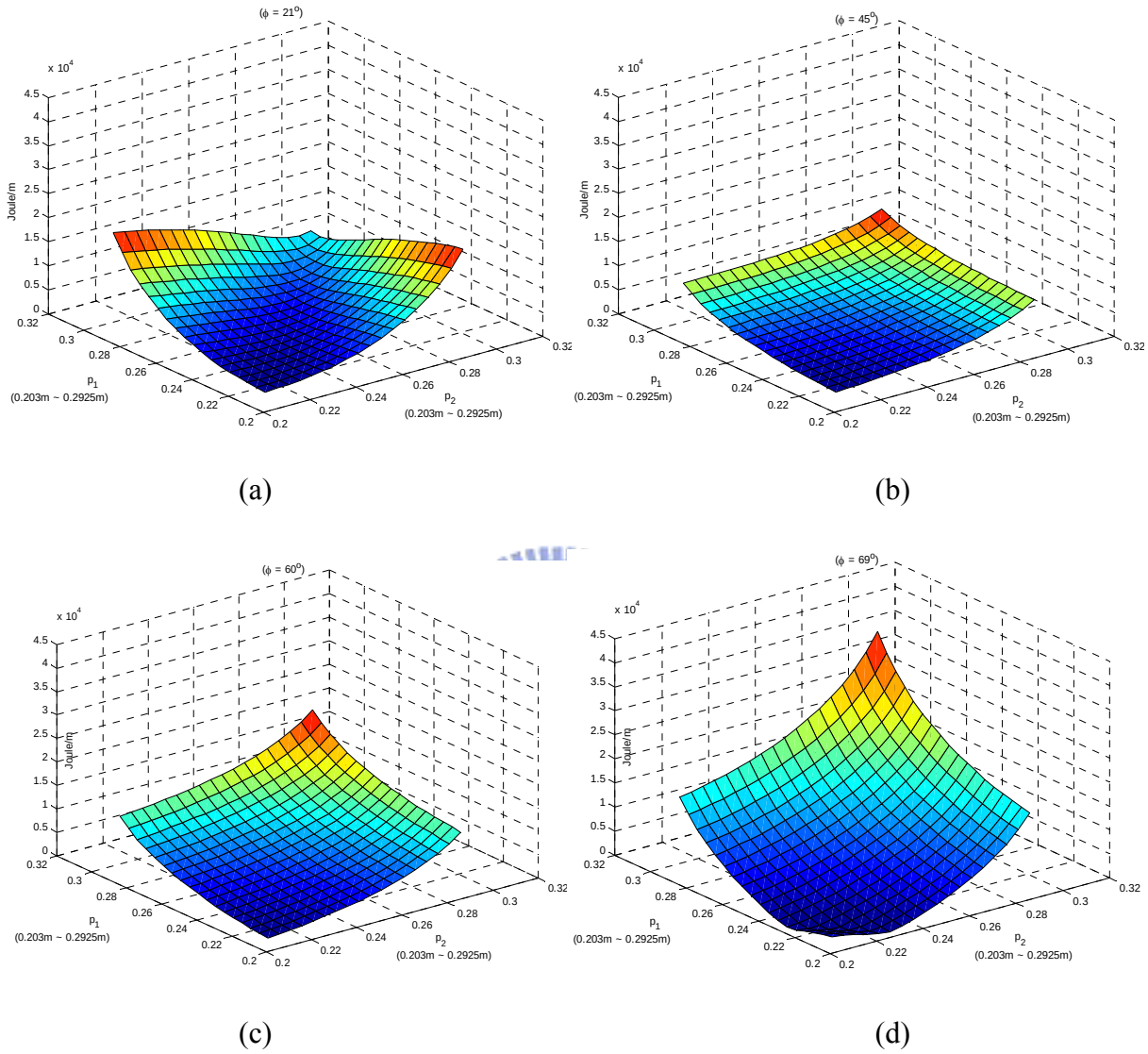

Fig. 20. Comparison of 2-norm of gradient of potential energy with (a) ϕ = 21°, (b) ϕ = 45°, (c) ϕ = 60°, and (d) ϕ = 69°.

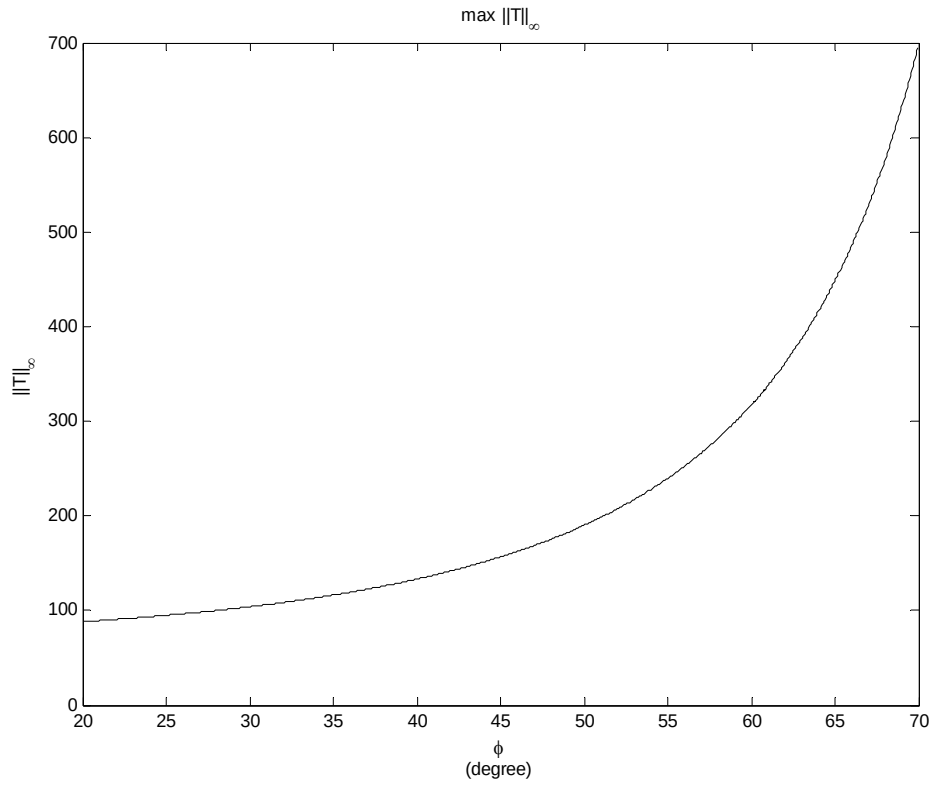

Fig. 21. Infinity-norm of kinetic energy, $\left\| T\big|_{\phi} \right\|_{\infty}$

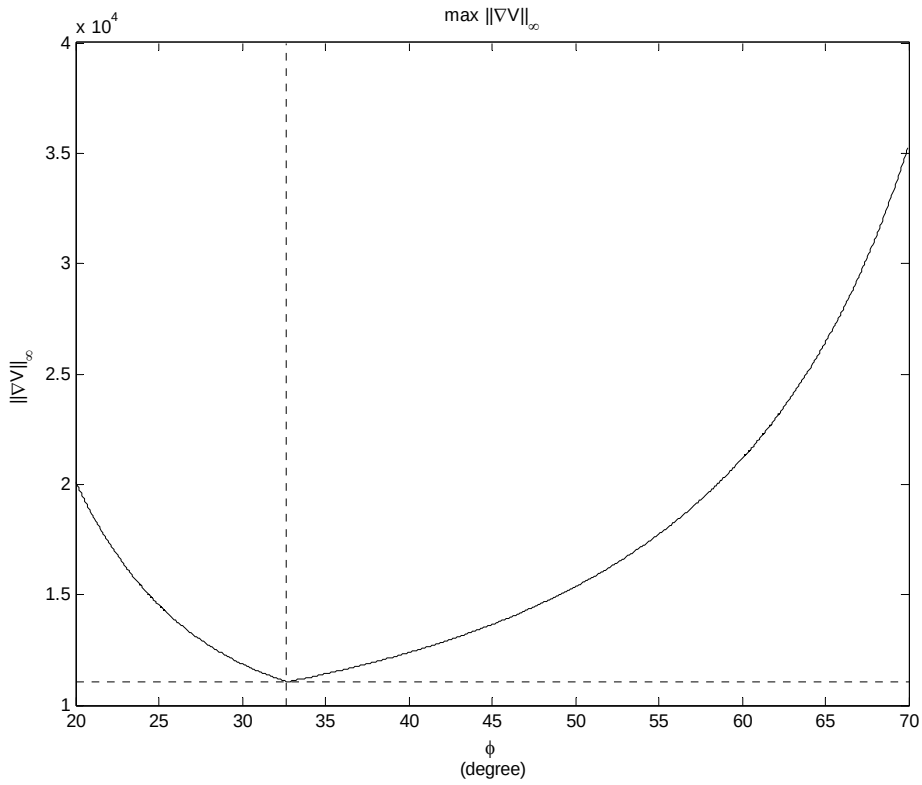

Fig. 22. Infinity-norm of gradient of potential energy, $\left\| \nabla V \big|_{\phi} \right\|_{\infty}$.

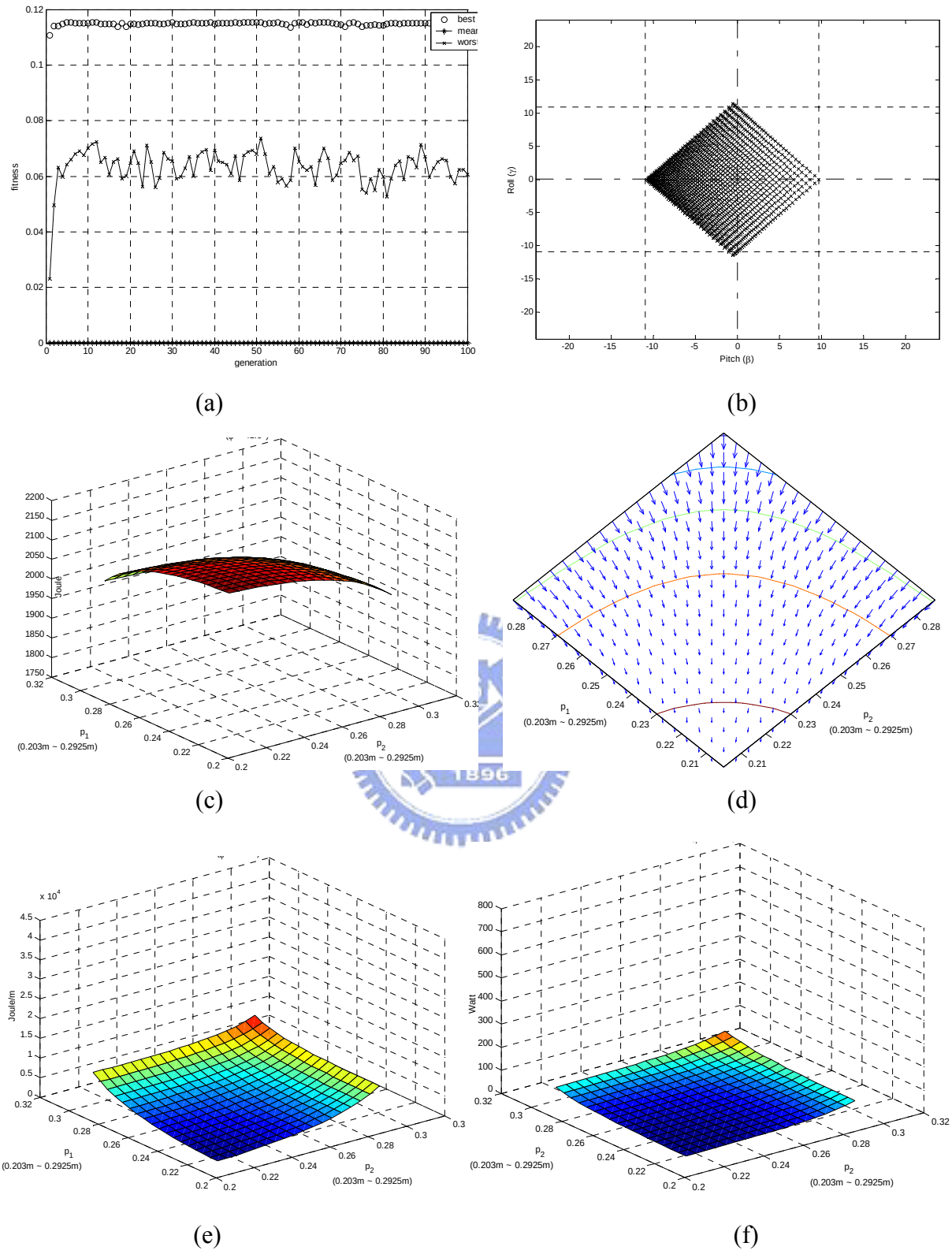

Fig. 23. GA optimization, emphasized the workspace symmetry, with weights $w_b = 80$, $w_T = 10$, $w_V = 10$. This figure shows (a) best-so-far solution during GA recursive searching, (b) workspace, (c) potential energy, (d) gradient of potential energy, (e) norm of gradient of potential energy, and (f) kinetic energy as the optimal solution is $\phi = 41.94°$.

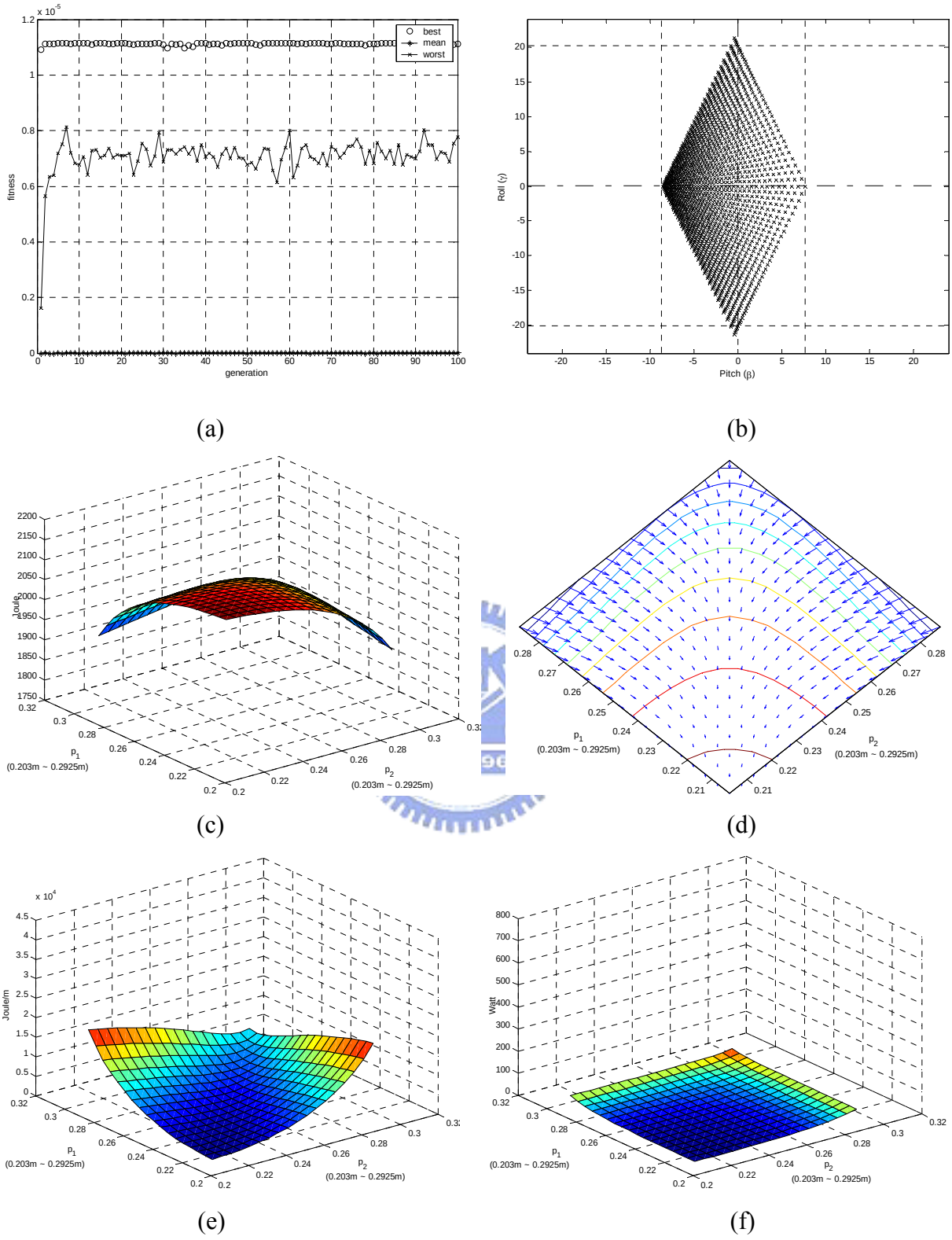

Fig. 24. GA optimization, emphasized the infinity-norm of kinetic energy, with weights $w_b = 10$, $w_T = 80$, $w_V = 10$. This figure shows (a) best-so-far solution during GA recursive searching, (b) workspace, (c) potential energy, (d) gradient of potential energy, (e) norm of gradient of potential energy, and (f) kinetic energy as the optimal solution is $\phi = 21.22°$.

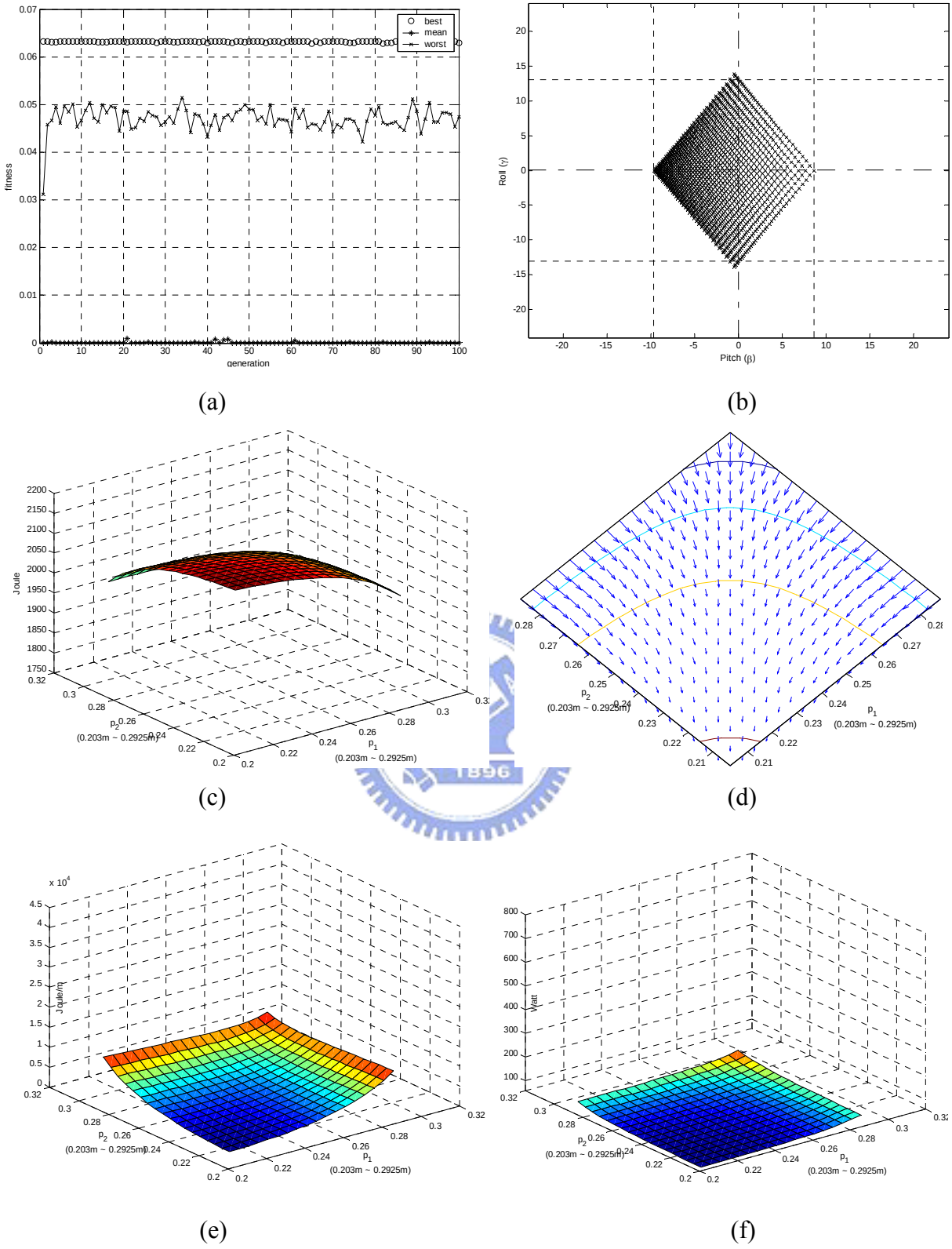

Fig. 25. GA optimization, emphasized the infinity-norm of kinetic energy, with weights $w_b = 10$, $w_T = 10$, $w_V = 80$. This figure shows (a) best-so-far solution during GA recursive searching, (b) workspace, (c) potential energy, (d) gradient of potential energy, (e) norm of gradient of potential energy, and (f) kinetic energy as the optimal solution is $\phi = 33.49°$.

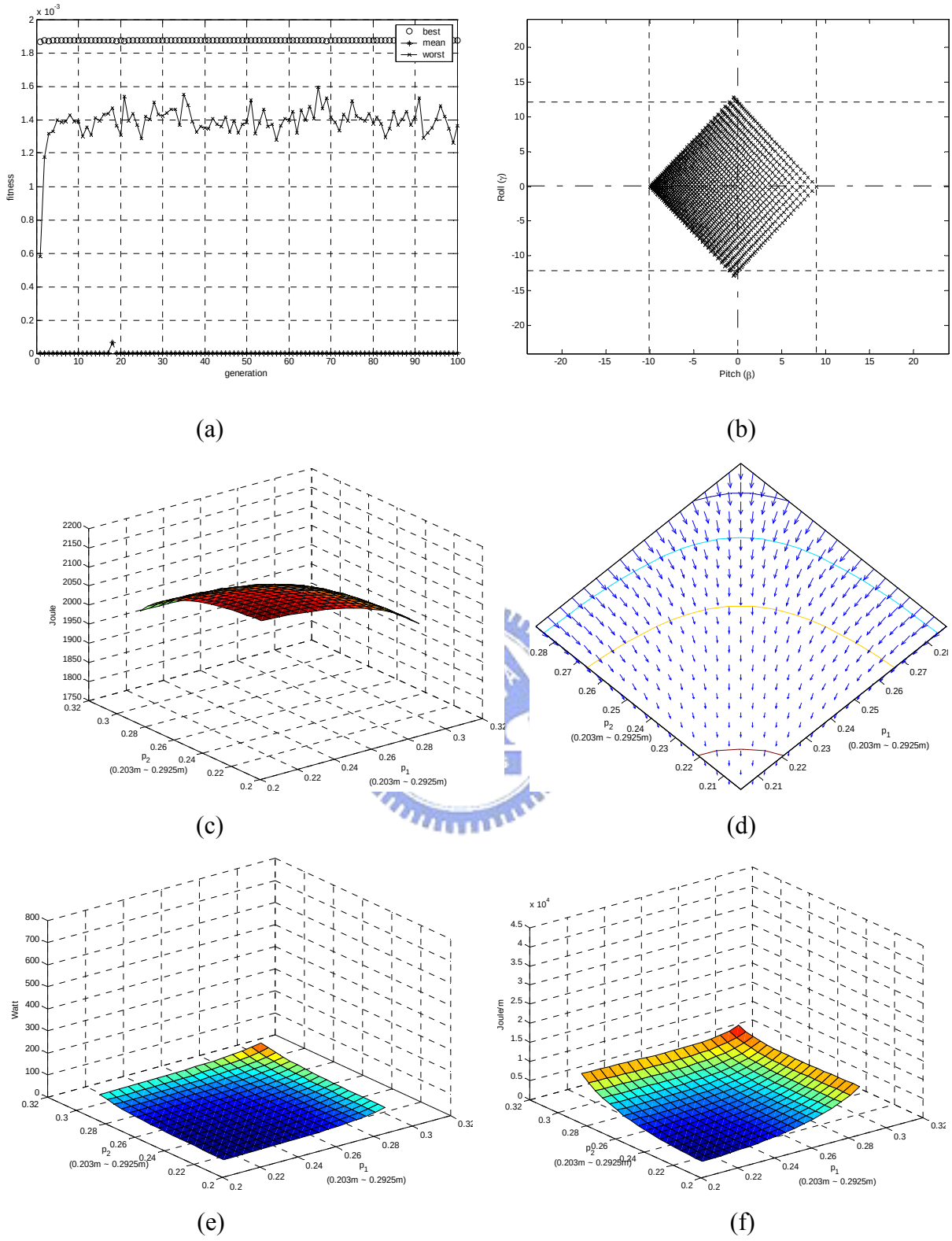

Fig. 26. GA optimization, emphasized the infinity-norm of kinetic energy, with weights $w_b = 40$, $w_T = 30$, $w_V = 30$. This figure shows (a) best-so-far solution during GA recursive searching, (b) workspace, (c) potential energy, (d) gradient of potential energy, (e) norm of gradient of potential energy, and (f) kinetic energy as the optimal solution is $\phi = 36.53°$.

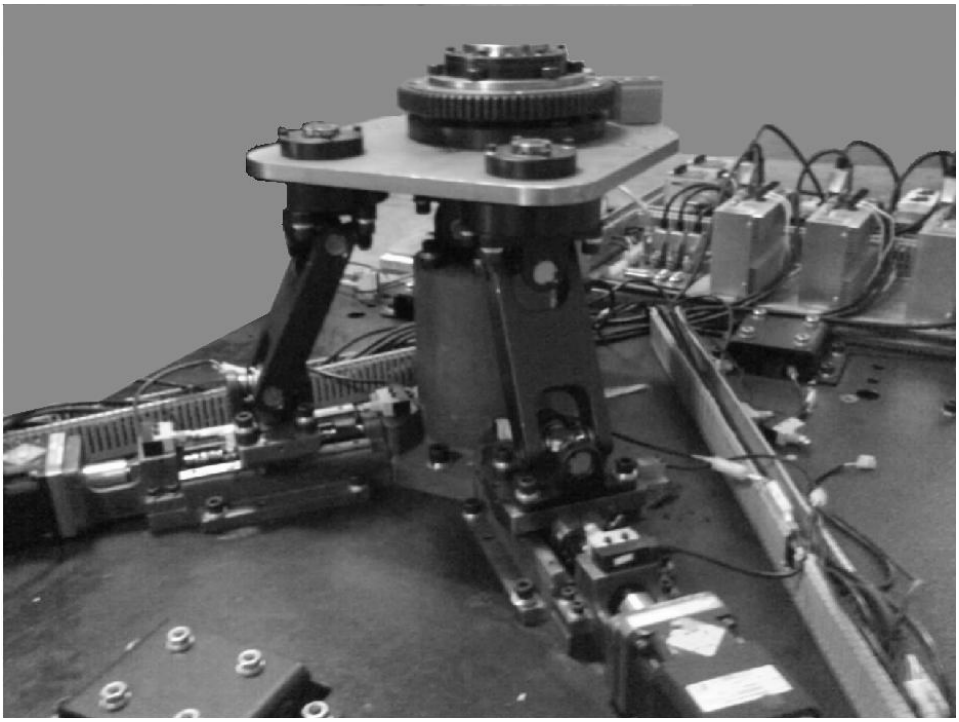

Fig. 27. Implementation of the control and driving system

(X-360, Courtesy of IMON Corp.)

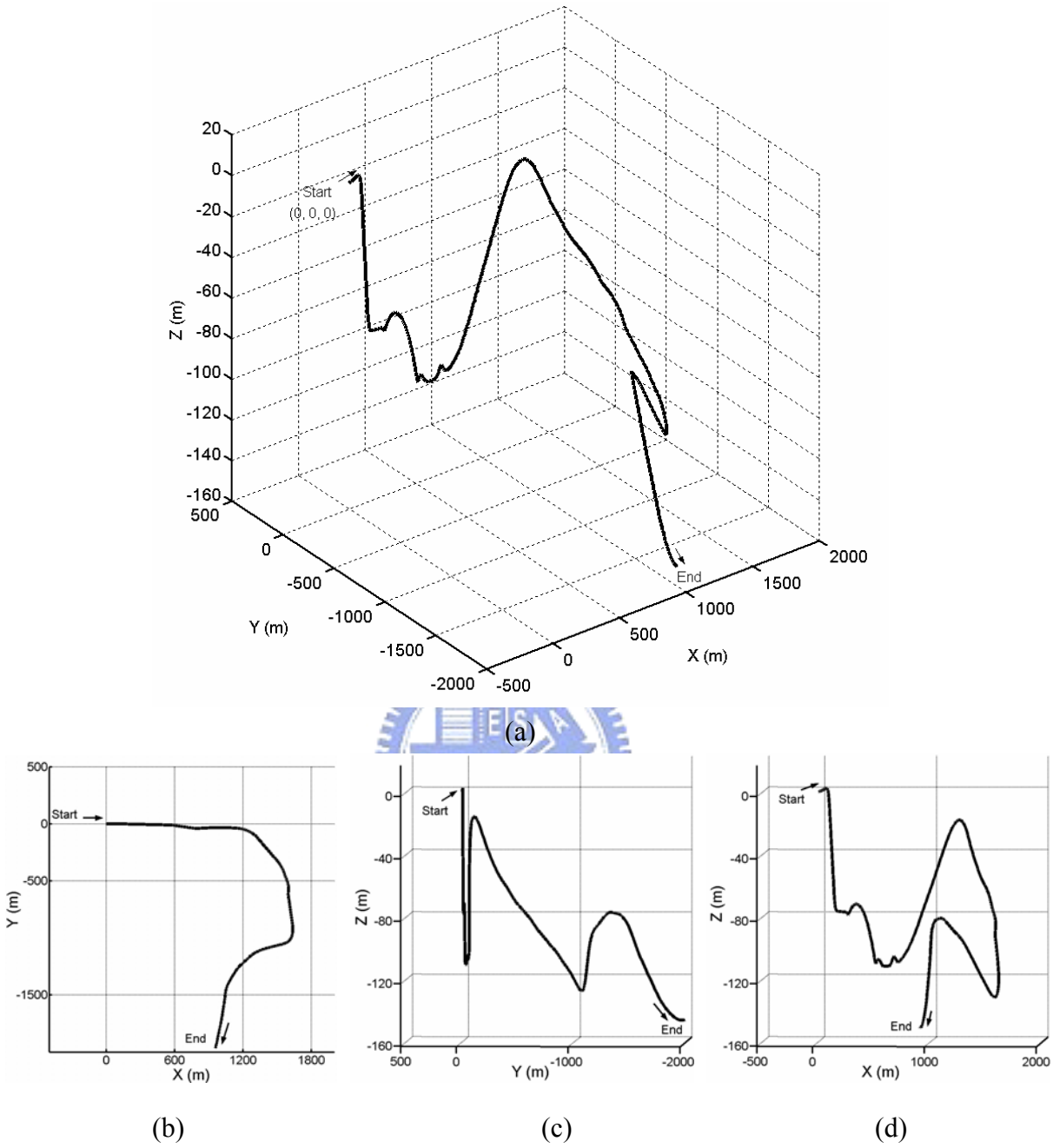

Fig. 28. Trajectory of flight simulation in the view of

(a) 3-D view

(b) Top view (X-Y plane)

(c) Front view (Y-Z plane)

(d) Side view (X-Z plane)

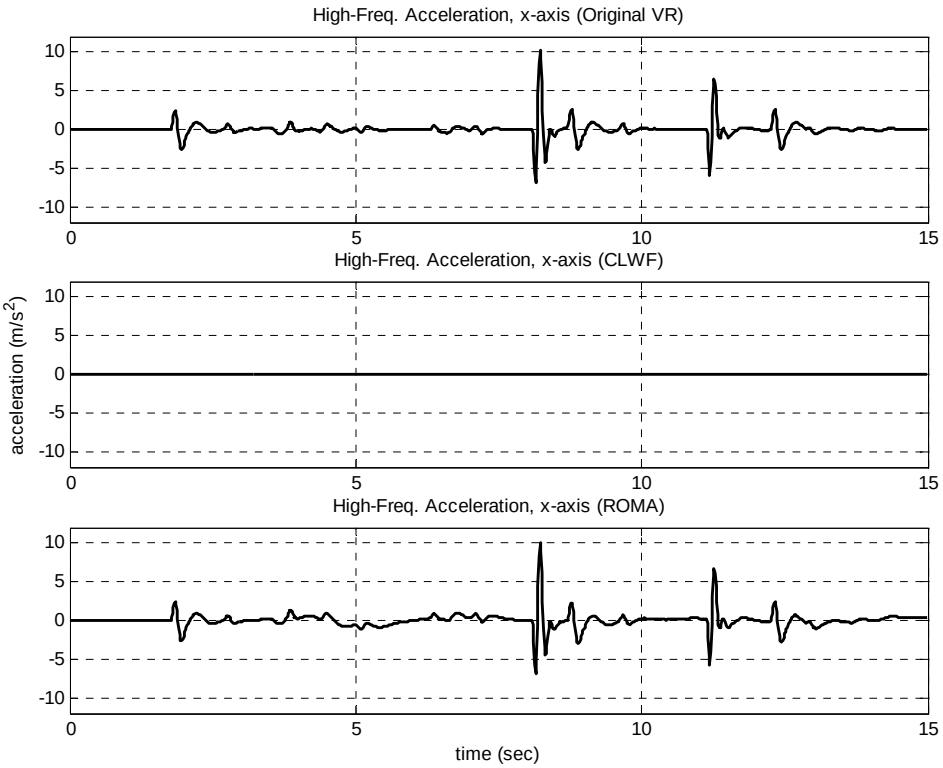

Fig. 29. Comparison of linear high-frequency acceleration along *x*-axis between

(a) original VR dynamic output,

(b) simulator output using classical washout filter (CLWF) and

(c) simulator output using proposed algorithm (ROMA)

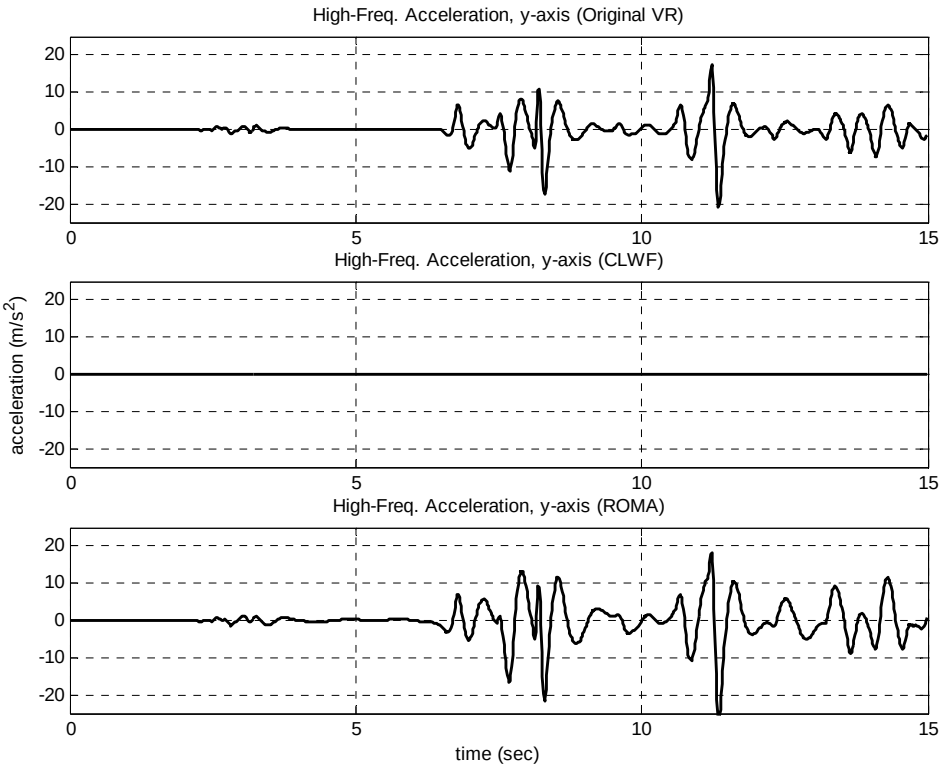

Fig. 30. Comparison of linear high-frequency acceleration along *y*-axis between

(a) original VR dynamic output,

(b) simulator output using classical washout filter (CLWF) and

(c) simulator output using proposed algorithm (ROMA).

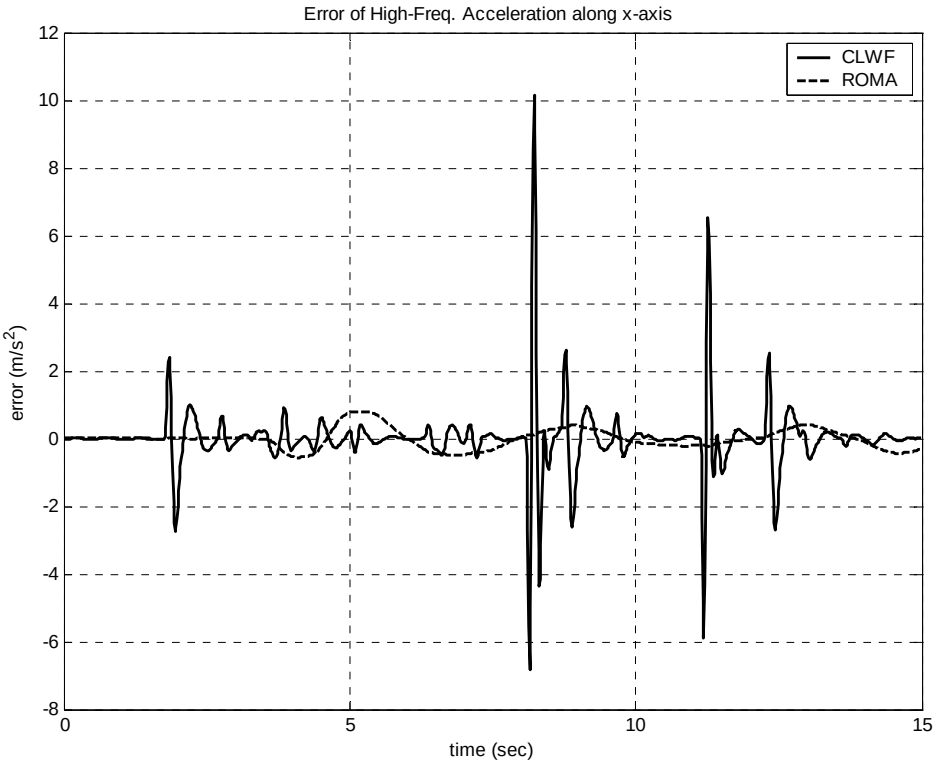

Fig. 31. Segmental error of linear high-frequency (onset) acceleration along *x*-axis using classical method (CLWF) and the proposed algorithm (ROMA)

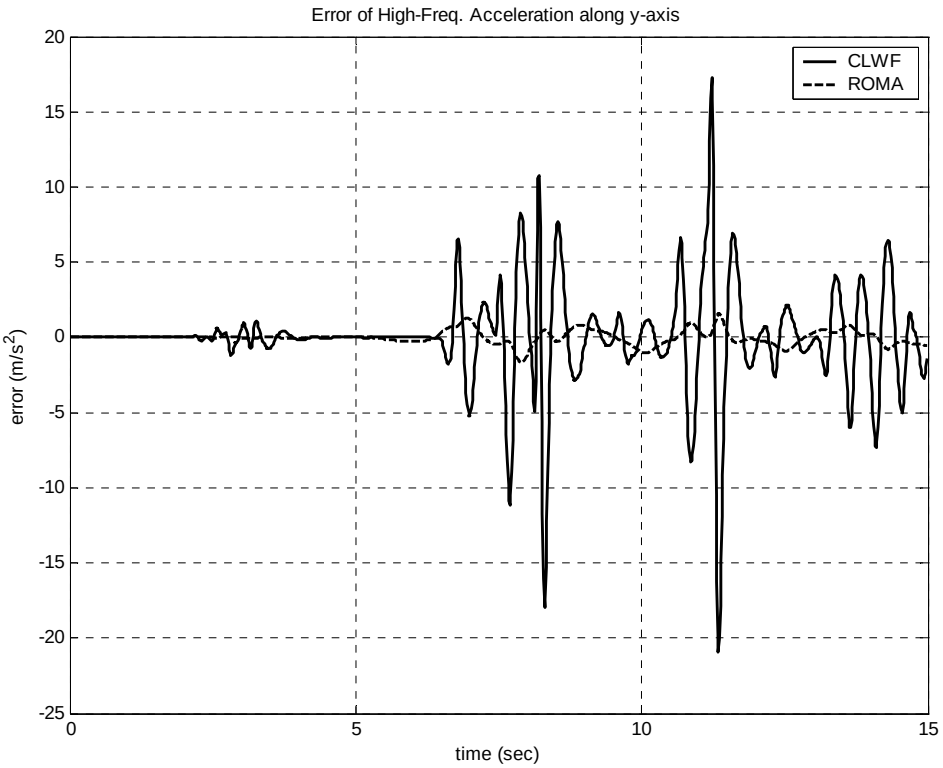

Fig. 32. Segmental error of linear high-frequency (onset) acceleration along *y*-axis using the classical method (CLWF) and the proposed algorithm (ROMA)

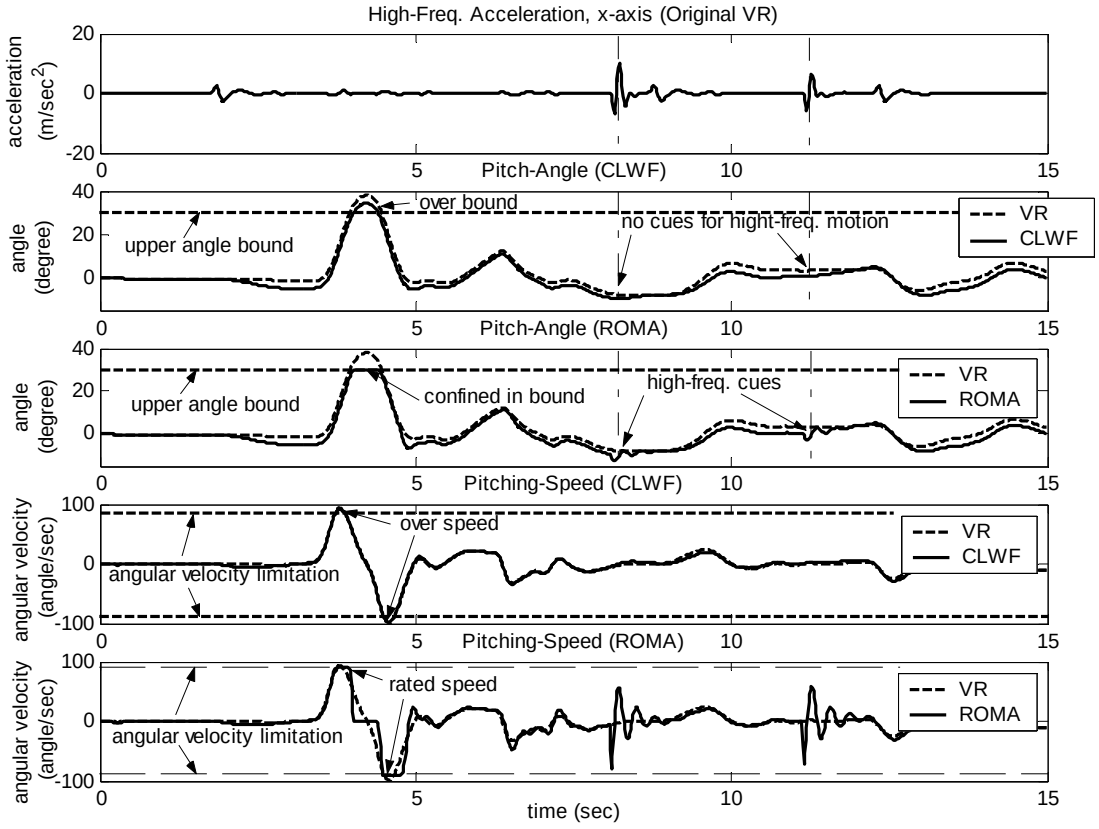

Fig. 33. Comparison of simulator output, longitudinal-motion:

(a) Linear acceleration, *x*-axis (high-frequency)

(b) Pitch-angle, using classical washout filter (CLWF)

(c) Pitch-angle, using proposed algorithm (ROMA)

(d) Pitching-speed, using classical washout filter (CLWF)

(e) Pitching-speed, using proposed algorithm (ROMA)

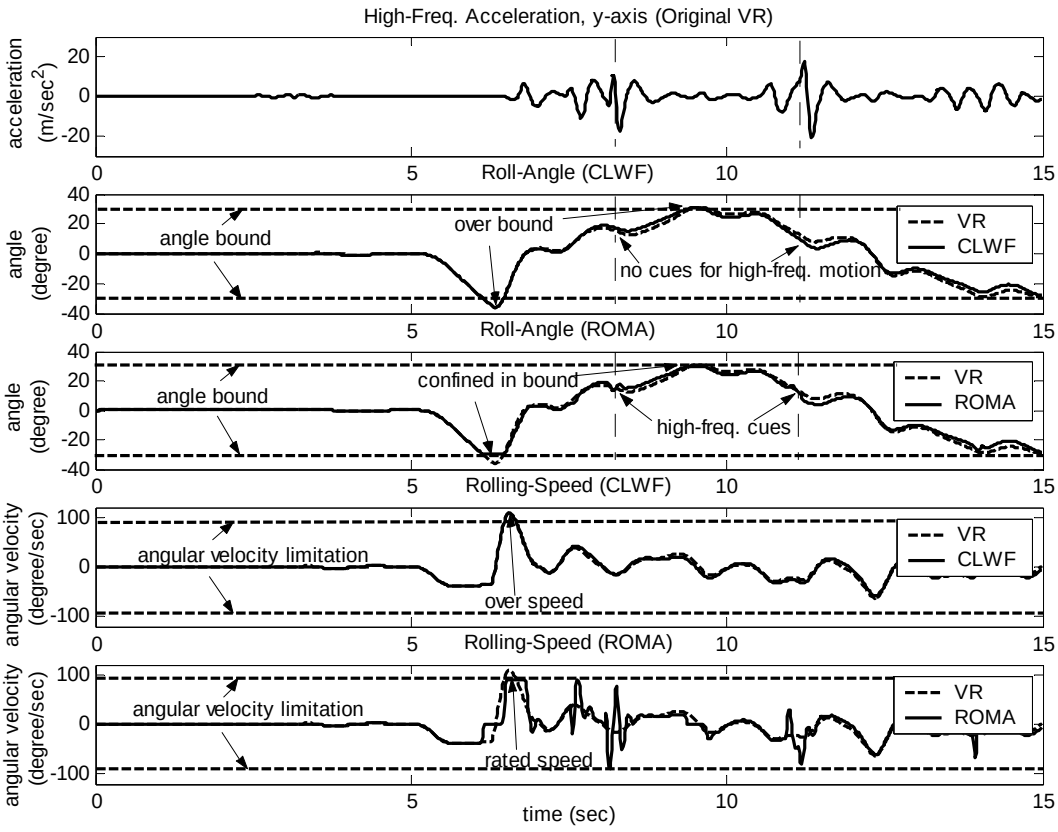

Fig. 34. Comparison of simulator output, lateral-motion:

(a) Linear acceleration, *y*-axis (high-frequency)

(b) Roll-angle, using classical washout filter (CLWF)

(c) Roll-angle, using proposed algorithm (ROMA)

(d) Rolling-speed, using classical washout filter (CLWF)

(e) Rolling-speed, using proposed algorithm (ROMA)

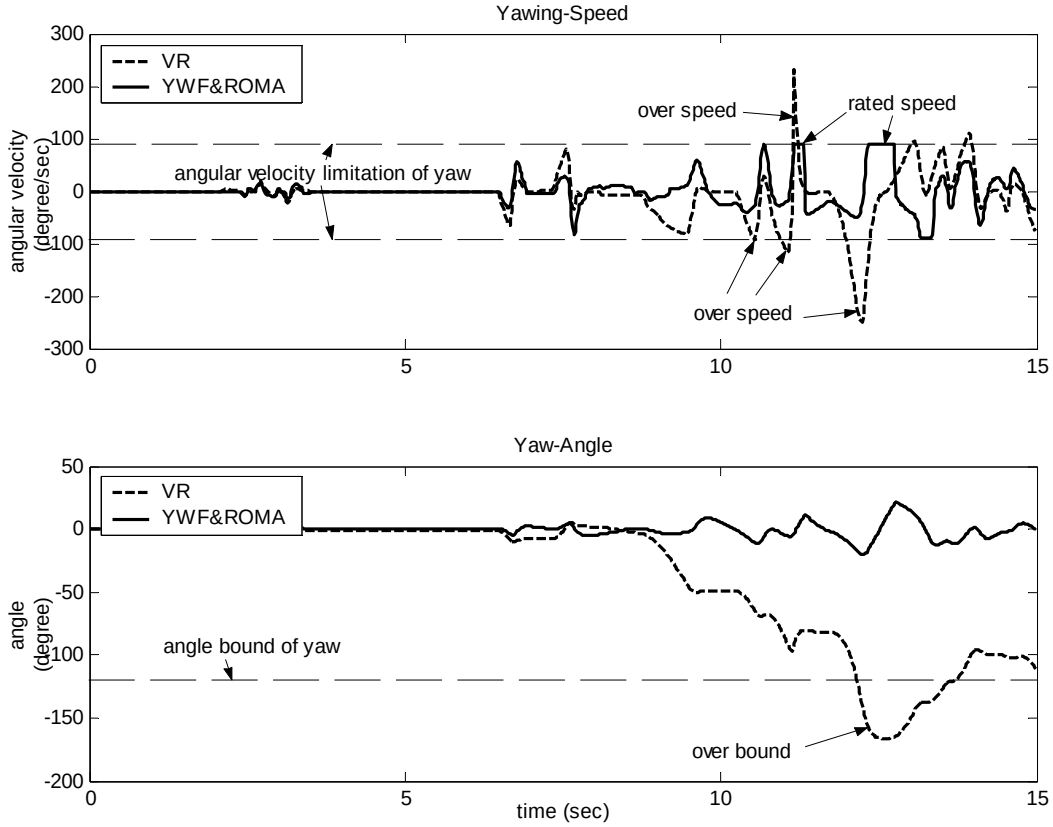

Fig. 35. Comparison of simulator output, yaw-motion:

(a) Yawing-speed, using proposed algorithm (ROMA)

(b) Yaw-angle, using proposed algorithm (ROMA)

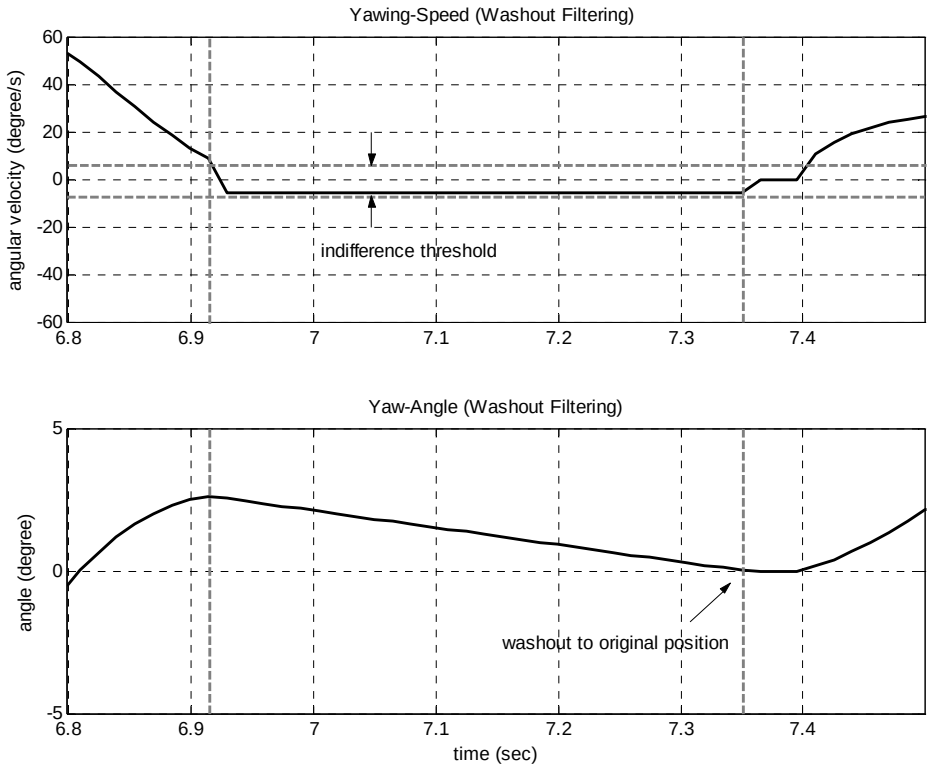

Fig. 36. Yawing-speed and yaw-angle after washout filtering (YWF)

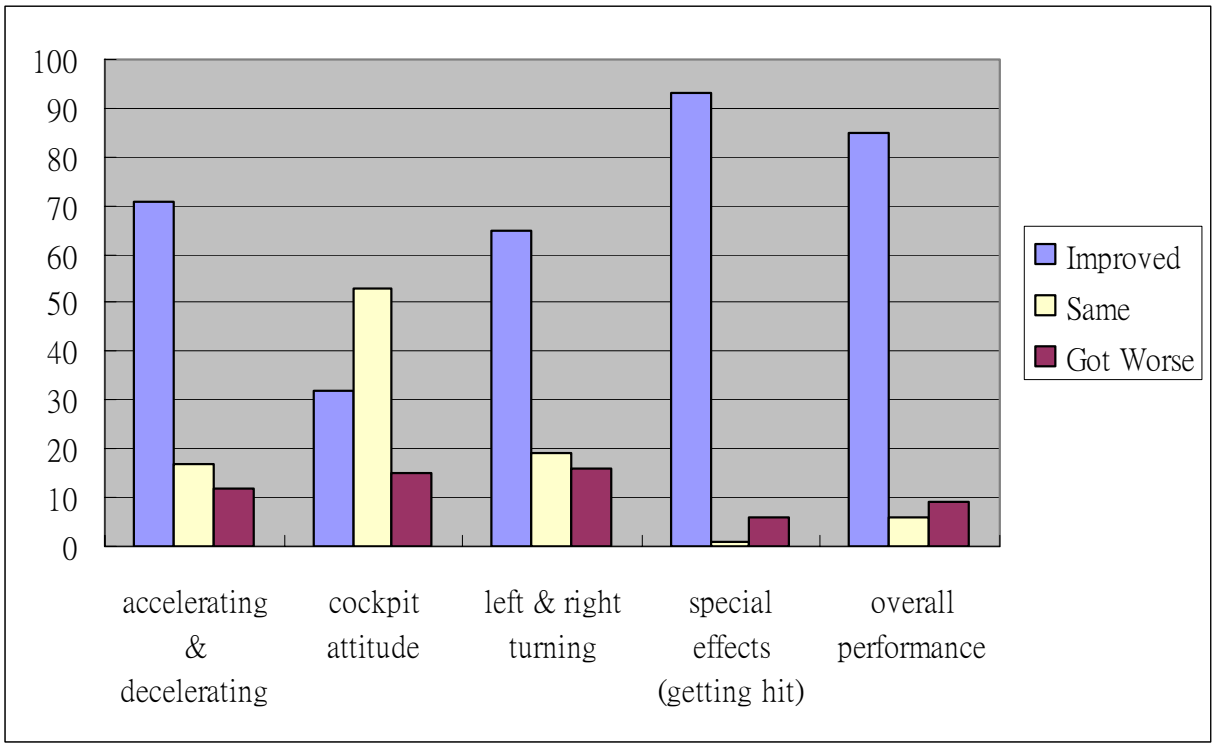

Fig. 37. Subjective feedback from users with five significant characteristics of flight simulators using proposed algorithm (ROMA)

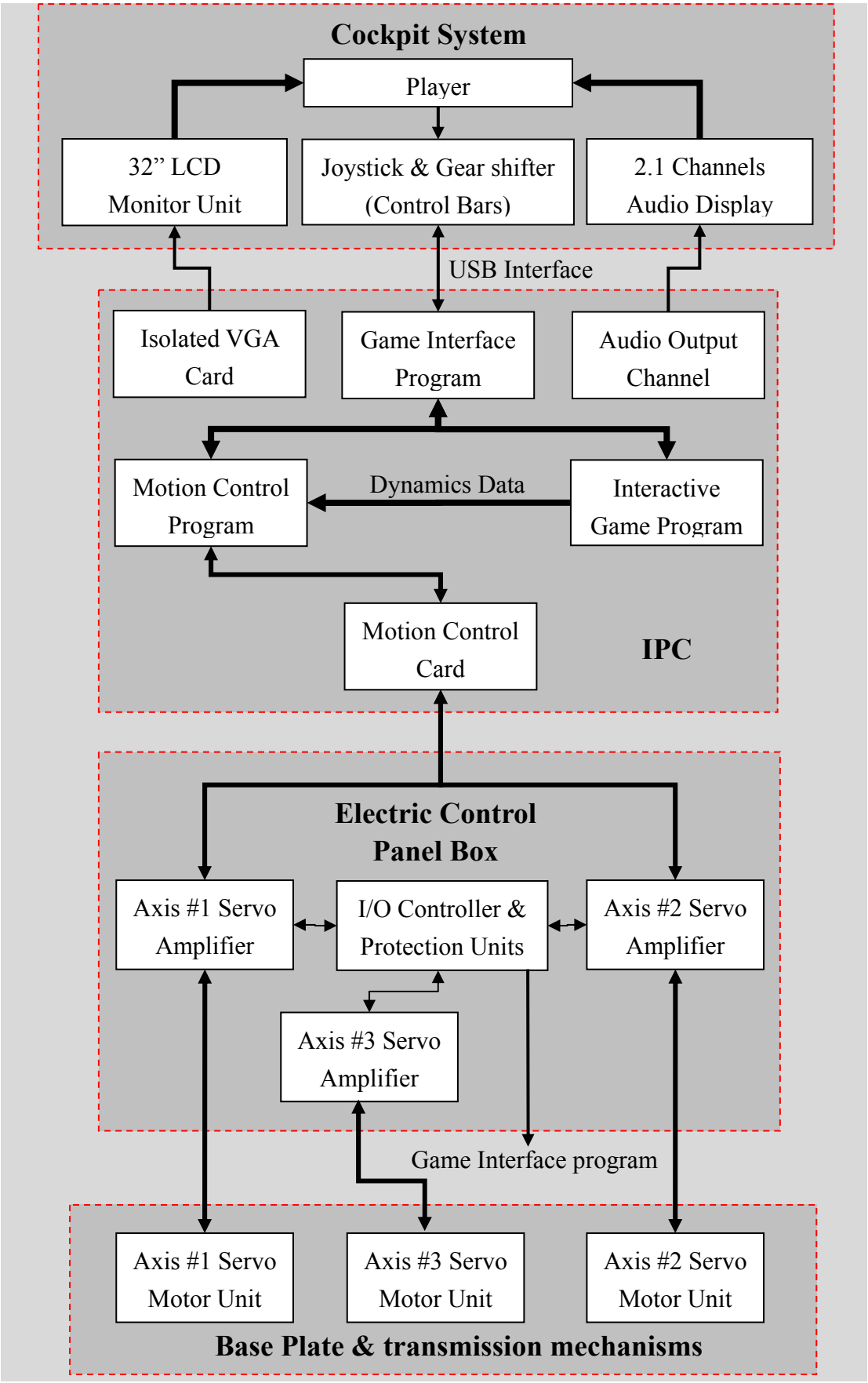

Fig. 38. Complete framework of the entire electrical and mechanical system

Fig. 39. Complete implementation of the system

(Courtesy of IMON Corp.)

Specification	Unit	Value
p_{min}	m	0.203
p_{max}	m	0.2925
h_c	m	0.156
ℓ	m	0.183
u	m	0.170
ϕ	°	21 ~ 69
$[H_x \quad H_y \quad H_z]$	m	[0.25 0 0.5]

Table 1. Experimental Setup of Mechanical System

Specification	Unit	Value
Rated Output	kW	1.5
Rated Speed	rpm	3000
Max. Speed	rpm	5000
Rated Voltage	V	3 ϕ , 200V
Rated Current	A	9.6
Max. Current	A	28.8
Rated Torque	N*m	4.78
Max. Torque	N*m	14.3
Rotor Inertia	$kg*m^2$	$4.51*10^{-4}$
Insulation Class F	Class	F
Weight	kg	7
Ambient Temp.	^oC	-10~+40

Table 2. Experimental Setup of Servo-Drive System

Specification	
Interrupt of Motion Control (ROMA) Programming	10 ms
Interrupt of Virtual Reality (PFO) Programming	30 ms
Calculation Time of Motion Control (ROMA)	less than 1ms
CPU Load	less than 1%(motion control) + 50~60% (VR rendering process)

Table 3. Experimental Setup of Software System

(CPU: PENTIUM D, 3.20GHz, RAM: 2.00GB)

本論文作者已發表之著作

Reviewed Paper:

Yang-Hung Chang, Wei-Hua Chieng, Chung-Shu Liao, Shyr-Long Jeng. A novel master switching method for electronic cam control with special reference to multi-axis coordinated trajectory following. *Control Engineering Practice*, Volume 14, Issue 2, February 2006, Pages 107-120

Yang-Hung Chang, Chung-Shu Liao, Wei-Hua Chieng. Optimal Motion Cueing for 5-DOF Motion Simulations via a 3-DOF Motion Simulator. *Control Engineering Practice*, accepted in May, 2008

Yang-Hung Chang, Bing-Lin Wu, Wei-Hua Chieng. Design for a Novel 2-DOF Motion Platform. *Mechanism and Machine Theory*, submitted to Journal in April, 2008